

1-1-2011

# Raman spectroscopy for the microbiological characterization and identification of medically relevant bacteria

Khozima Mahmoud Hamasha  
*Wayne State University,*

Follow this and additional works at: [http://digitalcommons.wayne.edu/oa\\_dissertations](http://digitalcommons.wayne.edu/oa_dissertations)



Part of the [Physics Commons](#)

---

## Recommended Citation

Hamasha, Khozima Mahmoud, "Raman spectroscopy for the microbiological characterization and identification of medically relevant bacteria" (2011). *Wayne State University Dissertations*. Paper 311.

**RAMAN SPECTROSCOPY FOR THE MICROBIOLOGICAL  
CHARACTERIZATION AND IDENTIFICATION OF MEDICALLY  
RELEVANT BACTERIA**

by

**KHOZIMA MAHMOUD HAMASHA**

**DISSERTATION**

Submitted to the Graduate School

of Wayne State University,

Detroit, Michigan

in partial fulfillment of the requirements

for the degree of

**DOCTOR OF PHILOSOPHY**

2011

MAJOR: PHYSICS

Approved by:

---

Advisor

Date

---

---

---

---

## DEDICATION

*I would like to dedicate my dissertation to the memory of my brother "Saleh".*



## ACKNOWLEDGMENTS

First of all, I would like to express my great thanks to my advisor Dr. Steven Rehse for his guidance and great help and support throughout my research work. I am always appreciative of this precious opportunity to learn from him about all research aspects, starting from thinking about the problems, sharing the ideas, performing the experiments, collecting the data, analyzing the results, and preparing the manuscripts for publication. Also, special thanks to the committee members, Dr. Ratna Naik for her continued support and encouragement through my graduate study, Dr. Choong-Min Kang for his great assistance and generosity through providing his facility to improve my skills and to getting trained in every microbiological aspect related to my research, and Dr. Sean Gavin for his collaboration in this project.

I am out of words to express my special gratitude to all my family members, my parents for their support financially and spiritually to help me reach this point, my husband Qassem Mohaidat for his endless love and encouragement throughout my graduate study, my kids Amr and Sarah for the precious time that I stole from them and my brothers and sisters for their continued sympathy and encouragement. Also I should mention the great help and supports of all my friends, especially Aishah Tahir, Alaa Omari, Daed Manaserah, Hend Mayyas and Rana Garaibih who have made the hard time painless through their love and compassion.

I would like to extend my gratitude to Dr. Vaman Naik for the useful conversations and technical help concerning Raman spectroscopy and Dr. Sunil Palchaudhuri for the valuable discussion through his collaboration in the xylitol project. Also, I am thankful for Dr Sahana Moodakare for her great help on a lot of Raman experiments, Dr Yi Liu from the WSU

Department of Chemistry who trained me on SEM and TEM techniques and Dr. Rangaramanujam M. Kannan (Associate Professor Chemical Eng. and Mat. Sci., Biomed. Eng.) for allowing me to use his microtome for bacteria sectioning. A special thanks to the graduate students Charul Jani (Biological Sciences), Eldar Kurtovic and Emir Kurtovic (School of Medicine) and Kanika Bhargava (Department of Nutrition & Food Science) for their kindness, cooperation, and bacterial samples preparation, Rajesh Regmi for helping me in filling the LN<sub>2</sub> and my lab mate Caleb Ryder for his help and kindness.

Finally, I would take the opportunity to thank all the professors, staff, and students of the Physics Department for the huge knowledge and experience I gained through the past five years.

# TABLE OF CONTENTS

Dedication .....	ii
Acknowledgments .....	iii
List of Tables .....	x
List of Figures .....	xi
Chapter 1 “Introduction” .....	1
1.1 Introduction (Bacteria, Friends and Foes) .....	1
1.2 Bacteria Identification .....	2
1.2.1 Traditional Microbiological Methods .....	2
1.2.2 Genomic (nucleic acid-based) Methods.....	3
1.2.3 Spectroscopic Methods .....	3
1.3 Review of Previous Studies.....	5
1.4 Thesis Scope .....	8
Chapter 1 References .....	10
Chapter 2 “Theoretical Background and Experimental Instrumentation” .....	15
2.1 Raman Spectroscopy .....	15
2.1.1 Theoretical Background .....	16
2.1.2 Raman Signal Enhancement .....	21

2.1.2.1	Surface Enhanced Raman Spectroscopy (SERS) .....	23
2.2	Molecular Vibrations .....	25
2.3	Raman Spectroscopy Instrumentation .....	28
2.3.1	Excitation Source .....	29
2.3.2	Optical Components .....	32
2.3.3	Spectrometer .....	34
2.3.4	Detector/Analysis .....	36
2.4	Bacteria Physiology .....	37
2.4.1	Bacteria Cell Structure and Biochemical Constituents .....	37
2.4.1.1	Cell Envelope Structure .....	38
2.4.1.2	Biochemical Constituents of the Cell .....	40
2.5	Raman Spectra Obtained From Macromolecules .....	41
2.5.1	Proteins .....	41
2.5.2	Lipids .....	44
2.5.3	Polysaccharides .....	45
2.5.4	Nucleic Acids (DNA and RNA) .....	46
2.6	Bacterial Classification .....	47
2.6.1	Gram-Positive Aerobic Cocci .....	47

2.6.2	Gram-Positive Aerobic Bacilli .....	48
2.6.3	Gram-Negative Enterobacteriaceae .....	49
	Chapter 2 References .....	50
Chapter 3 “Data Collection and Statistical Analysis Methods” .....		53
3.1	Sample Preparation for Raman Spectroscopy .....	53
3.2	Instrument Calibration and Spectrum Acquisition .....	54
3.3	Data Preprocessing for Statistical Analysis .....	58
3.4	Multivariate Statistical Methods .....	60
3.4.1	Principal Component Analysis (PCA) .....	60
3.4.2	Discriminant Function Analysis (DFA) .....	62
	Chapter 3 References .....	66
Chapter 4 “Raman Spectroscopy for the Discrimination of Bacterial Strains” .....		67
4.1	<i>E. coli</i> Bacterial Strains .....	67
4.1.1	Introduction .....	67
4.1.2	Bacterial Strains and Culture Conditions .....	68
4.1.3	Internal Validation .....	69
4.2	<i>E. coli</i> Results and Discussion .....	69
4.2.1	Blind Study: Internal Validation .....	73
4.2.2	<i>E. coli</i> Conclusions .....	77

4.3 <i>E. coli</i> Summary .....	78
4.4 <i>Staphylococcus aureus</i> Bacterial Strains .....	79
4.4.1 Introduction .....	79
4.4.2 Bacterial Strains and Culture Conditions .....	80
4.5 <i>S. aureus</i> Results and Discussion .....	81
4.6 <i>S. aureus</i> Conclusions and Summary.....	87
4.7 Summary .....	88
Chapter 4 References .....	89
Chapter 5 “Raman Spectroscopy Study of Xylitol Uptake and Metabolism in Gram-Positive and Gram-Negative Bacteria and the Stability of Xylitol Metabolic Derivatives in Viridans Group Streptococci” .....	92
5.1 Introduction .....	92
5.2 Materials and Methods .....	94
5.2.1 Bacterial Strain Selection and Growth Conditions .....	94
5.2.2 Raman Data Collection .....	97
5.3 Results .....	98
5.3.1 Differential Gram-Staining .....	98
5.3.2 Raman Spectroscopy of Xylitol Powder and Solution .....	100

5.3.3	Raman Spectroscopy of the Uptake of Xylitol by <i>E. coli</i> K-12 (xylitol operon-deficient), its Pili- and Flagella-Deficient Derivative <i>E. coli</i> JW1881-1, and <i>E. coli</i> C(xylitol operon-positive, but in a repressed state).....	102
5.3.4	Xylitol-Uptake and Stability in <i>E. coli</i> HF4714 .....	106
5.3.5	Xylitol Metabolism by Gram-Positive <i>S. viridans</i> .....	107
5.3.6	The Stability of Xylitol Derivative(s) Formed in Xylitol-Grown <i>S. viridans</i> Measured by Raman Spectroscopy .....	108
5.4	Discussion .....	113
5.4.1	Anti-Adhesion Effects of Xylitol .....	114
5.4.2	Bacterial Morphology and Physiology and Their Importance to Xylitol Treatment .....	116
5.4.3	Fluoride and Xylitol .....	116
5.5	Summary .....	117
	Chapter 5 References .....	119
Chapter 6	“The Effect of Wag31 Phosphorylation on the Cells and the Cell Envelope Fraction of Wild-type and Conditional Mutants of <i>Mycobacterium smegmatis</i> Studied in Vivo by Visible-Wavelength Raman Spectroscopy” .....	124

6.1 Introduction .....	124
6.2 Materials and Methods.....	125
6.2.1 Microorganisms and Growth Conditions .....	125
6.2.2 Cell Envelope Isolation .....	126
6.3 Results and Discussion .....	127
6.3.1 Raman Spectra From Bacteria Cells .....	127
6.3.2 Raman Spectra From Bacterial Cell Envelope .....	133
6.4 Raman Spectroscopy on Protein.....	139
6.5 Summary .....	143
Chapter 6 References .....	145

Chapter 7 “Surface-Enhanced Raman Spectroscopy (SERS) Study of bacteria”.148

7.1 Introduction .....	148
7.2 Materials and Methods .....	149
7.2.1 Microorganisms and Growth Conditions .....	149
7.2.2 Silver Colloids Solution Materials and Preparation .....	149
7.2.3 Raman Data Collection .....	151
7.3 Results and Discussion .....	151
7.3.1 R6G Results .....	151
7.3.2 Bacteria Results .....	154

7.4 Summary and Conclusions .....	158
Chapter 7 References .....	159
<b>Chapter 8 “Bacterial Characterization Using Electron Microscopy” .....</b>	<b>160</b>
8.1 Introduction .....	160
8.2 Transmission Electron Microscopy (TEM) .....	160
8.3 Scanning Electron Microscope (SEM) .....	164
8.4 Conclusions .....	166
Chapter 8 References .....	166
<b>Abstract.....</b>	<b>167</b>
<b>Autobiographical Statement.....</b>	<b>169</b>

## LIST OF TABLES

Table 2.1: The specifications of the Modu-laser Ar-ion laser.....	31
Table 2.2: The macromolecules in the bacterial cell and their subunits, location, and average percentage composition of the dry cell weight.....	41
Table 2.3: The band assignments for the main bands that appear in the amino acids Raman spectra .....	43
Table 4.1: Identification results of the internal validation test.....	75
Table 4.2: Assignment of the Raman vibrational bands observed in <i>S. aureus</i> Raman spectra .....	82
Table 5.1: The band assignments for the main Raman peaks of 100% xylitol .....	101
Table 5.2: Assignment of the main Raman vibrational bands observed in <i>S. viridans</i> Raman spectra .....	110
Table 6.1: Assignment of the Raman vibrational bands observed in this study.....	129

## LIST OF FIGURES

Figure 2.1: Raman scattering energy level diagram and representative Raman spectrum .....	19
Figure 2.2: Raman spectrum of Si wafer .....	20
Figure 2.3: Raman spectrum of sucrose .....	21
Figure 2.4: Raman spectrum of bacterial sample .....	22
Figure 2.5: SEM images of the aggregated silver nanoparticles on <i>E. coli</i> bacteria .....	24
Figure 2.6: Raman and SERS spectra of <i>E. coli</i> cells.....	25
Figure 2.7: A simple model of O=CH <sub>2</sub> vibrational modes .....	27
Figure 2.8: A typical Raman spectroscopy setup .....	28
Figure 2.9: A schematic diagram of an Ar-ion laser .....	29
Figure 2.10: Energy level diagram of Ar-ion Laser .....	30
Figure 2.11: Picture of Modu-laser .....	31
Figure 2.12: A picture of lens and optical fiber .....	32
Figure 2.13: A picture of the Raman microscope .....	33
Figure 2.14: A picture and Schematic diagram of spectrometer components.....	35
Figure 2.15: Picture of TRIAX550 spectrometer .....	35
Figure 2.16: A picture of the home-built Raman spectroscopy instrumentation.....	36
Figure 2.17: Scanning electron microscope (SEM) images of different bacteria .....	37
Figure 2.18: Bacteria Cell Structure .....	38
Figure 2.19: Composition of the cell wall of Gram-positive and Gram-negative bacteria .....	40
Figure 2.20: Raman spectra of amino acids with non-cyclic side chain .....	42

Figure 2.21: Raman spectra of amino acids with a cyclic side chain .....	42
Figure 2.22: Raman spectra of saturated fatty acids .....	44
Figure 2.23: Raman spectra of some saccharides .....	45
Figure 2.24: Raman spectra of Nucleic acids bases .....	46
Figure 2.25: Bacteria classification flow chart .....	47
Figure 3.1: Bacteria cultured on a plate, delivered into a tube and smeared on a slide .....	53
Figure 3.2: Raman spectra obtained from quartz and bacteria .....	54
Figure 3.3: Labspec software home page .....	56
Figure 3.4: Calibration process of the Si Peak .....	57
Figure 3.5: Spectra of bacteria in the spectral range 600-2000 $\text{cm}^{-1}$ .....	57
Figure 3.6: Raman spectrum of bacteria before and after processing.....	59
Figure 3.7: Principal component loadings of the PCA .....	61
Figure 3.8: The procedure of multivariate analysis on Raman spectra .....	65
Figure 3.9: Example of DFA plot using two discriminant functions .....	65
Figure 4.1: Comparison of the normalized averaged Raman spectra of four <i>E.coli</i> strains .....	70
Figure 4.2: PC-DFA plot of all the Raman spectra .....	71
Figure 4.3: The first principal component loading of the PCA plotted with the difference of the average Raman spectrum of <i>E. coli</i> O157:H7 and <i>E.coli</i> C bacteria .....	72
Figure 4.4: PC-DFA plot of training set and test set Raman spectra obtained from four <i>E. coli</i> strains.....	74
Figure 4.5: The general correlation between the size of the training set used in the model to identify the unknown spectra and the accuracy of identification of the unidentified test spectra.....	77
Figure 4.6: Comparison of the normalized averaged Raman spectra of four <i>S. aureus</i> strain.....	81
Figure 4.7: A plot of first four PC loadings in the spectral region 600-2000 $\text{cm}^{-1}$ .....	83

Figure 4.8: The loadings of the first PC with the main spectral features identified .....	84
Figure 4.9: Principal component loadings of the PCA performed on the Raman spectra acquired from four <i>S. aureus</i> strains compared to the difference of the average spectra between the different strains .....	85
Figure 4.10: The loadings of the second PC plotted with the difference of the average spectrum of DRSA and MRSA .....	86
Figure 4.11: PC-DFA plot showing the first two discriminant function scores of all the Raman spectra obtained from the four strains of <i>S. aureus</i> .....	87
Figure 5.1: Xylitol crystals and xylitol molecular structure .....	92
Figure 5.2: Action of xylitol on <i>S. viridans</i> ultrastructure as revealed by differential Gram-staining imaged with the same magnification .....	98
Figure 5.3: Raman spectra for different concentrated spots of xylitol and the main peaks of xylitol .....	100
Figure 5.4: The averaged Raman spectrum from xylitol-exposed <i>E. coli</i> K-12, the difference of the xylitol-exposed spectra and the control <i>E. coli</i> K-12 and the difference of the post-exposure chase spectra and the control <i>E. coli</i> K-12, and Raman spectrum from 100% xylitol.....	102
Figure 5.5: The averaged Raman spectrum from xylitol-exposed <i>E. coli</i> C, the difference of the xylitol-exposed spectra and the control <i>E. coli</i> C and the difference of the post-exposure chase spectra and the control <i>E. coli</i> C, and xylitol Raman spectrum ....	104
Figure 5.6: The averaged Raman spectrum from xylitol-exposed <i>E. coli</i> JW1881-1, the difference of the xylitol-exposed spectra and the control <i>E. coli</i> JW1881-1 and the difference of the post-exposure chase spectra and the control <i>E. coli</i> JW1881-1, and xylitol Raman spectrum .....	105
Figure 5.7: The averaged Raman spectrum from xylitol-exposed <i>E. coli</i> HF4714, the difference of the xylitol-exposed spectra and the control <i>E. coli</i> HF4714 and the difference of the post-exposure chase spectra and the control <i>E. coli</i> HF4714, and xylitol Raman spectrum.....	106

Figure 5.8: The averaged Raman spectrum from xylitol-exposed <i>S. viridans</i> , the difference of the xylitol-exposed spectra and the control <i>S. viridans</i> and the difference of the post-exposure chase spectra and the control <i>S. viridans</i> , and xylitol Raman spectrum.....	107
Figure 5.9: Raman spectra from the <i>S. viridans</i> cells directly after harvesting from the xylitol-fed bacterial cultures (0 hours) and after 24 and 72 hours of growth in the xylitol .....	109
Figure 5.10: The intensity of the five labeled peaks as a function of time relative to a normalization peak at $1000\text{ cm}^{-1}$ and the peak at $1775\text{ cm}^{-1}$ .....	111
Figure 5.11: Raman spectra from the <i>S. viridans</i> cells harvested from the TSA growth media at 24, 48, and 72 hours.....	112
Figure 5.12: The intensity of the five labeled peaks as a function of time relative to a normalization peak at $997\text{ cm}^{-1}$ and the peak at $1392\text{ cm}^{-1}$ .....	112
Figure 6.1: Typical Raman spectra of <i>M. smegmatis</i> expressing phosphomimetic <i>M. tuberculosis wag31</i> ( <i>wag31T73E<sub>Mtb</sub></i> ) (TE), wild-type <i>wag31<sub>Mtb</sub></i> (WT), or phosphoablative <i>wag31T73A<sub>Mtb</sub></i> (TA).....	127
Figure 6.2: Principal component loadings of the PCA performed on the Raman spectra acquired from three mutants of <i>M. smegmatis</i> .....	130
Figure 6.3: A discriminant function analysis plot of the Raman spectra from the three <i>M. smegmatis</i> cell types.....	132
Figure 6.4: The average Raman spectra of P60 cell envelope fraction of the three mutants of <i>M. smegmatis</i> cells.....	134
Figure 6.5: The difference between the average spectrum of the TA and TE cell envelope fraction plotted with the PC1 loadings .....	135
Figure 6.6: A comparison of the average Raman spectra of the five classification groups studied in this work (the spectra of the cells of the three <i>wag31</i> conditional mutants of <i>M. smegmatis</i> and the spectra of the cell envelope fraction of two of them).....	136
Figure 6.7: A PCA-DFA plot of all the Raman spectra showing the high-degree of similarity between wild-type and TA cells, and the ability to easily distinguish spectra from other groups.....	138

Figure 6.8: A typical Raman spectra obtained from <i>wag31T73E<sub>Mtb</sub></i> and <i>wag31T73E<sub>Mtb</sub></i> protein compared with the Raman spectrum obtained from the protein-fixing buffer.....	139
Figure 6.9: A comparison between typical spectra obtained from powdered lysozyme and BSA proteins.....	140
Figure 6.10: Micrographs of dried protein residue from solutions of lysozyme and BSA.....	141
Figure 6.11: Raman spectra obtained from lysozyme and BSA protein solutions with different concentration.....	142
Figure 6.12: A comparison between Raman spectra obtained from lysozyme and BSA proteins with different concentrations .....	143
Figure 7.1: Raman spectra of R6G dye solution and silver colloids solution mixed with different ratios.....	152
Figure 7.2: A comparison between the spectra of R6G, Ag colloids and the mixture of equal amount of R6G and Ag colloids, and a comparison between processed Raman spectra and SERS spectra of R6G dye.. ..	153
Figure 7.3: SERS spectra of <i>E. coli</i> K12 and the silver colloids solution mixed with different ratios.....	154
Figure 7.4: A comparison between SERS and Raman spectra of <i>E. coli</i> K12, (A) raw data shows the signal enhancement, (B) processed data compares the signal features. ....	155
Figure 7.5: SERS spectra of TA, TE, and WT and the silver colloids solution mixed with equal amounts and SERS spectra of varying TA-colloids ratios.....	156
Figure 7.6: SERS spectra of TA, where the bacteria and the silver colloids solution mixed with different ratios .....	157

Figure 8.1: TEM image of *M. smegmatis*. We are trying to quantify variations in the cell membrane thickness.....164

Figure 8.2: SEM image of *M. smegmatis* cells containing phosphorylated (Wag31T73E) and non-phosphorylated Wag31T73A).....165

# Chapter 1

## Introduction

### 1.1 Introduction (Bacteria, Friends and Foes)

Bacteria are prokaryotic single-celled organisms that have a single molecule of DNA representing the nucleus with no membrane bounding the nucleus.<sup>1</sup> Its name was devised from the Greek word bakterion which means small rod.<sup>2,3</sup> Bacteria are widespread everywhere around us, in air, water, food, soil, and in all living bodies. They are very different in their required growth conditions, but they are common in their need for sugar as food to survive.

Despite the fact that the word bacteria is connected with infectious diseases; the vast majority of bacteria do not affect human health through an interaction with our immune system. Actually, some of them are important for human life, food industry, agriculture, and biotechnology. For example, certain kinds of bacteria such as *Escherichia coli* are essential for the food digestion,<sup>4,5</sup> some are used to prepare and preserve food,<sup>6</sup> while others called decomposers are responsible for waste decay.<sup>7</sup> Recently a soil bacterium known as *Streptomyces* has been used to produce special kinds of antibiotics such as nocardicin and streptomycin.<sup>8,9</sup>

On the other hand, pathogenic bacteria can be very dangerous and are considered life threatening microorganisms. To give some examples of these pathogens, some species of *Staphylococci* bacteria cause food poisoning and toxic-shock syndrome,<sup>10</sup> some species of *Streptococci* cause throat and middle ear infections<sup>11</sup> and dental caries,<sup>12</sup> a special strain of *E. coli* causes severe diarrhea, and *Mycobacterium tuberculosis* (the agent of tuberculosis) is considered to be one of the most dangerous pathogens with a high mortality,<sup>13</sup> infecting one out of every three people globally.<sup>14</sup> Since bacteria have a significant impact to our life in different

ways, we should think about how we can detect and characterize these microorganisms and control their activities to avoid their threats. The methods that have been developed over decades to achieve this goal are illustrated in the following section.

## **1.2 Bacteria Identification**

Detection and identifying bacteria is of great importance in clinical medicine, food safety, and water contamination control purposes. The early (same-day) *in vitro* identification of medically relevant microorganism can have a large impact on patients with infection. It has been proven that overall health care costs and mortality rates were significantly reduced when rapid bacterial identification can be achieved.<sup>15</sup> Many methods have been established for bacterial identification, below is a brief overview of some of them:

### **1.2.1 Traditional Microbiological Methods**

Traditional methods of bacterial identification rely on the cultivation of bacteria from a pure culture. By determining the response of the bacteria to the environmental growth conditions such as the required nutritional media or the pH value of the media and comparing their characteristics with known organisms, a trained microbiologist can identify an unknown specimen. In this method, the sample is often cultured on different agar nutrition media and then a viable counting measurement is carried out by counting the number of visible colonies in each medium.<sup>16</sup> In order to identify the bacteria, many other tests are often performed such as the Gram-stain reaction, morphology tests, and motility tests.<sup>17</sup> These measurements are time consuming (they can take up to a few days depending on the time required to culture the specimen) and laborious with limited accuracy since the bacteria that are not cultivated are not counted.<sup>18</sup>

### 1.2.2 Genomic (nucleic acid-based) Methods

In these techniques, the classification of bacteria is based on finding similarities between the DNA of two different bacteria (DNA-DNA hybridization) or by determining the sequences of bacterial nucleotide and comparing it with known sequences in a database; these processes are called sequence analysis of ribosomal DNA (16S rDNA) and ribosomal RNA (16S rRNA). DNA-DNA hybridization is mostly used for the classification of bacteria at the species level,<sup>19</sup> where the relationship between the organisms is determined by the degree of their DNA hybridization. Two different strains will fall in the same species if their hybridization value is more than 70%.<sup>18</sup> This method needs a specialist in bacterial taxonomy and requires a long time. Moreover it cannot help in bacterial identification due to the lack of characteristic information about the unknown bacteria.<sup>20</sup>

It has been found that certain species could not be distinguished by 16S rRNA sequence comparison.<sup>21</sup> Also 16S rDNA sequence data could not identify bacteria at the species level.<sup>22</sup> Recently a process called polymerase chain reaction (PCR) has been used to characterize bacteria by copying a particular nucleotides sequence of the DNA millions of copies in hours.<sup>23,24,25</sup> PCR is useful for detecting bacteria that are hard to culture *in vitro* like *Mycobacterium tuberculosis*.<sup>26</sup> This method is not as time consuming, but it requires a lot of processes that needs a specialist in this field.

### 1.2.3 Spectroscopic Methods

New approaches of bacterial identification have been considered recently due to the increasing needs for rapid and accurate identification of bacteria (without a lot of labor and without the need of a specialist). Mass spectrometry (MS) has been successful in comparing inter-strains of various clinical bacterial samples.<sup>27</sup> Also the matrix assisted laser

desorption/ionization time-of-flight mass spectrometry (MALDI-TOF-MS) technique has been used for the rapid identification of bacteria.<sup>28,29</sup> This technique provides highly reproducible measurements without laborious work, but it is a destructive and expensive method. Recently laser-induced breakdown spectroscopy (LIBS) has been used for rapid bacterial identification and classification<sup>30</sup> and to study the metabolic activity of bacteria.<sup>31</sup> Similar to Raman spectroscopy, LIBS is an all-optical laser based spectroscopy that can provide a unique fingerprint of bacteria based on their atomic compositions.

Vibrational spectroscopic techniques, infrared (IR) and Raman spectroscopy (RS), have been used extensively to identify bacterial samples by a careful investigation of the vibrating modes of the molecules in the bacteria. Lately, Fourier transform infrared (FT-IR) spectroscopy has been accepted for microorganism characterization where an infrared light is absorbed by the bacterial sample when its frequency is matched with the natural vibrational frequency of the sample molecules.<sup>32</sup> The absorbed radiation can be detected and transformed into a spectrum using Fourier transform mathematics. This process will occur only if there is a net change in the molecules' dipole moment. Raman spectroscopy is used to characterize bacteria through the interaction of coherent light and the sample's molecules. This interaction is different than that of IR spectroscopy. In Raman, an intense beam of laser in the visible or infrared or ultraviolet region is focused on the sample and the scattered beam is detected to get valuable information about the vibration modes of the sample molecules. An excellent review of the uses of vibrational spectroscopy to identify bacteria was given by Maquelin *et al.* in 2002.<sup>33</sup> In general, those methods are non-invasive and nondestructive and proven to provide rich information of bacteria at the strain level with less time and minimal effort. In the next section I will shed some light on the Raman spectroscopy technique and its specific application in bacterial systems.

Raman spectroscopy has recently gained popularity as an attractive approach for the biochemical characterization, rapid identification, and accurate classification of a wide range of bacterial genre, species, and strains.<sup>34,35,36,37,38,39,40,41,42,43</sup> Various experiments have been performed using different techniques of the Raman approach. To list just a few examples, Fourier transform Raman spectroscopy was applied for the characterization of the bacterial cell wall,<sup>44</sup> surface-enhanced Raman spectroscopy (SERS) experiments were performed to identify bacteria and discriminate between microorganisms at the strain level,<sup>45</sup> ultraviolet resonance Raman spectroscopy was successfully used to discriminate very closely related strains of endospores-forming bacteria,<sup>46</sup> and confocal Raman microscopy has been used to study the chemical composition of a single bacteria cell,<sup>47</sup> and to study the bioavailability and toxicity of pollutants.<sup>48</sup> I will now give a short summary of the important results that have been achieved previously using Raman spectroscopy to characterize, classify and identify bacterial specimens.

### **1.3 Review of Previous Studies**

Goeller and Riley studied the discrimination of bacteria and bacteriophages (viruses that can infect the bacterial cells) by using Raman spectroscopy (RS) and surface-enhanced Raman spectroscopy (SERS).<sup>49</sup> They observed that there are spectral peaks that appear in the bacteriophages' spectra and not in the *E. coli* spectrum. This significant difference can be used to distinguish between bacteria and bacteriophages. On the other hand, the spectra of the bacteriophage had similar features but with different intensities in some peaks which revealed that the bacteriophages had similar compositions but with different proportions. In these studies, glass slides coated with gold colloids were used for SERS measurements and an *E. coli* spectrum taken with SERS showed an increase in the intensity of Raman spectral features. Unfortunately the location of the Raman peaks was also shifted, so no comparison could be done between RS

spectra and SERS spectra. Overall this study showed that RS and SERS can both effectively discriminate between specific specie of bacteria and bacteriophages and the addition of gold colloids can increase the Raman signal intensity.

In 2000, Maquelin et al. used the RS method for the identification of clinically relevant microorganisms grown on a solid culture medium. They examined five different bacterial strains (*Staphylococcus aureus* ATCC 29213, *Staphylococcus aureus* UHR 28624, *Staphylococcus epidermidis* UHR 29489, *E. coli* ATCC 25922, and *Enterococcus faecium* BM 4147) using a Renishaw system 1000 Raman microspectrometer. Raman spectra of the bacterial strains revealed spectral differences characteristic of different strains.<sup>38</sup> To discriminate these types of spectra, principal component analysis (PCA) and hierarchical cluster analysis (HCA) were performed. These authors concluded that Raman microspectroscopy combined with the multivariate statistical techniques were able to discriminate between different bacterial strains and between the species level of *Staphylococcus* strains as well.

UV Resonance Raman spectroscopy (UVRRS) was used by E. Consuelo and R. Goodacre to study different endospores-forming bacteria belonging to the genera *Bacillus* and *Brevibacillus*.<sup>46</sup> The excitation wavelength was in the deep ultra violet region (244 nm). In this case, resonance Raman will take place which leads to an enhancement in the weak Raman bands by blocking the fluorescence. The spectra were analyzed by PCA, discriminant function analysis (DFA), and HCA. The results showed that DFA and HCA could discriminate between the spectra representing the main groups of bacteria under investigation. This study confirmed that UVRRS can be used as a tool for discriminating between very closely related endospore-forming bacteria.

Huang et al. have carried out Raman microscopic analysis of single microbial cells and demonstrated the utility of this approach in discriminating bacteria species.<sup>50</sup> In their study, they used seven different species of Gram-positive and Gram-negative bacteria. Raman spectra obtained from the seven bacteria species appear to have similar features with some differences in the intensity of some peaks. In order to figure out if Raman spectroscopy could discriminate between the seven spectra, the multivariate statistical techniques of PCA, DFA, and HCA were used. It was observed that Raman spectroscopy has the potential to discriminate between those bacteria species using only their single cell Raman spectrum which represents a “chemical fingerprint.”

Harz et al. studied the identification of bacterial cells of the genus *Staphylococcus* using micro-Raman spectroscopy (where a high-quality optical microscope is coupled to the spectrometer to enable the excitation and collection of Raman spectra).<sup>51</sup> Raman measurements of eight different strains of *Staphylococci* were recorded to get Raman spectra. The spectra were analyzed by hierarchical cluster analysis (HCA) which revealed that the discrimination between different strains of bacteria can be achieved using micro-Raman spectroscopy.

Jarvis and Goodacre used surface-enhanced Raman spectroscopy (SERS) for rapid differentiation among bacteria that cause urinary tract infections (UTI).<sup>45</sup> Bacteria species were isolated from UTI, and cultivated for 16 hr on a LabM blood agar base, then added to a silver colloid and spotted onto a CaF<sub>2</sub> substrate until it dried to be ready for SERS measurements. PCA followed by DFA were used repeatedly to analyze the SERS data. To improve the discrimination between groups, HCA was also used.

## 1.4 Thesis Scope

The overarching theme of this dissertation is to use Raman spectroscopy for the chemical characterization of microbiological targets, and to quantify the differences that exist between bacterial samples based on their inherent biochemical differences or based on specifically induced changes (e.g. in membrane chemistry due to growth conditions, changes due to various kinase introductions, etc.). Furthermore, the potential of Raman spectroscopy as a new tool for bacterial discrimination at the strain level is studied. In this way, new knowledge concerning the use of this spectroscopic technique on bacteriological samples and concerning the biochemical composition of intentionally altered bacterial samples will be obtained.

First in Chapter 2 I will discuss the theoretical background of Raman spectroscopy, bacterial physiology, and the Raman instrumentation that has been used for this work. The procedures of data collection will be described in Chapter 3.

Specific projects were conducted to achieve those goals; first a series of experiments were performed to identify and discriminate between different bacterial strains of *E. coli* and *Staphylococcus aureus* bacterial species. This study included discrimination between pathogenic and non-pathogenic strains as well and will be described in Chapter 4.

Raman spectroscopy was used to characterize the uptake and metabolic activity of xylitol in pathogenic (*viridans group Streptococcus*) and nonpathogenic (*E. coli*) bacteria by taking their Raman spectra before xylitol exposure and after growing with xylitol and detecting any significant difference in the molecular vibrational modes during this process. This will be described in Chapter 5.

The effect of a key cell-division protein (Wag31) on the molecular structure of *Mycobacterium smegmatis* and on the biosynthesis of its cell wall was investigated by collecting

and analyzing Raman spectra of conditional mutants of bacteria expressing three different phosphorylation forms of Wag31. This will be described in Chapter 6.

The use of the SERS technique with our visible wavelength apparatus was investigated to improve the intensity and the reproducibility of the Raman spectra acquired from different species of bacteria and the resultant spectra were compared to RS spectra. This will be described in Chapter 7. Finally, in chapter 8 I will discuss the characterization of the outer cell surface and the inner cross-section of bacteria using scanning electron microscopy and transmission electron microscopy.

## CHAPTER 1 REFERENCES

- 
- <sup>1</sup> M. Madigan, J. Martinko, and J. Parker, *Brock Biology of Microorganisms*, 9th Edition, Prentice Hall College Div (1996).
- <sup>2</sup> G. Gordh and D.H. Headrick, *A Dictionary of Entomology*, CAB International (2001).
- <sup>3</sup> L. Margulis and M.J. Chapman, foreword by E.O. Wilson, *Kingdoms & Domains An Illustrated Guide to the Phyla of Life on Earth*, 4<sup>th</sup> ed. (1998).
- <sup>4</sup> R. Bentley and R. Meganathan, "Biosynthesis of vitamin K (menaquinone) in bacteria," *Microbiology Reviews* **46**:241–80 (1982).
- <sup>5</sup> S. Hudault, J. Guignot, and A.L. Servin, "Escherichia coli strains colonising the gastrointestinal tract protect germfree mice against Salmonella typhimurium infection," *Gut* **49**:47–55 (2001).
- <sup>6</sup> T. Ishige, K. Honda, and S. Shimizu, "Whole organism biocatalysis," *Current Opinion in Chemical Biology* **9**:174–80 (2005).
- <sup>7</sup> M.H. Beare, R.W. Parmelee, P.F. Hendrix, and W. Cheng. "Microbial and faunal interactions and effects on litter nitrogen and decomposition in agroecosystems," *Ecological Monographs* **62**:569-591 (1992).
- <sup>8</sup> S.D. Bentley, K.F. Chater, A.-M. Cerden O-Tarraga, G.L. Challis, N.R. Thomson, K.D. James, D.E. Harris, M.A. Quail, H. Kieser, D. Harper, A. Bateman, S. Brown, G. Chandra, C.W. Chen, M. Collins, A. Cronin, A. Fraser, A. Goble, J. Hidalgo, T. Hornsby, S. Howarth, C.-H. Huang, T. Kieser, L. Larke, L. Murphy, K. Oliver, S. O'Neil, E. Rabinowitsch, M.-A. Rajandream, K. Rutherford, S. Rutter, K. Seeger, D. Saunders, S. Sharp, R. Squares, S. Squares, K. Taylor, T. Warren, A. Wietzorrek, J. Woodward, B.G. Barrell, J. Parkhill and D.A. Hopwood, "Complete genome sequence of the model actinomycetes *Streptomyces coelicolor* A3(2)," *Nature* **417**:141–147 (2002).
- <sup>9</sup> D.-J. Kim, J.-H. Huh, Y.-Y. Yang, Choong-Min Kang, I.-H. Lee, C.-Gu Hyun, S.-K. Hong, and J.-W. Suh, "Accumulation of S-Adenosyl-L-Methionine Enhances Production of Actinorhodin but Inhibits Sporulation in *Streptomyces lividans*," *TK23, Journal of Bacteriology* **185**:592-600 (2003).
- <sup>10</sup> J. Todd, M. Fishaut, F. Kapral and T. Welch, "Toxic-shock syndrome associated with phage-group -i *staphylococci*," *The Lancet* **312**:1116-1118 (1978).

- 
- <sup>11</sup> F. Dobbs, "A scoring system for predicting group A streptococcal throat infection," *British Journal of General Practice* **46**:461-464 (1996).
- <sup>12</sup> F.J.M. Roeters, J.S. van der Hoeven, R.C.W. Burgersdijk, and M.J.M. Schaeken, "*Lactobacilli*, Mutans *streptococci* and Dental Caries: A Longitudinal Study in 2-Year-Old Children up to the Age of 5 Years," *Caries Research* **29**:272-279 (1995).
- <sup>13</sup> K.J. Ryan, and C.G. Ray, *Sherris Medical Microbiology*, 4th ed., McGraw Hill (2004).
- <sup>14</sup> 2007 *Tuberculosis Facts Sheet*, World Health Organization, (2007).
- <sup>15</sup> G.V. Doern, R. Vautour, M. Gaudet, and B. Levy, "Clinical impact of rapid in vitro susceptibility testing and bacterial identification," *Journal of Clinical Microbiology* **32**:1757–1762 (1994).
- <sup>16</sup> A.S. Mckee, A.S. Mcdermid, D.C. Ellwood, and P.D. Marsh, "The establishment of reproducible complex communities of oral bacteria in chemostat using define inocula," *Journal of Applied Bacteriology* **59**:263-275 (1985).
- <sup>17</sup> P. Singleton, *Bacteria in biology, biotechnology and medicine*, Fifth edition (1999).
- <sup>18</sup> R.I. Amann, W. Ludwig, and K.H. Schleifer, "Phylogenetic identification and in situ detection of individual microbial cells without cultivation," *Microbiology Reviews* **59**:143-169 (1995).
- <sup>19</sup> H. Christensen, O. Angen, R. Mutters, J.E. Olsen, and M. Bisgaard, "DNA-DNA hybridization determined in micro-wells using covalent attachment of DNA," *International Journal of Systematic and Evolutionary Microbiology* **50**:1095-1102 (2000).
- <sup>20</sup> L. Vauterin, J. Rademaker, and J. Swings, "Synopsis on the taxonomy of the genus *Xanthomonas*," *Phytopathology* **90**:677-682 (2000).
- <sup>21</sup> G.E. Fox, J.D. Wisotzkey, and P. Jurtshuck Jr., "How close is close: 16S rRNA sequence identity may not be sufficient to guarantee species identity," *International Journal of Systematic Bacteriology* **42**:166-170 (1992).
- <sup>22</sup> D. Xu and J.C. Cote, "Phylogenetic relationships between *Bacillus* species and related genera inferred from comparison of 3' end 16S rDNA and 5' end 16S-23S ITS nucleotide sequence," *International Journal of Systematic and Evolutionary Microbiology* **53**:695-704 (2003).
- <sup>23</sup> M.N. Widjojoatmodjo, A.C. Fluit, and J. Verhoef, "Rapid identification of bacteria by PCR-single-strand conformation polymorphism," *J Clin Microbiol.* **32**:3002-3007 (1994).

- 
- <sup>24</sup> A.-K. Järvinen, S. Laakso, P. Piiparinen, A. Aittakorpi, M. Lindfors, L. Huopaniemi, H. Piiparinen, and M. Mäki, “Rapid identification of bacterial pathogens using a PCR- and microarray-based assay,” *BMC Microbiology* **9**:161-176 (2009).
- <sup>25</sup> D.E. Ost, D. Poch, A. Fadel, S. Wettimuny, C. Ginocchio, and X.-P. Wang, “Mini-bronchoalveolar lavage quantitative polymerase chain reaction for diagnosis of methicillin-resistant *Staphylococcus aureus pneumonia*,” *Critical Care Medicine* **38**:1536-1541 (2010).
- <sup>26</sup> K. Kaneko, O. Qndera, T. Miyatake, and S. Tsuji, “Rapid diagnosis of tuberculosis meningitis by polymerase chain reaction (PCR),” *Neurology* **40**:1617-1618 (1990).
- <sup>27</sup> R. Goodacre, E.M. Timmins, R. Burton, N. Kaderbhai, A.M. Woodward, D.B. Kell, and P.J. Rooney, “Rapid identification of urinary tract infection bacteria using hyperspectral whole-organism fingerprinting and artificial neural networks,” *Microbiology* **144**:1157-1170 (1998).
- <sup>28</sup> J.O. Lay, “MALDI-TOF mass spectrometry of bacteria,” *Mass Spectrometry Reviews* **20**:172-194 (2001).
- <sup>29</sup> V. Ruelle, B. El Moulaj, W. Zorzi, P. Ledent and E. De Pauw, “Rapid identification of environmental bacterial strains by matrix-assisted laser desorption/ionization time-of-flight mass spectrometry,” *Rapid Communications in Mass Spectrometry* **18**:2013-2019 (2004).
- <sup>30</sup> S.J. Rehse, Q.I. Mohaidat, and S. Palchadhuri, “Towards the clinical application of laser-induced breakdown spectroscopy for rapid pathogen diagnosis: the effect of mixed cultures and sample dilution on bacterial identification,” *Applied Optics* **49**:C27-C35 (2010).
- <sup>31</sup> Q. Mohaidat, S.J. Rehse, S. Palchadhuri ”The effect of bacterial environmental and metabolic stresses on a LIBS-based identification of *Escherichia coli* and *Streptococcus viridans*,” *Applied Spectroscopy* **65**: 386-392 (2011).
- <sup>32</sup> L. Mariely, J.P. Signolle, C. Amiel, and J. Travert, “Discrimination, classification, identification of microorganisms using FTIR spectroscopy and chemometrics,” *Vibrational Spectroscopy* **26**:151-159 (2001).
- <sup>33</sup> K. Maquelin, C. Kirschner, L.-P. Choo-Smith, N. van den Braak, H.P. Endtz, D. Naumann, and G.J. Pupples, “Identification of medically relevant microorganisms by vibrational spectroscopy,” *Journal of Microbiological Methods* **51**:255-271 (2002).
- <sup>34</sup> R. Petry, M. Schmitt, and J. Popp, “Raman spectroscopy - a prospective tool in the life sciences,” *ChemPhysChem*. **4**:14-30 (2003).

- 
- <sup>35</sup> D. Pappas, B.W. Smith, and J.D. Winefordner, "Raman spectroscopy in bioanalysis," *Talanta* **51**:131–144 (2000).
- <sup>36</sup> M.S. Ibelings, K. Maquelin, H.P. Endtz, H.A. Bruining, and G.J. Puppels, "Rapid identification of *Candida* spp. in peritonitis patients by Raman Spectroscopy," *Clinical Microbiology and Infection* **11**:353-358 (2005).
- <sup>37</sup> K. Maquelin, C. Kirschner, L.P. Choo-Smith, N.A. Ngo-Thi, T. van Vreeswijk, M. Stammeler, H.P. Endtz, H.A. Bruining, D. Naumann, and G.J. Puppels, "Prospective study of the performance of vibrational spectroscopies for rapid identification of bacterial and fungal pathogens recovered from blood cultures," *Journal of Clinical Microbiology* **41**:324-329 (2003).
- <sup>38</sup> K. Maquelin, L.P. Choo-Smith, T. van Vreeswijk, H.P. Endtz, B. Smith, R. Bennett, H.A. Bruining, and G.J. Puppels, "Raman spectroscopic method for identification of clinically relevant microorganisms growing on solid culture medium," *Analytical Chemistry* **72**:12-17 (2000).
- <sup>39</sup> R.M. Jarvis and R. Goodacre, "Ultra-violet resonance Raman spectroscopy for the rapid discrimination of urinary tract infection bacteria," *FEMS Microbiology Letters* **232**:127-132 (2004).
- <sup>40</sup> H. Yang and J. Irudayaraj, "Rapid detection of foodborne microorganisms on food surface using Fourier transform Raman spectroscopy," *Journal of Molecular Structure* **646**:35-43 (2003).
- <sup>41</sup> E.C. Lopez-Diez and R. Goodacre, "Characterization of microorganisms using UV resonance Raman spectroscopy and chemometrics," *Analytical Chemistry*. **76**:585-591 (2004).
- <sup>42</sup> Q. Wu, T. Hamilton, W.H. Nelson, S. Elliott, J.F. Sperry, and M. Wu, "UV Raman spectral intensities of *E. coli* and other bacteria excited at 228.9, 244.0, and 248.2 nm," *Analytical Chemistry* **73**:3432-3440 (2001).
- <sup>43</sup> U. Neugebauer, U. Schmid, K. Baumann, U. Holzgrabe, W. Ziebuhr, S. Kozitskaya, W. Kiefer, M. Schmitt, and J. Popp, "Characterization of bacterial growth and the influence of antibiotics by means of UV resonance Raman spectroscopy," *Biopolymers* **82**:306–311 (2006).
- <sup>44</sup> A.C. Williams and H.G. Edwards, "Fourier transform Raman spectroscopy of bacterial cell walls," *Journal of Raman Spectroscopy* **25**:673-677 (1994).
- <sup>45</sup> R.M. Jarvis and R. Goodacre, "Discrimination of bacteria using surface enhanced Raman spectroscopy," *Analytical Chemistry* **76**:40-47 (2004).

- 
- <sup>46</sup> E. Consuelo and R. Goodacre, "Characterization of microorganisms using UV resonance Raman spectroscopy and chemometrics," *Analytical Chemistry* **76**:585-591 (2004).
- <sup>47</sup> K.C. Schuster, I. Reese, E. Urlaub, J.R. Gapes, and B. Lendle, "Multidimensional information on the chemical composition of single bacterial cells by confocal Raman microspectroscopy," *Analytical Chemistry* **72**:5529-5534 (2000).
- <sup>48</sup> A.C. Singer, W.E. Huang, J. Helm, and I.P. Thompson, "Insight into pollutant bioavailability and toxicity using Raman confocal microscopy," *Journal of Microbiological Methods* **60**:417-422 (2005).
- <sup>49</sup> J. Goeller and M.R. Riley, "Discrimination of bacteria and bacteriophages by Raman spectroscopy and surface-enhanced Raman spectroscopy," *Applied Spectroscopy* **61**:679-685 (2007).
- <sup>50</sup> W.E. Huang, R.I. Griffiths, I.P. Thompson, M.J. Bailey, and A.S. Whiteley, "Raman microscopic analysis of single microbial cells," *Analytical Chemistry* **76**:4452-4458 (2004).
- <sup>51</sup> M. Harz, P. Rosch, K. Peschke, O. Ronneberger, H. Bukhardt, and J. Popp, "Micro-Raman spectroscopic identification of bacterial cells of the genus *Staphylococcus* and dependence on their cultivation conditions," *Analyst* **130**:1543-1550 (2005).

## **Chapter 2**

### **Theoretical Background and Experimental Instrumentation**

This chapter will begin with the theoretical background of Raman spectroscopy, then an overview of the Raman instrumentation that has been used for this work. Afterward bacterial physiology, which represents the target material for all the Raman studies conducted in this work, will be reviewed.

#### **2.1 Raman Spectroscopy**

Raman spectroscopy (RS) is a powerful molecular fingerprinting technique which analyzes materials through the interaction of the material's molecules with an incident laser beam.<sup>1</sup> The applications of RS are incredibly diverse, from the study of minerals<sup>2</sup> to the characterization of polymers<sup>3</sup> to medicine.<sup>4</sup> An exhaustive list of the uses and applications of RS is impossible to compile. Although it has been used for a long time for the chemical characterization of different materials, it has just lately been applied to the study of biological samples in order to provide a rapid all-optical identification and discrimination of pathogenic organisms. This is due to the development of increasingly sophisticated, powerful, fast, and portable Raman spectroscopy instrumentation and statistical techniques that are used to analyze the data. The need for a robust detection technique of bacteria has become more important than ever due to the increase of potential bioterrorism threats<sup>5</sup> and the high mortality rate of bacterial infections worldwide. For example, in 2004 26% of the worldwide annual deaths were caused by infectious diseases.<sup>6</sup>

### 2.1.1 Theoretical Background

The Raman effect has been known and exploited for many years, and the physics behind it are very well understood.<sup>7</sup> In 1923 Smekal discovered the inelastic scattering theoretically<sup>8</sup> and in 1928 Raman and Krishnan reported the observation of this effect which has been called “Raman scattering” since then.<sup>9</sup> Since the Raman scattering effect is very weak, its widespread applications did not appear until the 1960s after the laser invention. By the 1980s Raman spectroscopy was being successfully used for materials characterization after the invention of sensitive detectors and optical components.<sup>10</sup>

The Raman effect is caused by the inelastic scattering that occurs when incident light (assume monochromatic laser radiation) of wavelength  $\lambda_0$  and frequency  $f_0$  is scattered from the vibrating molecules of the sample. The displacement of the normal coordinates of those molecules about their equilibrium position due to a specific vibrational mode may be expressed in equation 1.1,

$$\Delta q = q_0 \cos(2\pi f_m t) \quad 1.1$$

where  $f_m$  is the frequency of the vibrational mode and  $q_0$  is the vibrational amplitude. The electric field of the laser beam oscillates with time ( $t$ ) and is given by equation 1.2,

$$E = E_0 \cos(2\pi f_0 t) \quad 1.2$$

where  $E_0$  is the amplitude of the oscillating electric field. This electric field will induce an electric dipole moment  $P$  in the molecule which is given by equation 1.3.

$$P = \alpha E \quad 1.3$$

The proportionality constant  $\alpha$  is called the molecular polarizability and is a material property that depends on the material structure and bond nature.  $\alpha$  can be expanded around the normal coordinate of the vibrating molecule for small amplitudes of vibration as given by equation 1.4,

$$\alpha = \alpha_0 + \left( \frac{\partial \alpha}{\partial q} \right)_0 \Delta q + \dots \quad 1.4$$

where  $\alpha_0$  is the polarizability of the molecular mode at equilibrium position. Based on equations 1.1, 1.2, and 1.4, equation 1.3 becomes

$$P = \alpha_0 E_0 \cos(2\pi f_0 t) + \frac{1}{2} \left( \frac{\partial \alpha}{\partial q} \right)_0 q_0 E_0 [\cos(2\pi \{f_0 + f_m\} t) + \cos(2\pi \{f_0 - f_m\} t)] \quad 1.5$$

This equation represents an oscillating dipole which radiates photons with three different frequencies, namely  $f_0$  (elastic scattering) in the first term,  $(f_0 + f_m)$  (inelastic scattering with shorter wavelength) in the second term, and  $(f_0 - f_m)$  (inelastic scattering with longer wavelength) in the third term. As can be observed in equation 1.5, the Raman effect which is associated with the inelastic scattering occurs only if  $\left( \frac{\partial \alpha}{\partial q} \right)_0 \neq 0$ , which means that the polarizability must change with vibrational displacement to get what is called a ‘‘Raman active mode.’’ The Raman active band intensity ( $I$ ) is proportional to the square of the rate of change of the polarizability with respect to the change of the displacement  $\left( \frac{\partial \alpha}{\partial q} \right)_0^2$ . The theoretical value of Raman scattering intensity will depend on the molecular composition of the sample, the molecule’s specific vibrational modes, the power of the excitation source (typically a laser), and on the laser wavelength since the intensity is proportional to the fourth power of the laser frequency.<sup>10</sup> Also,

the experimentally measured Raman intensity will depend not just on the Raman scattering intensity, but also on the experimental instrumentation such as the detector and optics efficiency.

The change in the frequency between the incident and emitted light ( $\Delta f$ ) is called the Raman shift, and the magnitude of this change is determined by the various vibrational modes of the molecules in the sample. The Raman shift is typically measured in units of  $\text{cm}^{-1}$  (although it is really a wavelength shift that is measured). Equation 1.6 gives the value of Raman shift in terms of the incident and scattered photon wavelength.

$$\Delta f \left( \text{cm}^{-1} \right) = \left( \frac{1}{\lambda_{\text{incident}} \text{ (nm)}} - \frac{1}{\lambda_{\text{scattered}} \text{ (nm)}} \right) \times 10^{-7} \quad 1.6$$

Most of the incident photons will scatter elastically with no change in frequency (Rayleigh scattering), while a small portion of light ( $\sim 10^{-8}$  of the incident beam) will scatter inelastically, which is called Raman scattering. If the scattered light has more energy than the incident light, the difference in the energy will destruct a phonon which changes the vibrational state of the molecule and as a result we will observe anti-Stokes lines. The anti-Stokes lines, having more energy than the incident light, will have a shorter or more blue wavelength. Stokes lines occur when the scattered photons have less energy than the incident photons and the difference in the energy will create a phonon. These Stokes lines will have a longer or more red wavelength than the incident light.<sup>7</sup> In general the Stokes lines are considerably more intense than the anti-Stokes lines at standard temperature, since the lowest vibrational states have more occupation probability. Due to this fact, the Raman spectra shown in this dissertation will contain the Stokes lines only.

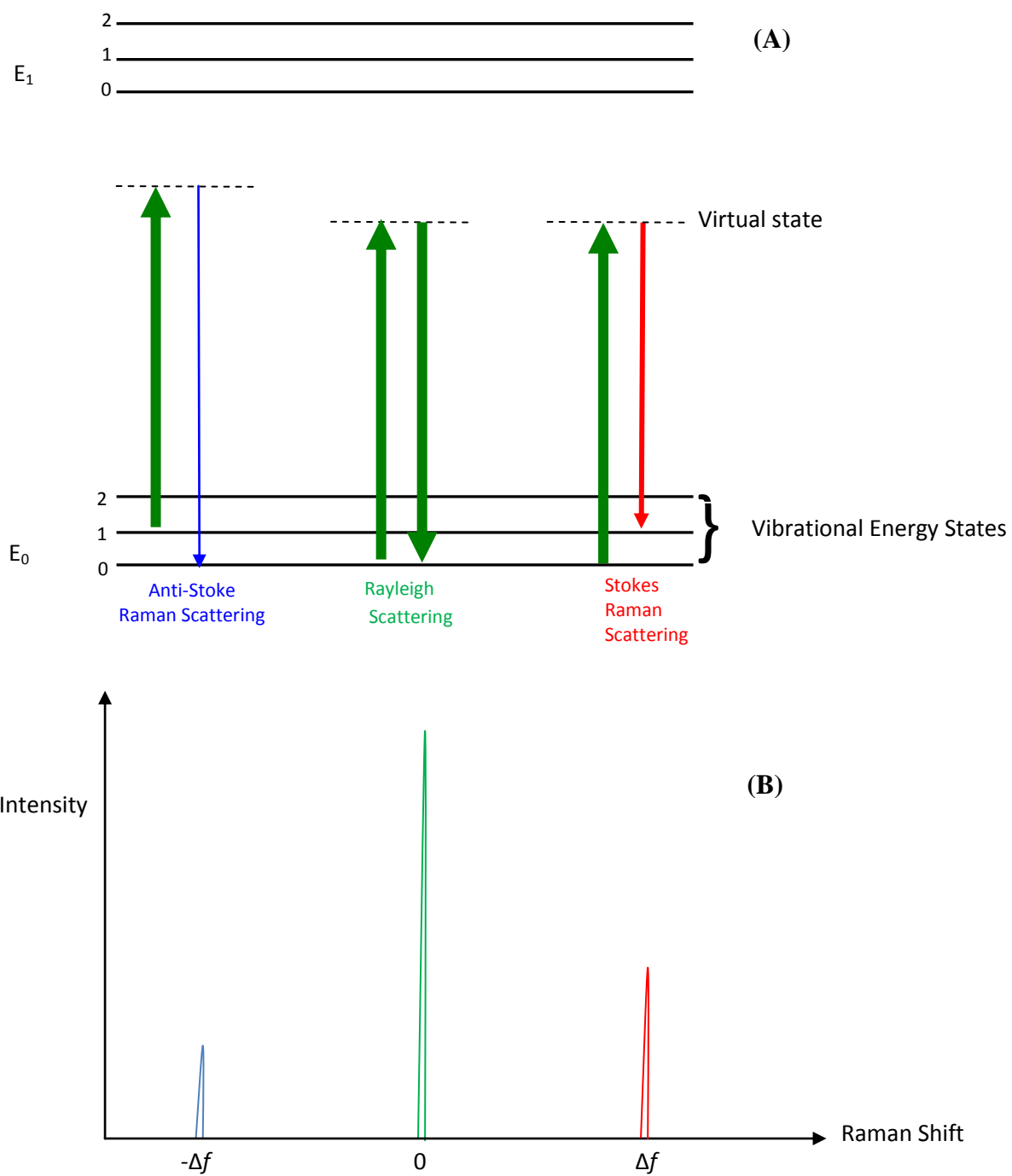


**Figure 2.1:** (A) Energy level diagram showing the states involved in Raman scattering, (B) Raman spectrum representing Stokes and anti-Stokes scattering.

Figure 2.1(A) shows a simple model of the light scattering mechanism where the incident photon puts the molecular system into a virtual energy state which is generally not equal to any electronic energy state (dashed lines located between the ground electronic state  $E_0$  and the first excited state  $E_1$ ) and has a very short lifetime, about  $10^{-14}$  seconds. A representative Raman spectrum (plot of the number of scattered photons (intensity) versus Raman shift) is shown in Figure 2.1(B) where the intensity of Rayleigh scattering is suppressed to show Stokes and anti-Stokes lines. Examples of actual Raman spectra are shown below.

Si has a very simple Raman spectrum which consists of only one peak. Figure 2.2(A) shows a full Raman scan. Even after filtering the Rayleigh scattering out of the collected light with high extinction, the Rayleigh line still has a much bigger intensity than the Si Stokes line. Consequently, all measurements should start from a positive value of Raman shift (e.g.  $100\text{ cm}^{-1}$ ) to avoid the appearance of this huge peak. Figure 2.2(B) shows a more detailed view of the Si Raman peak located at  $520\text{ cm}^{-1}$ .

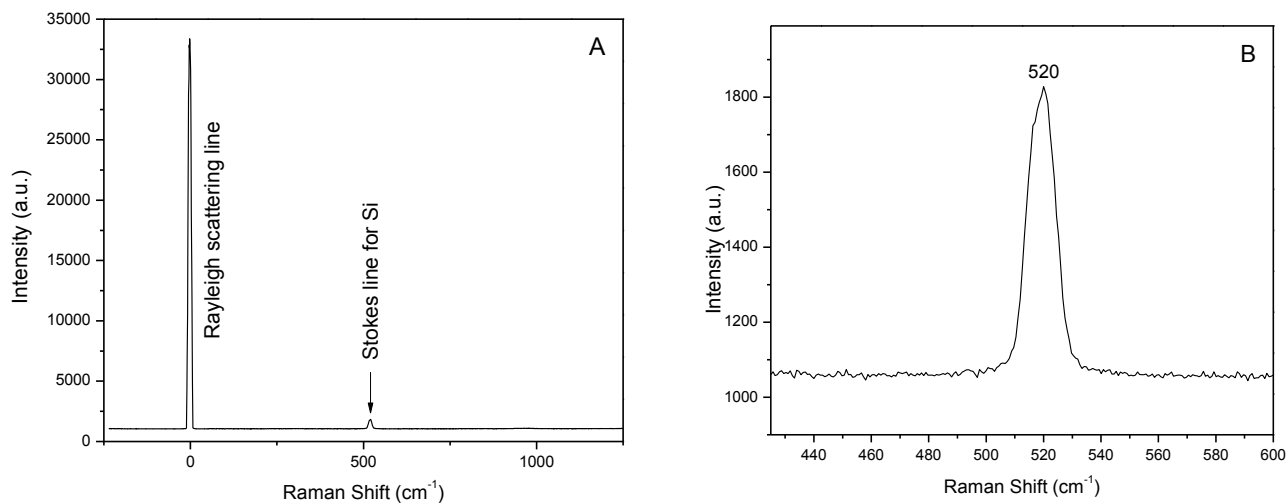


**Figure 2.2:** (A) Raman spectrum of Si wafer in the spectral range ( $-250$ - $1200\text{ cm}^{-1}$ ), (B) Si peak at  $520\text{ cm}^{-1}$ .

Because the Si line is so well isolated and its Raman shift is so well-measured, this peak is often used for spectral calibration. Most substances do not give such a “clean” Raman spectrum. Figure 2.3 shows a Raman spectrum of a kind of sugar called sucrose, it can be noticed that this spectrum consists of many complex features reflecting the complex structure of this sugar.

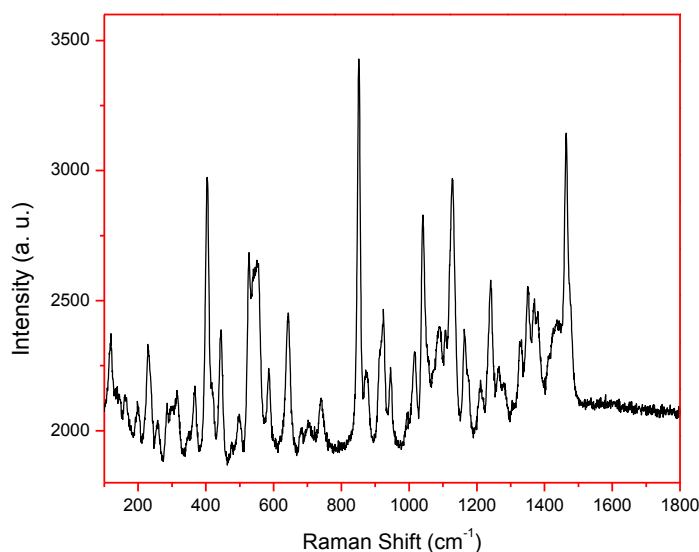


**Figure 2.3:** Raman spectrum of sucrose.

### 2.1.2 Raman Signal Enhancement

As mentioned earlier, Raman scattering is inherently a very weak or inefficient process since only 1 out of every  $10^8$  photons is scattered inelastically. Also, Raman spectra for biological samples typically suffer from high fluorescence backgrounds due to the presence of fluorophore molecules in biological macromolecules which have the ability to absorb light to be excited to a vibrational level located within an excited energy state and then re-emit it with different frequency (causing fluorescence).<sup>11,12</sup> Figure 2.4 shows an example of a bacterial

Raman spectrum suffering from huge fluorescence (the large background upon which the smaller peaks are present).

Many experimental techniques have been developed to address these problems. One way

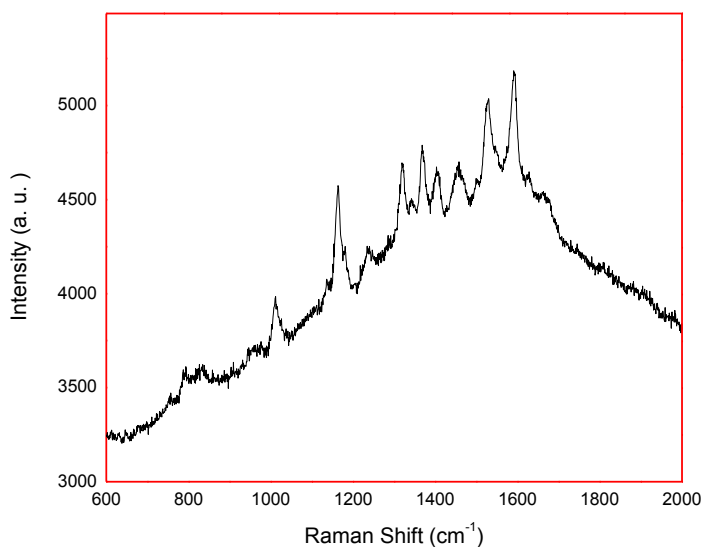


**Figure 2.4:** Raman spectrum of bacterial sample.

to reduce the fluorescence is to choose the laser wavelength to be in the ultraviolet (UV) or infrared (IR) regions. To do this one must take into consideration that the detector sensitivity would typically be less for IR Raman, while the high energy of UV laser could damage the biological samples. On the other hand, the Raman signal intensity is proportional to the fourth power of the laser frequency,<sup>10</sup> so the use of a short wavelength laser (in the UV region) would help to enhance the signal considerably. As a result UV resonance Raman spectroscopy has been used for microorganism identification since the late 1980s.<sup>13,14,15,16</sup>

Another technique used to enhance the Raman signal of a specific band that has received special interest is Coherent Anti-Stokes Raman spectroscopy (CARS). In CARS, two coherent lasers are used to excite the sample. One of them has a constant wavelength (frequency) while

the other has a changeable, or tunable frequency. In order to enhance the intensity of the required Raman-active mode, the frequency of the band should match the difference between the frequencies of the two lasers. The interaction of the two laser beams with the sample will lead to a strong anti-Stokes lines for the vibrational mode with a frequency equal to the frequency difference between the two beams.<sup>17</sup> The main drawback of CARS is the dominant non-resonance background contributed from the substrate or other vibrational modes.<sup>18</sup>

### **2.1.2.1 Surface Enhanced Raman Spectroscopy (SERS)**

The most common and widely used way to amplify the weak Raman signal is to attach the sample to a metallic rough surface which can enhance the Raman signal greatly and quench the fluorescence.<sup>19</sup> This technique is called surface enhanced Raman spectroscopy (SERS).<sup>20</sup> This technique was investigated to enhance the Raman intensity from the bacterial samples in this dissertation, therefore a thorough explanation of the technique is provided here.

Since the signal intensity is proportional to the square of the induced dipole moment ( $P$ ), the enhancement can be achieved by increasing the electric field ( $E$ ) or the molecular polarizability ( $\alpha$ ) or both of them.<sup>7</sup> The electromagnetic field can be enhanced by using a rough surface of metal. The incident laser will excite the conduction electrons of the surface and create a plasmon resonance (collective excitation of conductive electrons in small metallic structure) which makes the rough surface polarized and causes a large electromagnetic field.<sup>21</sup> The second mechanism of enhancement is called “chemical enhancement” which is due to the charge transfer interaction between the metal and the adsorbed molecules or bond formation between the metal and adsorbate that causes an increase in the molecular polarizability.

The enhancement effect depends on the physical properties of the substrate. Rather than using a nano-roughened surface, the most common nanostructured substrates used for SERS are

actually suspensions of gold and silver nanoparticles, the attachment of these nanoparticles could enhance the signal by  $10^3$ - $10^6$  fold and quench the fluorescence.<sup>22,23,24</sup> The spectra obtained

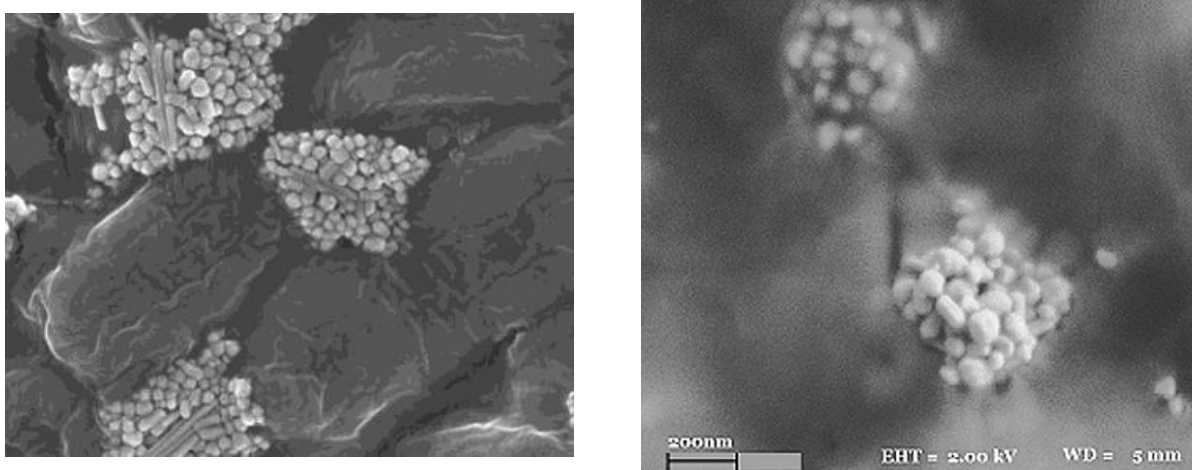


**Figure 2.5:** SEM images of the aggregated silver nanoparticles on *E. coli* bacteria.

using SERS suffer from irreproducibility due to the inhomogeneity of the bacteria and colloidal suspension. To address this problem, scanning electron microscope imaging can be used to locate the regions of bacteria and colloids together and strike the sample at those points. An example of such SEM images showing the colloidal nanoparticles is shown in Figure 2.5.<sup>24,25</sup>

To show one example, the SERS spectra of bacteria was compared to its normal Raman spectra by Dutta et al. and an enhancement in Raman signal was reported.<sup>26</sup> Figure 2.6 reveals the intensity enhancement caused by incorporation of ZnO nanoparticles (next page).

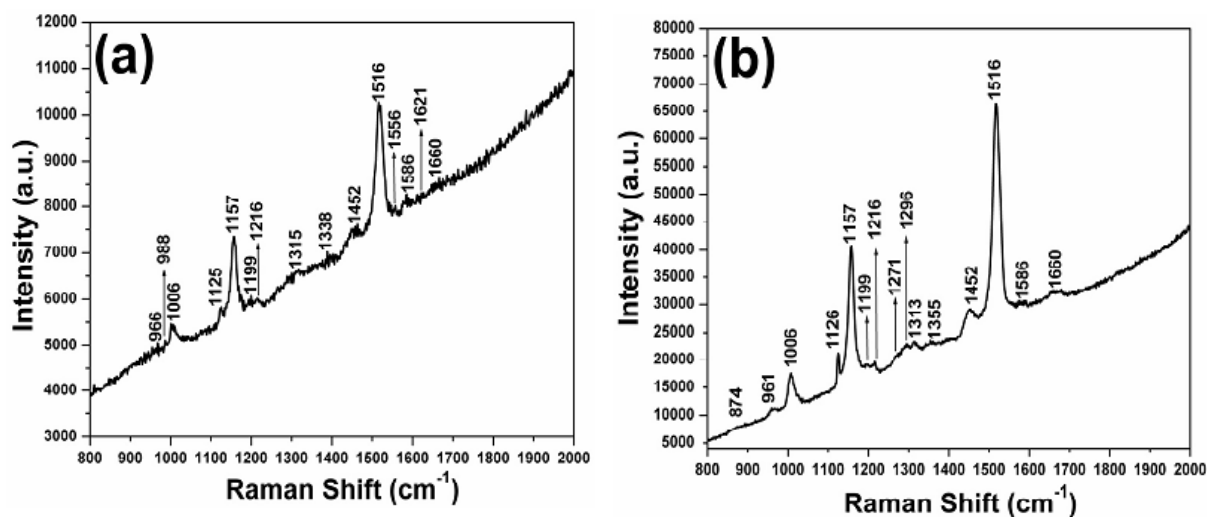


**Figure 2.6:** Comparison of relative Raman spectra of (a) bulk Raman spectrum and (b) SERS spectrum of *E. coli* cells.

## 2.2 Molecular Vibrations

Molecules consist of atoms attached by chemical bonds. The atoms experience a periodic motion even if the molecule has no translational or rotational motion. This periodic motion is called molecular vibration and its frequency is called the vibration frequency or vibrational frequency. In general, for each molecule with  $N$  atoms there are  $3N$  degree of freedom for its translational, rotational, and vibrational motion. Three of these degrees of freedom are for the molecular translation in the  $x$ ,  $y$ , and  $z$  directions and three for the molecular rotation around these axes. In the case of a linear molecule there are two rotational motions only. The remaining degrees of freedom correspond to independent vibrational normal modes. Namely, a non-linear molecule has  $3N-6$  normal modes and a linear molecule has  $3N-5$  normal modes.<sup>27</sup> The frequency of a specific normal mode depends on the bond strength and the mass of the involved atoms. The distinctive frequency of each Raman active vibrational mode is what is being

measured experimentally using Raman spectroscopy in units of wave number ( $\text{cm}^{-1}$ ).<sup>28</sup> The vibrational modes represent complex changes of the atoms' positions relative to each other, and some of them are described below.

(1) Stretching modes: In this mode the bond length between two atoms will change in a symmetric or asymmetric way. It has higher energy than the other modes since it is harder to compress or stretch the bond than to bend it.

(2) Bending mode: In this case the angle between two bonds will change periodically while the bond length stays unchanged; this includes in-plane and out-of-plane bending. In-plane bending includes "scissoring," where the atoms move in opposite directions which leads to a change in the angle between them and "rocking," where the atoms move in the same direction so the angle between them and the rest of the molecule will change. The out-of-plane bending includes "wagging," which represents the change of the angle between the plane of a certain group of atoms and a plane through the rest of the molecule and "twisting," which represents the change of the angle between the planes of two groups of atoms.

These vibrations can be difficult to visualize, so they are shown here for a given molecule. For example the simple organic molecule ( $\text{O}=\text{CH}_2$ ) has 6 normal vibrational modes illustrated in Figure 2.7 (next page).

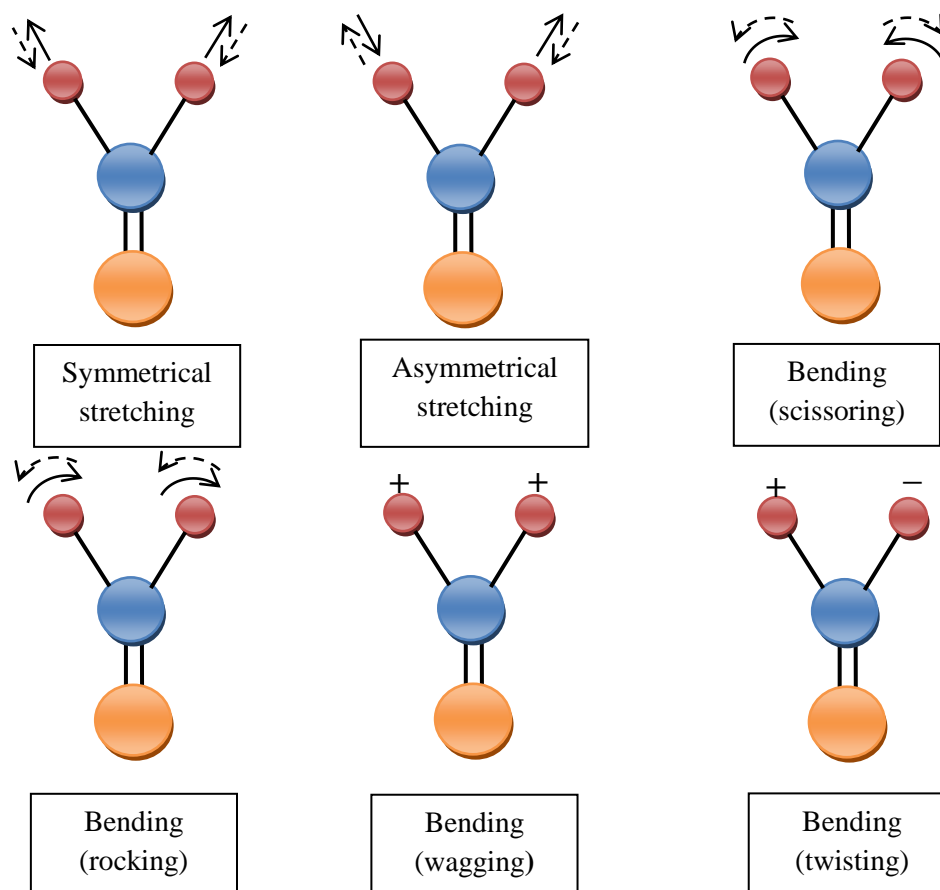


**Figure 2.7:** A simple model representing the vibrational modes of an organic molecule ( $\text{O}=\text{CH}_2$ ).

Due to the complex molecular structure of biological samples, their Raman spectra are composed of broad overlapping bands representing different vibrational modes of a multitude of different molecules. This makes the identification of specific vibrational modes not so straightforward.

## 2.3 Raman Spectroscopy Instrumentation

The main generic apparatus of a Raman spectroscopy experiment are: excitation source (laser), optical components, spectrometer, and the processing system (CCD detector and computer). A typical Raman experimental setup is shown in figure 2.8.

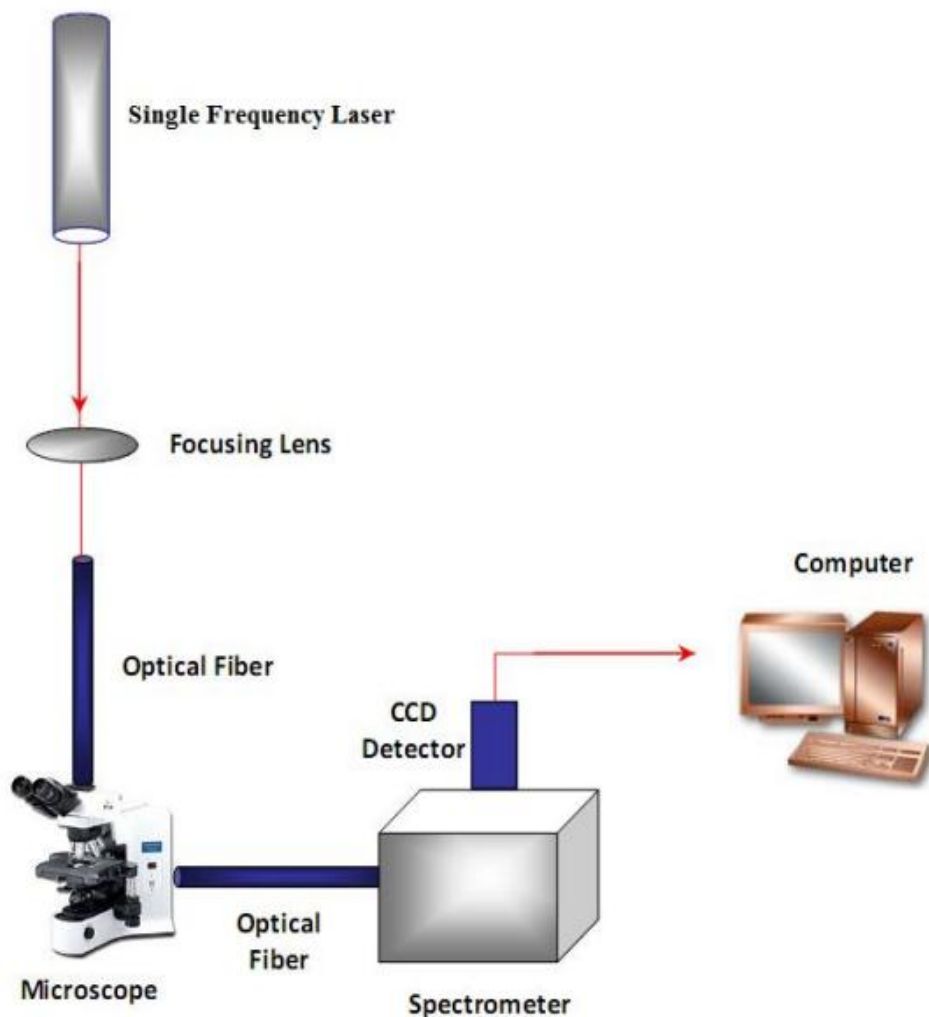


**Figure 2.8:** A typical Raman spectroscopy setup.

Almost all experiments utilize some variation of this basic setup.<sup>29</sup> The specific apparatus used in my experiments are described below.

### 2.3.1 Excitation Source

A laser is used to excite Raman spectra by supplying a coherent beam of a single wavelength of light that has sufficient power to produce Raman scattering. We use a continuous-wave argon-ion laser that operates in the visible region (514.5 nm). Figure 2.9 shows a scheme of this laser contents (power supply, gain medium (Ar gas), and resonant cavity).

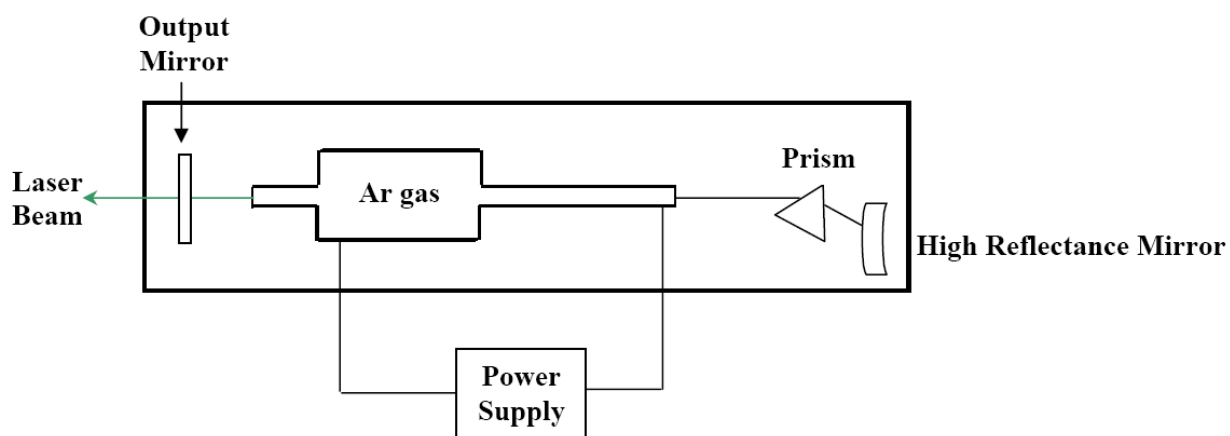


**Figure 2.9:** A schematic diagram of an Ar-ion laser.

The energy source supplies power to the gain medium, which is an Ar gas plasma in a tube. A high current ionizes the gas and provides the energy to excite Ar ions from the ground state to the upper laser level through the collisions between the current electrons and Ar gas atoms. A schematic diagram of the relevant energy levels is shown in Figure 2.10. The excitation process occurs in two steps, the first one removes one electron from an Ar atom in the  $3p^6$  ground state. This leads to  $Ar^+$  ground state (Ar excitation). The second process leads to a transition of another electron from  $3p^5$  to  $4s$  or  $4p$  states ( $Ar^+$  excitation). Also indirect process can lead to  $Ar^+$  excitation, such as the decay from upper excited levels and the excitation from metastable states. An accumulation of  $Ar^+$  in the metastable  $4p$  state will take place due to the

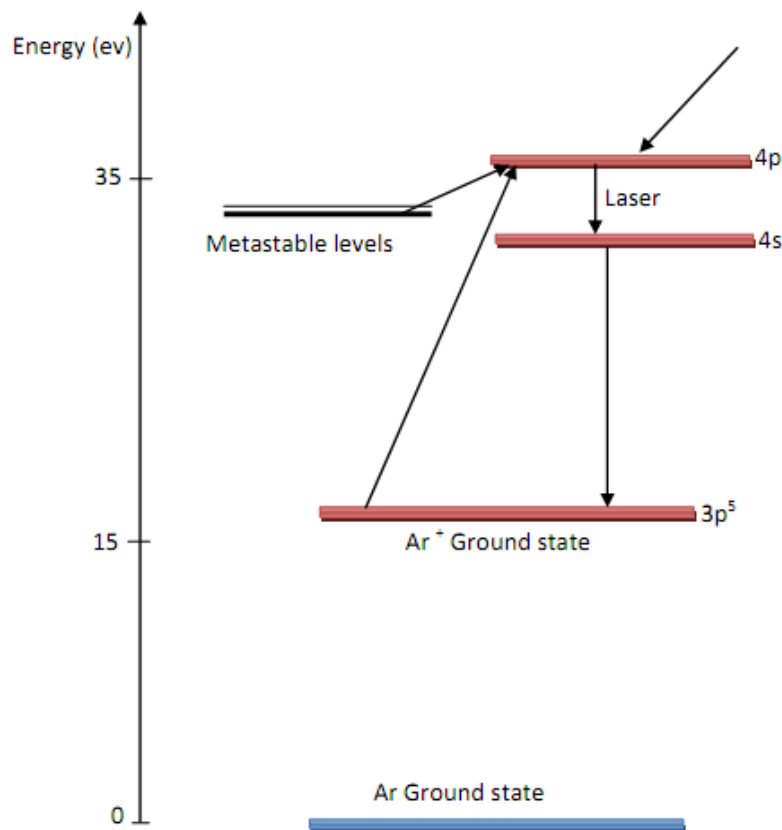


**Figure 2.10:** Energy level diagram of Ar-ion Laser.

long lifetime of this state compared to that of 4s state and as a result a laser transition from 4p to 4s state can be achieved. The resultant laser will oscillate with different wavelengths since the 4p and 4s states contain many sublevels. The green laser transition at 514.5 nm wavelength is the most intense one.<sup>30</sup> The resonant cavity surrounding the Ar tube contains a mirror with high reflectance (99.99%) and an output mirror which can transmit a part of the cavity energy. The emitted photons will bounce back and forth between the mirrors and interact with the excited ions which cause photon amplification, and there is a prism located between the mirrors to select a desired wavelength for single-frequency operation.

The specific argon-ion laser used of the majority of the experiments in this dissertation was a STELLAR-PRO-L Modu-laser (pictured in Figure 2.11) with the specification given in table 2.1.



**Figure 2.11:** Picture of Modu-laser.

Table 2.1: The specifications of the Modu-laser Ar-ion laser.

Wavelength	514 nm
Mode	TEM <sub>00</sub>
Maximum power	100 Mw
Beam diameter	0.75 mm
Beam divergence	0.95 mrad
Beam amplitude noise	< 1% RMS
Warm-up time	<15 min
Start delay	30 sec
Beam output power drift (after warm-up)	< ±1%
Beam height	2.375"
AC line voltage	200-265 V
Line frequency	50-60 Hz
Case dimensions	7.6"×5.36"×19.18"
Total weight	22.5 lbs

### 2.3.2 Optical Components

The optical components consist of a lens/optical fiber system to deliver the laser to the microscope, a commercial Raman-adapted microscope, and an optical fiber system to carry Raman scattered light to a spectrometer. These are described here.

A focusing lens focuses the laser beam coming from the laser into a jacketed optical fiber. This fiber carries the argon-ion laser beam into the microscope. Figure 2.12 shows this apparatus. A horizontal-vertical translation stage holds the fiber end and this should be adjusted to position the fiber end in the laser focus to get the maximum amount of laser power into the

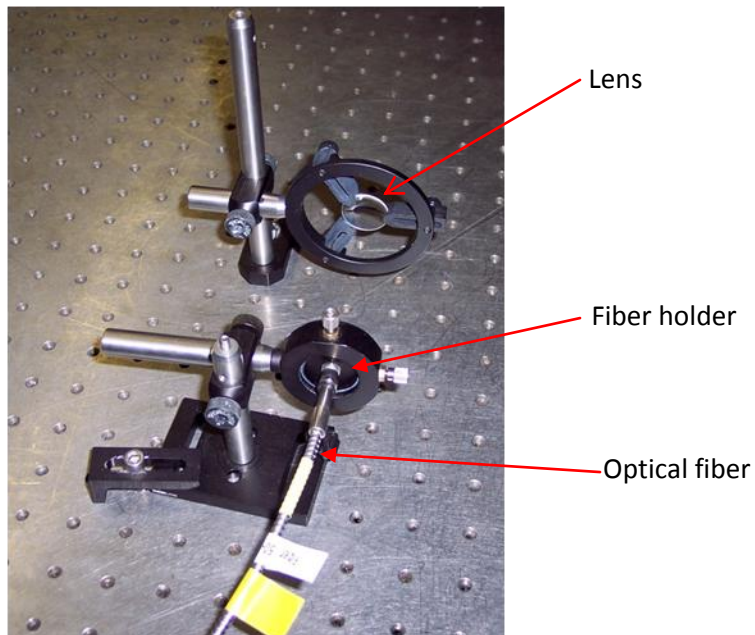


**Figure 2.12:** A picture of lens and optical fiber.

fiber. The fiber is a metal-jacketed single-mode optical fiber with  $TEM_{00}$  output (lowest order transverse mode with a small rounded spot size) which allows optimal focusing of the laser beam by the microscope objective.<sup>31</sup>

An Raman-adapted optical microscope (Olympus BX41TF) with three objectives (10X, 50X, and 100X) is used to focus the laser spot on the sample and collect the scattered light from

the sample (pictured in Figure 2.13). The microscope is equipped with several custom optics, including a notch filter and a bandpass filter that are used to filter out the Rayleigh scattered light from the scattered light.

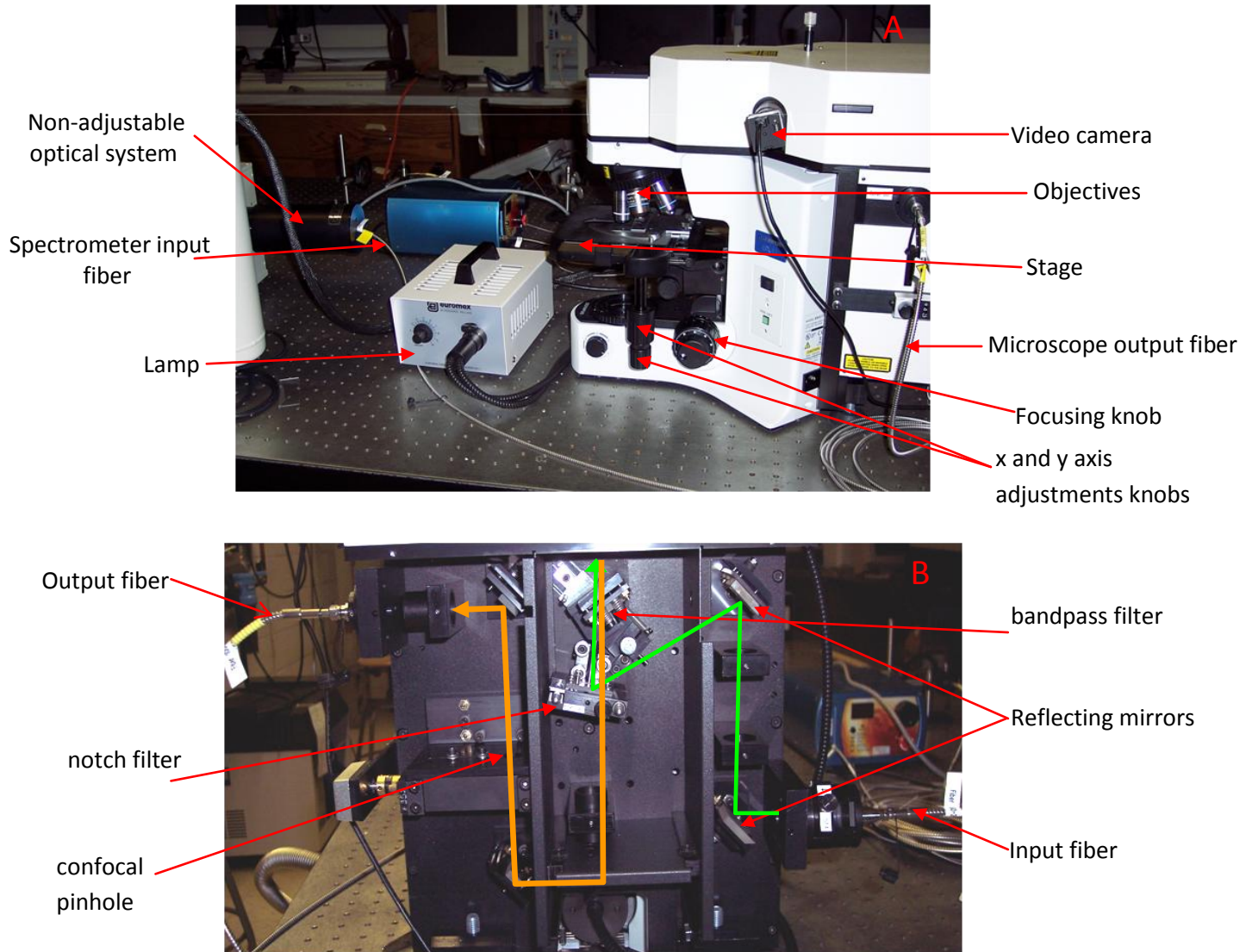


**Figure 2.13:** (A) a picture of the Raman microscope from outside, (B) a picture of the components inside the microscope. The path of the laser is shown in green. The path of the Raman scattered light is shown in orange.

Lastly, another metal jacketed optical fiber carries the Raman scattered light from the microscope to a spectrometer, and the light from the fiber is focused into the spectrometer by an optical system built into the spectrometer. This rigid design never requires adjustment by the user. The optical fibers serve as a source and detector aperture with stable and robust laser alignment.

### **2.3.3 Spectrometer**

A TRIAX550 spectrometer (Jobin Yvon Horiba Inc.) is used to analyze the Raman spectrum. Figure 2.14 (A) shows a picture of the spectrometer components and its schematic diagram is shown in Figure 2.14 (B) and figure 2.15 shows a picture of the whole unit (with camera). The TRIAX spectrometer is equipped with motorized entrance and exit slits, toroidal mirror, large exit focusing mirror, and three different diffraction gratings of 2400, 1800, and 1200 groves/mm mounted on an on-axis turret (just one of them is used during each scan). The availability of triple gratings provides the best compromise for the required spectral range and to get the best resolution (the ability of the spectrometer to resolve two close wavelengths). Another way to improve the resolution of the spectrometer is to increase the focal length of the instrument, the distance between the focusing mirror and the focal plane (exit slit). As the name implies, the TRIAX550 possesses a 0.55 m (550 mm) focal length optical system.

Light from the microscope is focused onto the entrance slit and is focused onto a diffraction grating by a curved mirror. The diffraction grating diffracts the scattered light into its various wavelength components with light of different wavelengths diffracting at different angles. This diffracted light is focused at different points at the exit slit using a large focusing mirror.

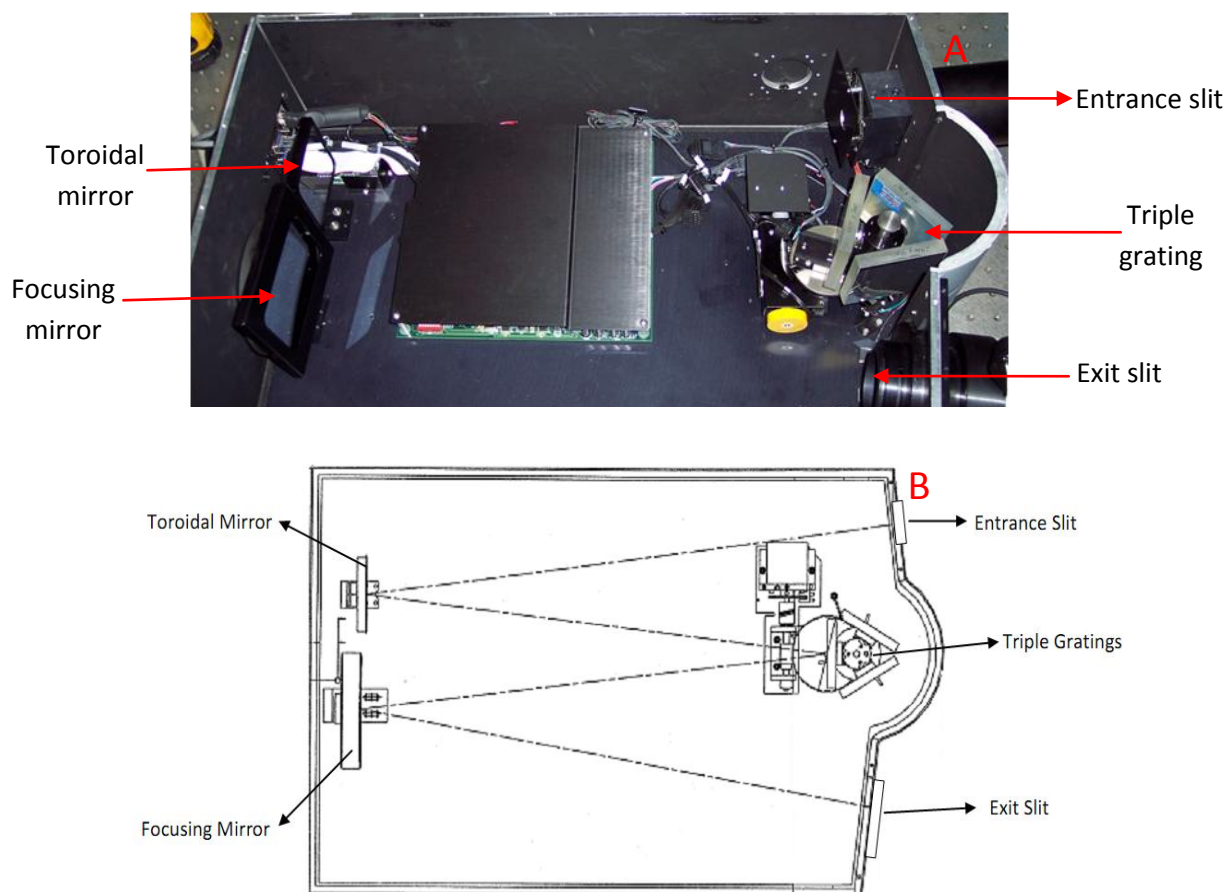


**Figure 2.14:** (A) a picture of spectrometer components, (B) a Schematic diagram of TRIAX550 spectrometer.



**Figure 2.15:** Picture of TRIAX550 spectrometer.

In our experiments the 1200 grooves/mm diffraction grating was mostly used. This

grating has a scanning range 0-1500 nm, 500 nm blaze, 0.03 nm resolution and 1.55 nm/mm dispersion. The typical size of the entrance slit was 250  $\mu\text{m}$  with entrance aperture ratio F/6.4 (called the F number, this represents the amount of light that can be collected).

### 2.3.4 Detector/Analysis

The light dispersed by the diffraction grating is focused onto a charge-coupled device (CCD) detector which is read out by a computer.<sup>32</sup> A CCD detector is a semiconductor that contains an array of photosensitive elements. When the photons hit a CCD element, a charge (photoelectron) will be created and stored there as a function of the photon number (light intensity). The amount of charge is counted and converted into a measurable analog voltage which is converted into a digital voltage and transferred to the memory of the computer. Our CCD camera utilizes a 1024 $\times$ 128 pixels liquid nitrogen cooled CCD array detector mounted on tiltable flanges and attached at the exit slit of the spectrometer to detect the dispersed Raman light. Computer software is used to control almost every aspect of acquiring the Raman

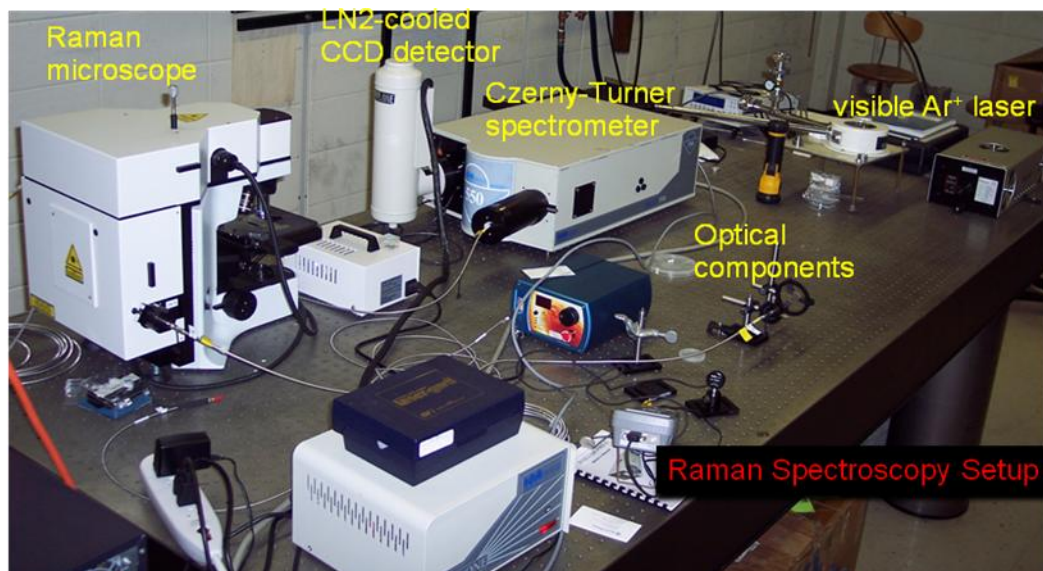


**Figure 2.16:** A picture of the home-built Raman spectroscopy instrumentation.

spectrum, from grating selection, to CCD readout. More details about this software will be discussed in the next chapter. A picture of our home-built Raman spectroscopy instrumentation is given in Figure 2.16.

Since Raman spectroscopy probes the molecular compositions of the bacterial cell, an overview of bacterial cell structure and its biochemical building blocks is needed for better understanding of the identification basis for this technique.

## 2.4 Bacteria Physiology

Although bacteria have different morphological forms such as rods (bacilli), spherical (cocci), spirals (spirilla), and chains (scanning electron microscope pictures of these different morphologies are shown in Figure 2.17 A,B<sup>33</sup> and C<sup>34</sup>), they have a general common structure that will be described below.

### 2.4.1 Bacteria Cell Structure and Biochemical Constituents

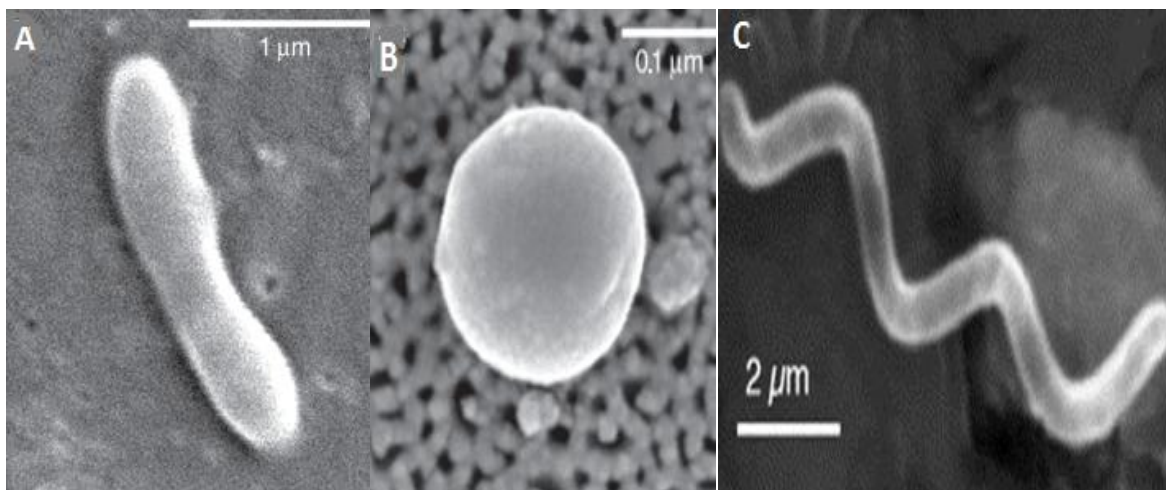


**Figure 2.17:** Scanning electron microscope (SEM) images of: (A) a rod-shaped bacterium, (B) a coccoid bacterium on a filter, (C) *R. rubrum* (a spiral-shaped bacterium).

The main structure of bacterial cells consists of the cell envelope, cytoplasm, and nucleoid (DNA). The cell envelope consists of the capsule, cell wall, and cell membrane and the cytoplasm contains the ribosomes (RNA and protein), enzymes, plasmid (DNA), and some inclusions which store nutrients and waste. Some bacteria have pili and flagella attached to the outer surface. Figure 2.18 shows the structure of a typical bacterial cell.

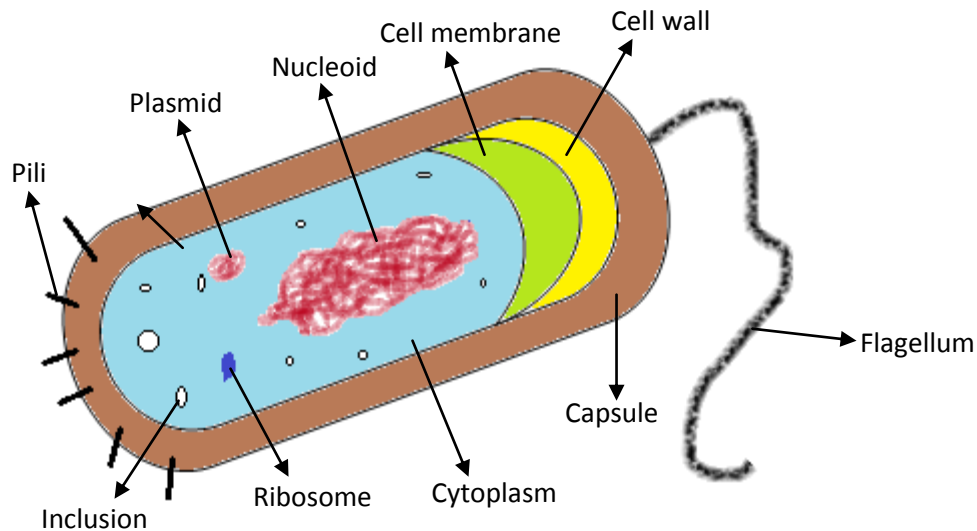


**Figure 2.18:** Bacteria Cell Structure

#### 2.4.1.1 Cell Envelope Structure

The cell envelope is a very important part of the cell that keeps it alive, so it is often considered an important target for antibiotics and host defenses. The contents of this part of the cell are described below:

- 1: The capsule is composed of polysaccharide and it plays a main role in keeping the cell from drying out, helping the cells to stick on the surfaces to develop a colony, and protecting the cells from the destruction by the host's defense system.

2: The bacterial cell wall is a unique complex rigid structure that gives the shape to the cell and provides the protection and support for the cell membrane. The reason for the wall rigidity of the cell wall is the presence of a peptidoglycan layer which is a complex molecule of repeating units of two sugar derivatives (*N-acetylmuramic acid* (NAM) and *N-acetylglucosamine* (NAG) which are linked by peptide cross links and some amino acids.<sup>35</sup>

3: The cell membrane consists of a phospholipid bilayer with protein and glycoprotein dispersed throughout (layers in between). This membrane plays a significant role in cell functions such as the energy conservation in the cell, the cell biosynthesis, and as a permeability barrier. The proteins in both structural and enzymatic forms are responsible for most of the membrane functions and the synthesis of the membrane lipids as well.<sup>36</sup>

On the basis of the cell wall structure, bacteria can be divided into Gram-positive and Gram-negative bacteria. For this classification a Gram staining procedure is carried out to test the ability of the bacteria cell wall to retain a crystal violet dye. Bacteria that retain the crystal violet appear purple and are called Gram-positive, while bacteria that are not stained by crystal violet are referred to as Gram-negative.<sup>35</sup> Gram-positive bacteria have a cell wall of two layers; a thick peptidoglycan (90%) sheet and an internal membrane and Gram-negative bacteria have a multilayer-wall structure that has an internal membrane, a thin peptidoglycan (10%) sheet, periplasm, and outer membrane which is a lipid bilayer composed of phospholipids and lipopolysaccharide (LPS). This difference is shown in Figure 2.19. LPS contains two proteins (core polysaccharide and O-polysaccharide) and a lipid A tail, the core polysaccharide protein contain ketodeoxyoctonate (KDO), different carbon sugars, and phosphates.

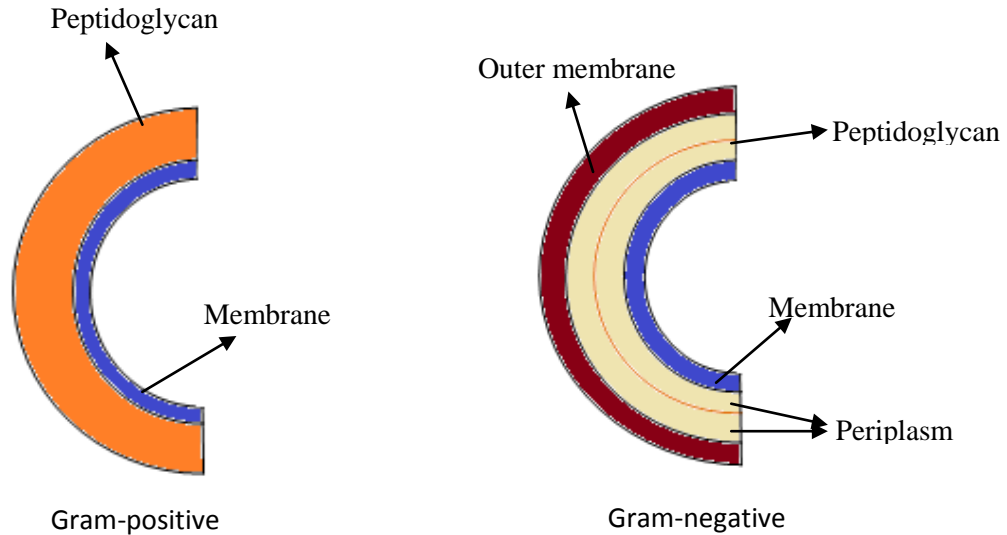


**Figure 2.19:** Composition of the cell wall of Gram-positive and Gram-negative bacteria

#### 2.4.1.2 Biochemical Constituents of the Cell

Water is the main constituent of the living bacteria cell (about 70% of the total weight of a live cell); the remaining 30% represent the dry compositions of the cell which includes macromolecules and small amount of monomers and inorganic ions.<sup>35</sup> Macromolecules which represent 96% of the cell dry weight are polymers of small monomers. Total monomers including amino acids, sugars, nucleotides, fatty acids and their precursors just amount to about 3% of the dry cell weight, while inorganic ions that are required for many essential functions of the cell represent only the remaining 1%. Table 2.2 lists the types of macromolecules, their subunits, location in the cell, and their percentage composition of dry cell weight.<sup>35</sup>

Table 2.2: The macromolecules in the bacterial cell and their subunits, location, and average percentage composition of the dry cell weight.<sup>35</sup>

Macromolecule	Primary subunit (monomer)	Location in the cell	Percentage of dry weight
Proteins	amino acids	Cell wall, cell membrane, pili, flagella, ribosomes, as enzymes in the cytoplasm.	55%
Lipids	fatty acids	Membranes, storage depots	9%
Polysaccharides	sugars (carbohydrates molecules)	Cell wall, capsule, inclusions (energy and carbon storage)	5%
Lipopolysaccharides	Sugars and fatty acids	Membranes	3.4%
RNA	Nucleotides	Ribosomes	20.5%
DNA	Nucleotides	nucleoid, plasmid	3.1%

## 2.5 Raman Spectra Obtained From Macromolecules

Bacterial Raman spectra composed of a complex pattern of many bands represent a superposition of molecular vibrations contributed from different molecules inside the cell. Therefore, the assignment of each band to a specific molecule is not trivial and can be attributed to different molecular structure of the cell macromolecule. An overview of the spectral patterns obtained from the individual macromolecules monomers will be helpful in the analysis of Raman spectra of the whole complex structure of the cell by providing a reference database of the different band assignments. The main macromolecule structures and their Raman spectra are discussed below,

### 2.5.1 Proteins

Proteins are polymers of amino acids that are linked by peptide bounds. There are 20 amino acids that differ considerably by their side chain which could be simple and small as in glycine and L-alanine, extended as in L-valine, L-serine and L-glutamate, or contain ring structures as in the aromatic amino acids L-phenylalanine, L-tyrosine and L-tryptophan. Raman spectra of those amino acids are shown in Figure 2.20 and 2.21.<sup>37</sup>

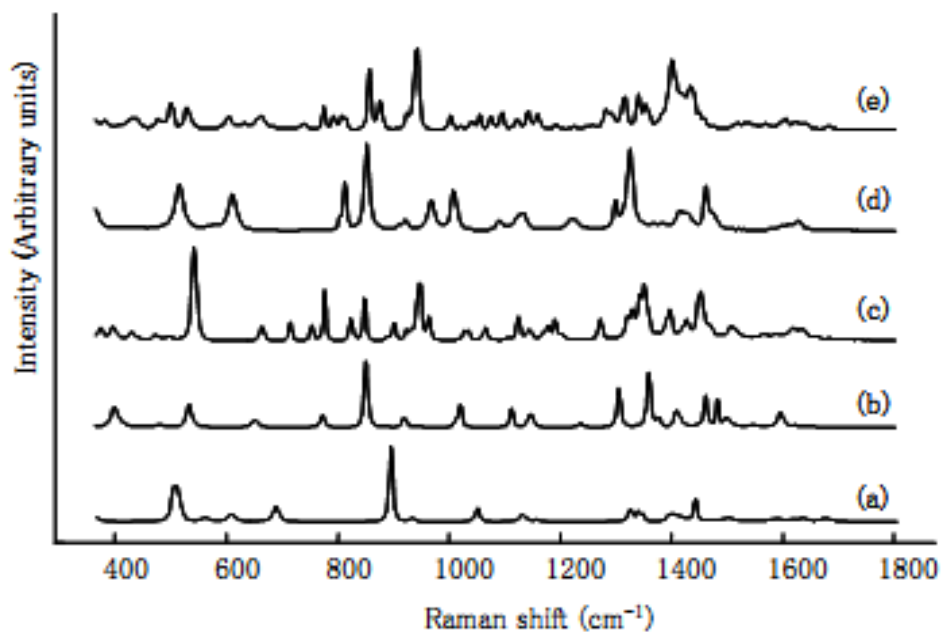


**Figure 2.20:** Raman spectra of amino acids with non-cyclic side chain: (a) glycine, (b) L-alanine, (c) L-valine, (d) L-serine, (e) L-glutamate.

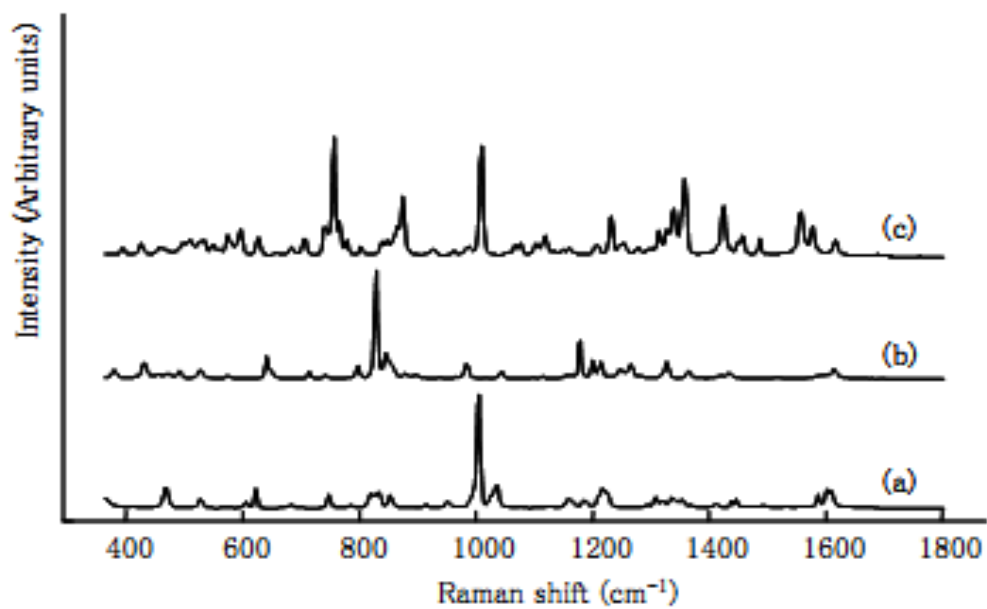


**Figure 2.21:** Raman spectra of amino acids with a cyclic side chain: (a) L-phenylalanine, (b) L-tyrosine, (c) L-tryptophan.

The strong bands in those amino acids and their assignments are given in table 2.3.

Table 2.3: The band assignments for the main bands that appear in the amino acids Raman spectra.<sup>38</sup>

Amino acid	Band position (cm <sup>-1</sup> )	Assignment
Glycine	894	CNC symmetric stretch
L-alanine	851	CNC symmetric stretch
L-valine	524 1351	CC <sub>3</sub> deformation CH deformation
L-serine	813, 853	C-C-O in-phase stretch or C-N stretch
L-glutamate	1401	CO <sub>2</sub> symmetric stretch
L-phenylalanine	1004	ring breathing
L-tyrosine	828	ring breathing
L-tryptophan	1009	ring breathing

## 2.5.2 Lipids

Lipids represent the main structure of the cell membrane, lipopolysaccharide and the storage depot of carbon inside the cell. Simple lipids such as triglycerides are made of three fatty acids and glycerol. Complex lipids such as phospholipids consist of triglycerides and other elements like nitrogen or phosphorous. The variation of lipids in the bacterial cell membrane has been used for bacteria identification and classification.<sup>39</sup>

Raman spectra of different linear (unbranched) saturated fatty acids are shown in Figure 2.22, the position of the main bands are at  $1296\text{ cm}^{-1}$  assigned for  $\text{CH}_2$  twisting vibration,  $1050\text{--}1150\text{ cm}^{-1}$  attributed to C-C stretching vibration, and  $1400\text{--}1500\text{ cm}^{-1}$  due to  $\text{CH}_2$  or  $\text{CH}_3$  deformations.<sup>37</sup> The unsaturated fatty acids Raman spectra showed an extra strong band located at  $1655\text{ cm}^{-1}$  attributed to C=C stretching vibrations.<sup>37</sup>

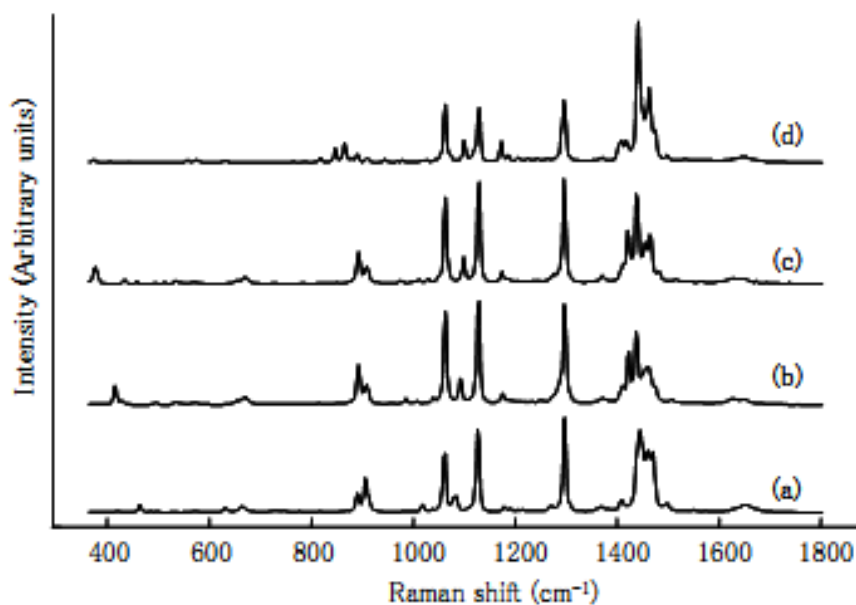


**Figure 2.22:** Raman spectra of saturated fatty acids: (a) lauric acid, (b) myristic acid, (c) palmitic acid, (d) stearic acid.

### 2.5.3 Polysaccharides

Polysaccharides (as mentioned before) represent important components in the cell capsule structure and LPS which is characteristic of Gram-negative bacteria so they have been used for bacterial identification.<sup>40</sup> The structure of polysaccharides which are made of different sugar monomers has been proven to be unique for closely related strains of some kinds of bacteria.<sup>41</sup> Figure 2.23 shows Raman spectra of some saccharides.

The bands located between 400-700  $\text{cm}^{-1}$  are assigned for endocyclic and exocyclic deformations.<sup>42</sup> Those located between 800-950  $\text{cm}^{-1}$  are assigned for COH, CCH, and OCH deformation vibrations. Those located in the region 1000-1200  $\text{cm}^{-1}$  are assigned for C-O stretching vibrations, while  $\text{CH}_2$  and  $\text{CH}_2\text{OH}$  deformation vibrations are represented by the bands in the region 1250-1500  $\text{cm}^{-1}$ .<sup>43</sup>

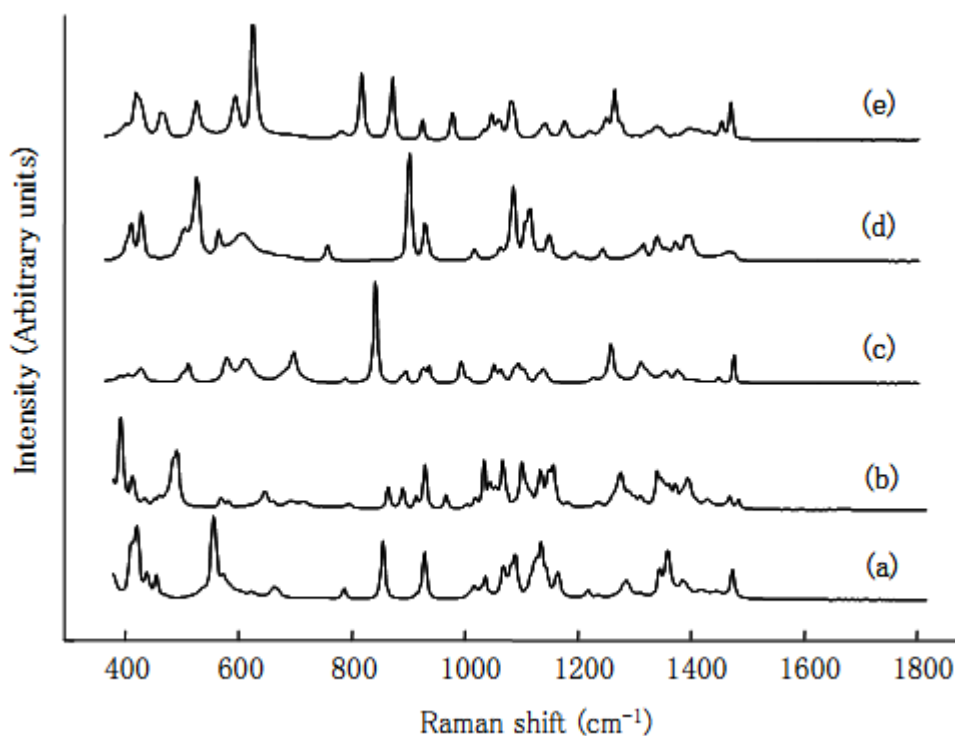


**Figure 2.23:** Raman spectra of some saccharides: (a)  $\beta$ -D-glucose, (b) lactose, (c) D(-)-arabinose, (d) D(+)-xylose, (e) D(-)-fructose.

### 2.5.4 Nucleic Acids (DNA and RNA)

Nucleic acids are polymers of nucleotides, where the nucleotides are composed of a base attached to a sugar by a glycosidic linkage and phosphate. The special sequence of the nucleotides in the nucleic acids represents the genetic information of the cell. Even though its abundance in the bacterial cell is small, DNA is essential for cell reproduction and function. RNA converts the genetic information carried by the DNA into amino acid sequences in proteins.<sup>35</sup> Raman spectra for the five different bases is shown in Figure 2.24.<sup>37</sup>

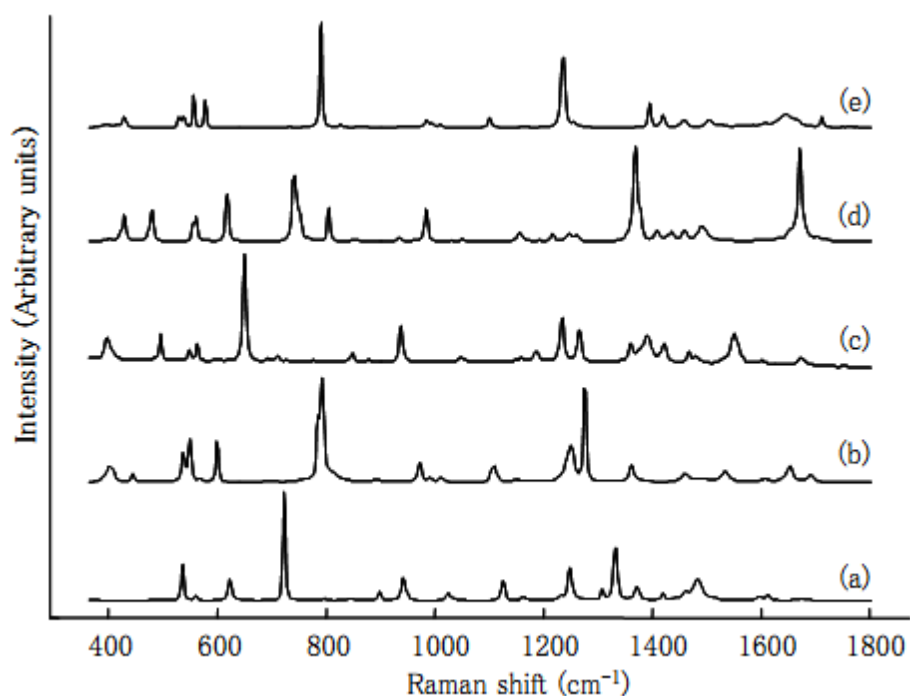


**Figure 2.24:** Raman spectra of Nucleic acids bases: (a) adenine, (b) cytosine, (c) guanine, (d) thymine, (e) uracil.

The observed strong band located between 600-800  $\text{cm}^{-1}$  is due to ring breathing vibrations and for thymine there is a strong band located at 1671  $\text{cm}^{-1}$  assigned to C=O stretching vibrations.<sup>37</sup>

## 2.6 Bacterial Classification

As mentioned earlier, bacteria are classified based on their cell wall structure into Gram-positive and Gram-negative. The Gram-positive bacteria are divided into aerobic cocci and bacilli based on the cell shape while Gram-negative have four groups: cocci, enteric, non-fomenters, and Pleomorphic bacteria. Figure 2.25 reveals the flow chart of this classification.

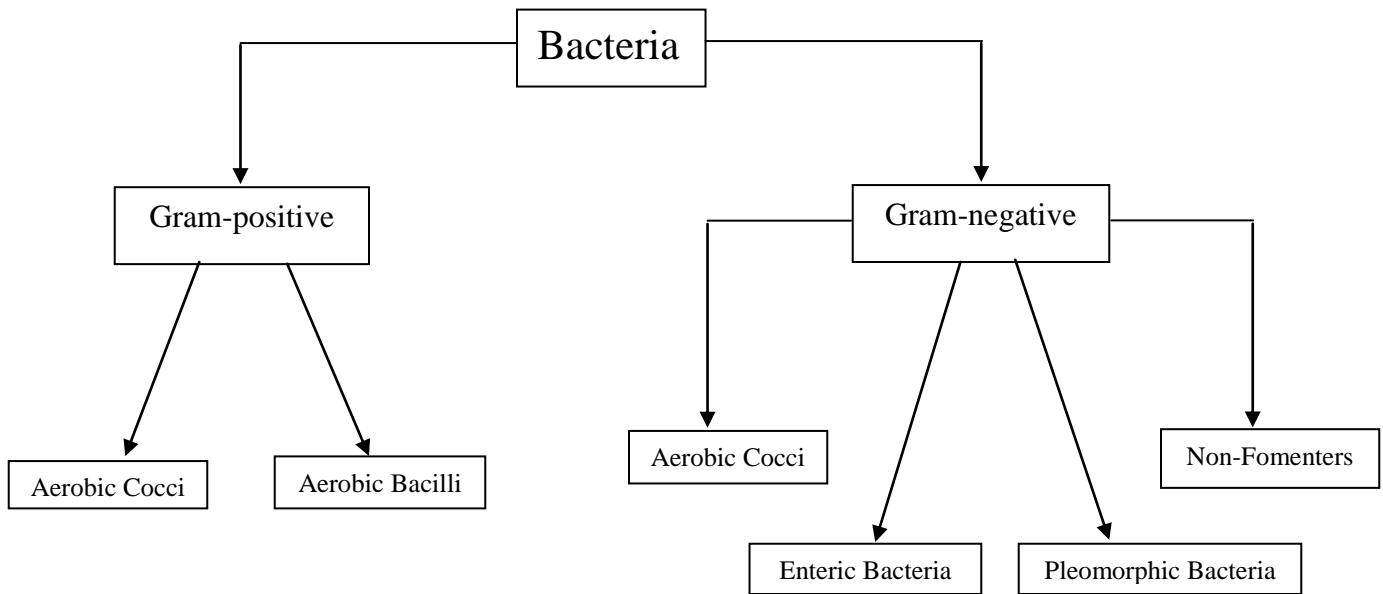


**Figure 2.25:** Bacteria classification flow chart.

Here is a brief overview of the bacterial groups with the bacterial species and strains that were studied in this work indicated in bold.

### 2.6.1 Gram-Positive Aerobic Cocci

This group has a thick cell wall, aerobic action on glucose, and a spherical shape. It includes many clinically relevant bacteria such as *micrococcus*, ***staphylococcus***, and ***streptococcus***. ***Staphylococcus*** genus is a toxin-producing bacterium which can be divided into two main species, ***S. aureus*** and non-aureus species (such as *S. epidermis*.) The most dangerous

pathogen of this group is *S. aureus* which causes food poisoning, tissue infections, and toxic shock syndrome which may lead to death. Many *S. aureus* strains are resistant to different kinds of antibiotic, so differentiation between those strains is of great importance and that will be discussed in chapter four.

On the other hand *streptococcus* bacteria include four different groups: *S. pyogenes* which are responsible for throat infections that can be treated by penicillin, *S. agalactiae* which cause the urogenital infections, and type D *streptococcus* that are divided into two subgroups of enterococci such as *E. faecalis* (urinary tract infection pathogen) and non-enterococci. The fourth group is called **viridans group** which includes *S. mitis* and *S. mutans*. Those bacteria are found in the mouth and are responsible for tooth decay. A comprehensive study of this group of bacteria was carried out in Chapter 5. Finally *Streptococcus pneumonia* is a *streptococcus* species that does not belong to any of the discussed *streptococcus* groups. This bacterium causes otitis media and pneumonia and its impact will be discussed also in chapter 5.

### 2.6.2 Gram-Positive Aerobic Bacilli

This group contains rod shaped bacteria with a thick cell wall and aerobic action on glucose. It is classified into five groups: bacillis are endospores-forming bacteria with many harmless species that live in water, air, soil and the intestines of human. The only pathogenic species of this group are *B. cereus* which causes food poisoning and the anthrax pathogen *B. anthracis*. The second group is *listeria* which include pathogenic species as *L. monocytogenes*, the cause of many food poisoning epidemics and *L. ivanovii*. A person who is infected with listeria suffers from severe nausea, vomiting, and diarrhea. *Lactobacillus* group include non-pathogenic bacteria that have the ability to derive glucose into lactic acids and so it is important for dairy products. The fourth genus is called *Erysipelothrix* with one pathogenic species *E.*

*rhusiopathiae* (causes skin infection). Finally, corynebacteria include many harmless genera and species and two harmful genera; *Actinomyces* and *Corynebacterium* that have some toxin-producing species.

### **2.6.3 Gram-Negative Enterobacteriaceae**

This group includes the most clinically relevant bacteria since they cause many diseases such as intestinal infections with almost the same symptoms. The laboratory identification of different species and strains of this family is very crucial. This family consists of 12 genera, *escherichia*, *edwardsiella*, *citrobacter*, *enterobacter*, *proteus*, *providencia*, *shigella*, *salmonella*, *klebsiella*, *serratia*, *morganella*, and *yersinia*. A study of the first genera (*Escherichia coli*) will be discussed in chapter four.

## CHAPTER 2 REFERENCES

- 
- <sup>1</sup> E.B. Hanlon, R. Manoharan, T.-W. Koo, K.E. Shafer, J.T. Motz, M. Fitzmaurice, J.R. Kramer, I. Itzkan, R.R. Dasari and M.S. Feld, "Prospects for *in vivo* Raman spectroscopy," *Physics in Medicine and Biology* **45**:R1-R59 (2000).
- <sup>2</sup> P.D. Taylor, O. Vinn, A. Kudryavtsev, and J.W. Schopf, "Raman spectroscopic study of the mineral composition of cirratulid tubes (Annelida, Polychaeta)," *Journal of Structural Biology* **171**:402-405 (2010).
- <sup>3</sup> B. Chen, "Raman spectroscopy studies of carbon nanotube-polymer composites," in *Dekker Encyclopedia of Nanoscience and Nanotechnology*, (2004).
- <sup>4</sup> L.P. Choo-Smith, H.G.M. Edwards, H.P. Endtz, J.M. Kros, F. Heule, H. Barr, J.S. Robinson, Jr., H.A. Bruining, and G.J. Puppels, "Medical applications of Raman spectroscopy: from proof of principal to clinical implementation," *Biopolymers* **67**:1-9 (2002).
- <sup>5</sup> K. Birmingham and G. Kenyon, "Bioterrorism threat becomes reality," *Nature* **71**:1167 (2001).
- <sup>6</sup> The world health report. Annex table 2 (2004).
- <sup>7</sup> J.R. Ferraro, K. Nakamoto, and C.W. Brown, *Introductory Raman Spectroscopy*, Second edition, Elsevier (2003).
- <sup>8</sup> A. Smekal, "Zur quantentheorie der dispersion," *Naturwiss* **11**:873-875 (1923).
- <sup>9</sup> C.V. Raman and K.S. Krishnan, "A new type of secondary radiation," *Nature* **121**:501-502 (1928).
- <sup>10</sup> M.J. Pelletier, *Introduction to Applied Raman Spectroscopy*, Blackwell Science Ltd, Oxford, 1-52 (1999).
- <sup>11</sup> R.Y. Tsien and A. Waggoner, "Fluorophores for confocal microscopy," J.B. Pawley, *Handbook of biological confocal microscopy*, New York, Plenum Press 267-274 (1995).
- <sup>12</sup> A. Sengupta, N. Brar, and E.J. Davis, "Bioaerosol detection and characterization by surface-enhanced Raman spectroscopy," *Journal of Colloid and Interface Science* **309**:36-43 (2007).
- <sup>13</sup> R.A. Dalterio, W.H. Nelson, D. Britt, J. Sperry and F.J. Purcell, "Resonance Raman microprobe study of *chromobacteria* in water," *Applied Spectroscopy* **40**:271-272 (1986).
- <sup>14</sup> W.H. Nelson, R. Manoharan and J.F. Sperry, "UV resonance Raman studies of bacteria," *Applied Spectroscopy Reviews* **27**:67-124 (1992).
- <sup>15</sup> W. Nelson and J.F. Sperry, "UV resonance Raman spectroscopic detection and identification of bacteria and other microorganisms," in *Modern Techniques for Rapid Microbiological Analysis*. W.H. Nelson, Editor. VCH Publishers, New York 127-132 (1991).

- 
- <sup>16</sup> R.M. Jarvis and R. Goodacre, "Ultra-violet resonance Raman spectroscopy for the rapid discrimination of urinary tract infection bacteria," *FEMS Microbiology Letters* **232**:127-132 (2004).
- <sup>17</sup> N. Dudovich, D. Oron and Y. Silberg, "Single-pulse coherent anti-Stokes Raman spectroscopy in the fingerprint spectral region," *Journal of Chemical Physics* **118**:9208-9214 (2003).
- <sup>18</sup> A. Dogariu, A. Goltsov, D. Pestov, A.V. Sokolov and M.O. Scully, "Real-time detection of bacterial spores using coherent anti-Stokes Raman spectroscopy," *Journal of Applied Physics* **103**:036103 1-3 (2008)
- <sup>19</sup> K. Kneipp, A.S Haka, H. Kneipp, K. Badizadegan, N. Yoshizawa, C. Boone, K.E. Shafer-Peltier, J.T. Motz, R.R. Dasari, and M.S. Feld, "Surface-enhanced Raman spectroscopy in single living cells using gold nanoparticles," *Applied Spectroscopy* **56**:150-154 (2002).
- <sup>20</sup> A. Campion and P. Kambhampati, "Surface-enhanced Raman scattering," *Chemical Society Reviews* **27**:241-250 (1998).
- <sup>21</sup> R. Petry, M. Scmitt, and J. Popp, "Raman spectroscopy - a prospective tool in the life sciences," *Chemical and Physical Chemistry* **4**:14-30 (2003).
- <sup>22</sup> M. Culha, A. Adigüzel, M.M. Yazici, M. Kahraman, F. Sahin, M. Güllüce, "Characterization of thermophilic bacteria using surface-enhanced Raman scattering," *Applied Spectroscopy* **62**:1226-32 (2008).
- <sup>23</sup> H.-W. Cheng, S.-Y. Huan, H.-L. Wu, G.-L. Shen, and R.-Q. Yu, "Surface-enhanced Raman spectroscopic detection of a bacteria biomarker using gold nanoparticle immobilized substrates," *Analytical Chemistry* **81**:9902-9912 (2009).
- <sup>24</sup> R.M. Jarvis and R. Goodacre, "Discrimination of bacteria using surface enhanced Raman spectroscopy," *Analytical Chemistry* **76**:40-47 (2004).
- <sup>25</sup> M. Kahraman, M.M. Yazici, K. Sahin, O.F. Bayrak and M. Culha, "Reproducible surface-enhanced Raman scattering spectra of bacteria on aggregated silver nanoparticles," *Applied Spectroscopy* **61**:479-485 (2007).
- <sup>26</sup> R.K. Dutta, P.K. Sharma and A.C. Pandey. "Surface enhanced Raman spectra of Esherichia coli cells using ZnO nanoparticles," *Digest Journal of Nanomaterials and Biostructures* **4**:83-87 (2009).
- <sup>27</sup> L.D. Landau and E.M. Lifshitz, *Mechanics*, 3rd. ed., Pergamon Press (1976).
- <sup>28</sup> D.C. Harris, and M.D. Bertolucci, *Symmetry and spectroscopy: an introduction to vibrational and electronic spectroscopy*, Oxford University Press (1978).
- <sup>29</sup> J.M. Chalmers and P.R. Griffiths, *Handbook of Vibrational Spectroscopy*, (2002).

- 
- <sup>30</sup> O. Svelto, *Principles of lasers*: translated from Italian and edited by D.C. Hanna. 4<sup>th</sup> edition. (1998).
- <sup>31</sup> J.B. Pawley, *Handbook of Biological Confocal Microscopy*, Third edition (2006).
- <sup>32</sup> H.P. Berlien and G.J. Muller, *Applied Laser Medicine*, Medical (2003).
- <sup>33</sup> D.M. Karl, D.F. Bird, K. Bjorkman, T. Houlihan, R. Shackelford and L. Tupas, "Microorganisms in the accreted ice of Lake Vostok, Antarctica," *Science* **286**:2144-2147 (1999).
- <sup>34</sup> R. Mogul, J.J. Getz Kelly, M.L. Cable and A.F. Hebard. "Synthesis and magnetic characterization of microstructures prepared from microbial templates of differing morphology", *Materials Letters* **60**: 19-22 (2006).
- <sup>35</sup> M. Madigan, J. Martinko, and J. Parker, *Brock Biology of Microorganisms*, 9th Edition, Prentice Hall College Div (1996).
- <sup>36</sup> K. Todar, *Todar's online test books of bacteriology*, University of Wisconsin, Department of Bacteriology, Madison, Wisconsin (2006).
- <sup>37</sup> J. De Gelder, "Raman spectroscopy as a tool for studying bacterial cell compounds," Ph-D dissertation in sciences, chemistry Gent university (2007-2008).
- <sup>38</sup> D. Lin-Vien, N.B. Colthup and W.G. Fateley, *The handbook of infrared and Raman characteristic frequencies of organic molecules*, Academic Press, San Diego (1991).
- <sup>39</sup> B. Bendinger, R.M. Kroppenstedt, S. Klatt and K. Altendorf. "Chemotaxonomic differentiation of coryneform bacteria isolated from biofilters," *International Journal of Systematic Bacteriology* **42**:474-486 (1992).
- <sup>40</sup> H. Brade, L. Brade and E.T. Rietschel, "Structure-activity relationships of bacterial lipopolysaccharides (endotoxins). Current and future aspects." *Zentralbl Bakteriologie Mikrobiologie Hygiene* **268**:151-179 (1988).
- <sup>41</sup> N. Bergstrom, P.E. Jansson, M. Kilian, and U.B. Skov Sorensen, "Structures of two cell wall-associated polysaccharides of a *streptococcus mitis* biovar 1 strain. A unique teichoic acid-like polysaccharide and the group O antigen which is a C-polysaccharide in common with pneumococci," *European Journal of Biochemistry* **267**:7147-7157 (2000).
- <sup>42</sup> M.F. Mrozek and M.J. Weaver, "Detection and identification of aqueous saccharides by using surface-enhanced Raman spectroscopy," *Analytical Chemistry* **74**:4069-4075 (2002).
- <sup>43</sup> Y.M. Weng, R.H. Weng, C.Y. Tzeng, W.Chen, "Structural analysis of triacylglycerols and edible oils by near-infrared Fourier transform Raman spectroscopy," *Applied Spectroscopy* **57**:413-418 (2003).

## Chapter 3

### Data Collection and Statistical Analysis Methods

In this chapter I will discuss the procedures of data collection. This discussion includes: sample preparation, the calibration process of the Raman instrument, acquisition of the Raman spectral data, data processing, and data analysis using the appropriate statistical methods.

#### 3.1 Sample Preparation for Raman Spectroscopy

Different bacterial strains used in this study were cultured as shown in Figure 3.1A using different methodologies with specific conditions that will be discussed thoroughly later. In all cases, dense pellets of bacteria (as shown in Figure 3.1B) were obtained from the bacterial culture for subsequent Raman spectroscopy. 10  $\mu$ L of each of the suspensions was transferred to a low-fluorescence quartz microscope slide (shown in Figure 3.1C) using a micro-pipette and allowed to air-dry at room temperature for about two hours. After each use, the slides were cleaned with deionized water, acetone, and methanol successively to remove any organic contaminants or residue from the tested bacteria.

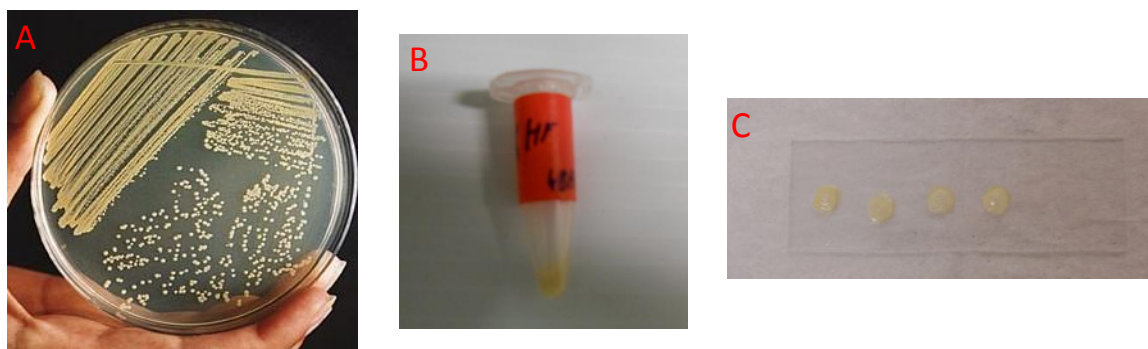


**Figure 3.1:** (A) Bacteria cultured on a plate, (B) a tube containing a dense pellet of bacteria, (C) bacterial suspensions smeared on a quartz slide.

Quartz was chosen as a substrate material since the Raman spectrum obtained from a blank quartz microscope slide showed no significant features in the range under investigation (600-2000  $\text{cm}^{-1}$ ) as compared to the bacterial samples as shown in Figure 3.2.

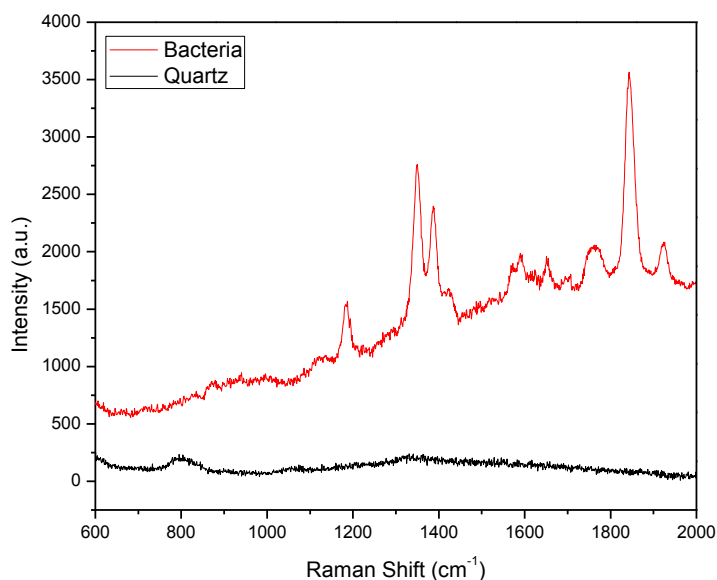


**Figure 3.2:** A comparison between Raman spectra obtained from quartz and bacteria.

### 3.2 Instrument Calibration and Spectrum Acquisition

In order to ensure the repeatability of the data, an instrument calibration was done before each use. The unique Raman peak of single crystal silicon located at  $520 \text{ cm}^{-1}$  was used as a calibration standard. The detailed procedure that was used to operate the system and take the measurement is given below:

1. Fill the liquid nitrogen Dewar and wait about 2 hours until the CCD temperature drops to about  $-130 \text{ C}^{\circ}$ .
2. Turn on laser and let laser warm up.

3. When laser power is stable at 60 mW, let laser into microscope.
4. Measure power after the 100X objective, it should be about 6 mW. Otherwise a realignment of the optics should be done.
5. Open the software program (Labspec) that is available in the computer (pictured in Figure 3.3) and turn on the camera.
6. Focus the laser on the target using the microscope adjustment knobs to get the clearest image on the screen.
7. Acquire a Si spectrum, setting the experimental parameters as: scan time = 10 sec, numbers of scans=3, with spectral range spanning 450-650  $\text{cm}^{-1}$ .
8. If the Si peak position is shifted from 520  $\text{cm}^{-1}$ , a calibration is done by changing the zero of the instrument calibration that can be found under the setup category (shown in Figure 3.4) and repeat the scan to get the exact location of the peak.
9. At this point we can take measurements for the bacterial samples; to avoid any spikes originating from room light, the measurements should be taken in a dark room with all lights off. Different spots of the sample were scanned to obtain many spectra that represent the molecular composition of the sample, an example of bacteria spectra are shown in Figure 3.5. Each spectrum was obtained from the average of three exposures with an exposure time of 10 s and the spectra were collected in the information-rich region between 600 and 2000  $\text{cm}^{-1}$  with 2070 data points. 1200 groves/mm grating and 100X microscope objective were chosen for all the experimental work. All the experimental parameters were controlled by the software

as appeared in Figure 3.3. The spectral data should be saved in order to be processed and analyzed as will be discussed in the next section.

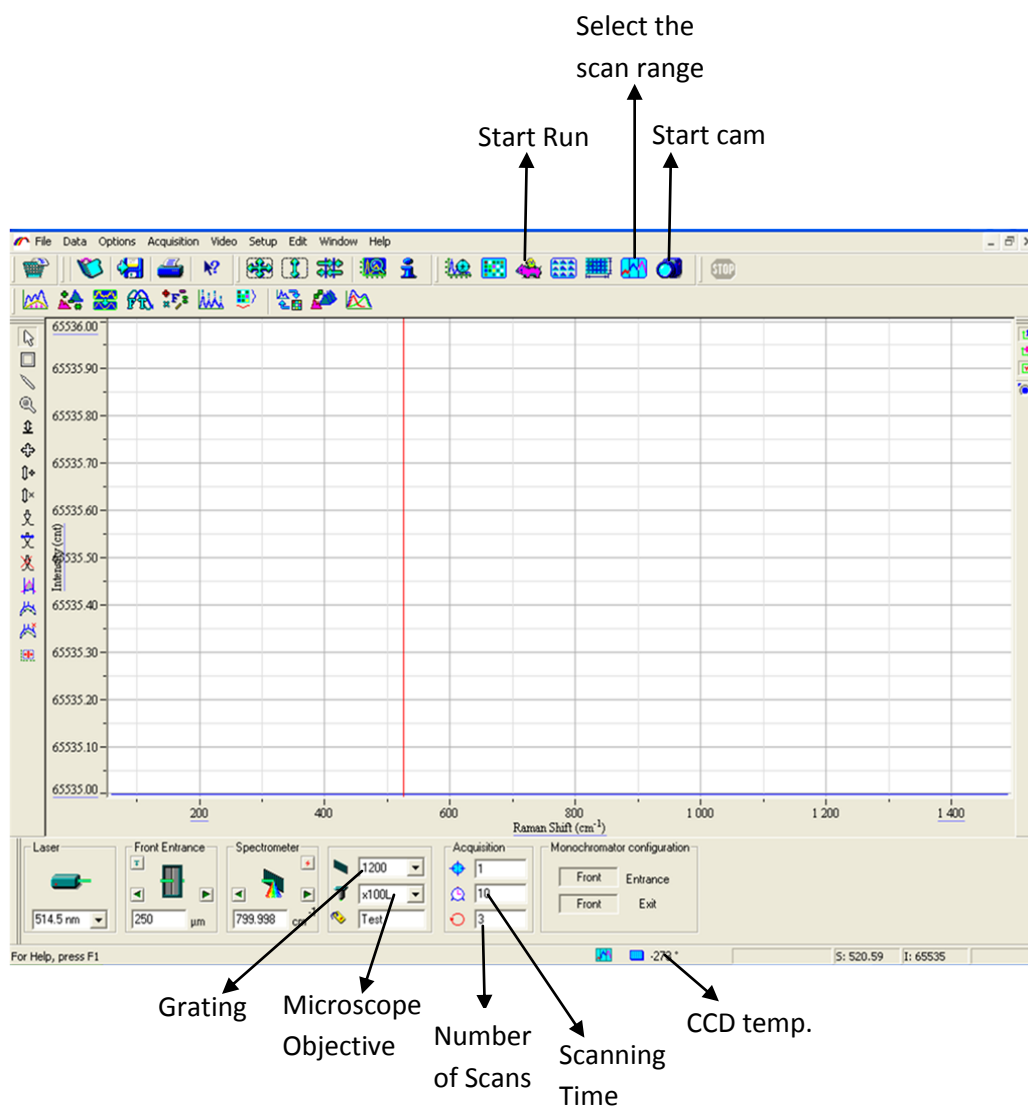


**Figure 3.3:** Labspec software home page.

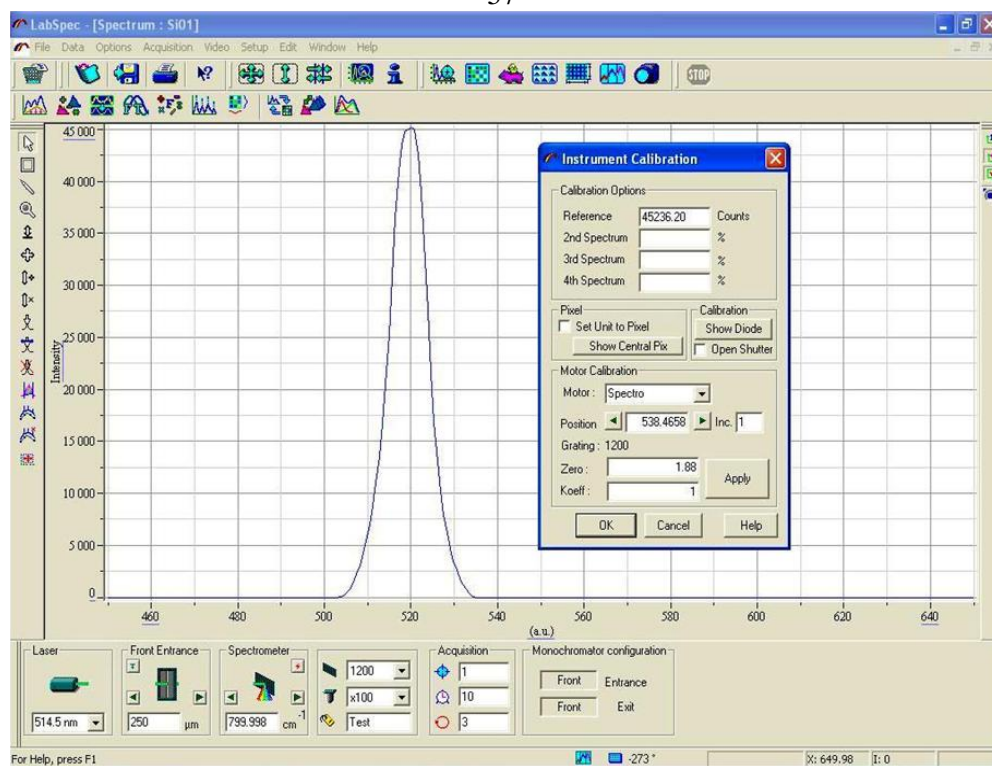


**Figure 3.4:** Calibration process of the Si Peak.

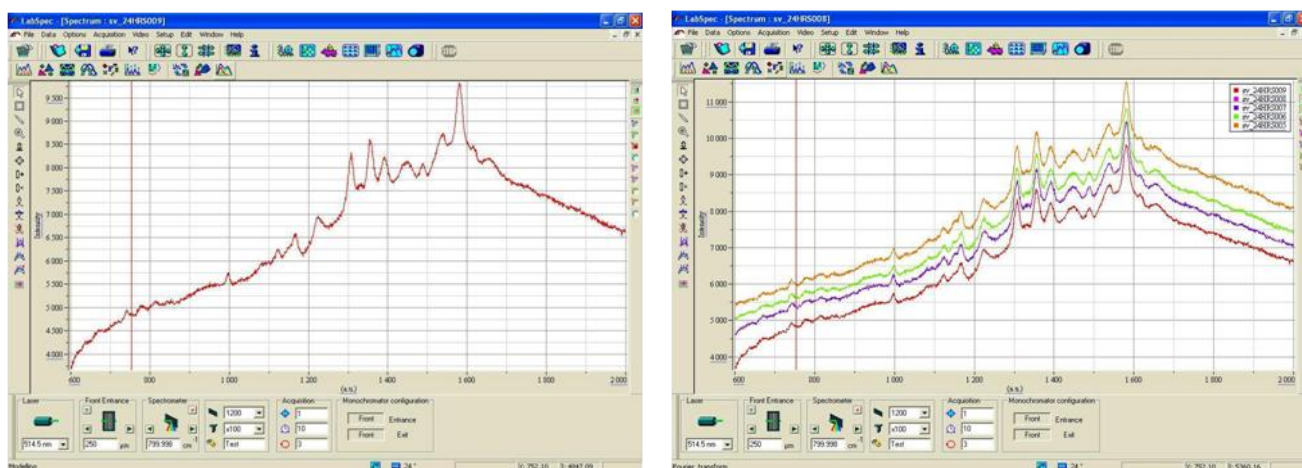


**Figure 3.5:** (left) A spectrum of bacteria in the spectral range 600-2000  $\text{cm}^{-1}$ . (right) Multiple spectra obtained from different spots of the same sample.

### 3.3 Data Preprocessing for Statistical Analysis

Data processing of the spectra included baseline correction and normalization of the Raman spectra. As discussed earlier, the spectra of biological samples suffer from a huge background (visible in Figure 3.5) due to fluorescence. Many hardware techniques were developed to solve this problem, but recently the development of software routines have made mathematically-based procedures to correct the background much easier and cheaper. Different numerical algorithms were used for this purpose.<sup>1</sup> One of the most significant and accurate algorithms uses a polynomial fit to approximate the profile of the background and subtracts it without any loss of the spectral signatures.<sup>2</sup>

A robust automated method using a custom Matlab program utilizing an adaptive minmax method was chosen to remove the background from each spectrum and normalize the spectral data by setting the max intensity to one.<sup>3</sup> The background subtraction procedure in this method is based on the fluorescence-to-signal ratio (F/S) where a multiple polynomials fit with different orders have been used to fit across all F/S ratios instead of a single polynomial fit as adapted by other comparable methods. F/S ratio is calculated by dividing the maximum fluorescence by the maximum Raman signal. Cao *et al.* named this method “the adaptive minmax” method since the subtraction process is carried out in two algorithmic steps. The adaptive part relates to the first step where two different polynomial fits (constrained and unconstrained) were performed with two different orders that were adapted based on the F/S ratio with the lowest RMS value. The minmax related to the second step where ‘min’ stand for taking the minimum point between the spectrum and the polynomial fit to prevent overfitting the data and ‘max’ stand for taking the maximum value among all the fitting to avoid underfitting the data.

A Matlab program was used for the data processing where the adaptive fit parameters (such as the fitting polynomial orders) were determined. Then a fourth-order polynomial fit was performed to estimate the spectrum F/S ratio which determined the order of the four polynomials that were used to get the best final fit for subtraction. After the subtraction process the program also normalized the processed spectrum from 0-1 by setting the maximum intensity to 1. Figure 3.6 shows the subtraction procedure.

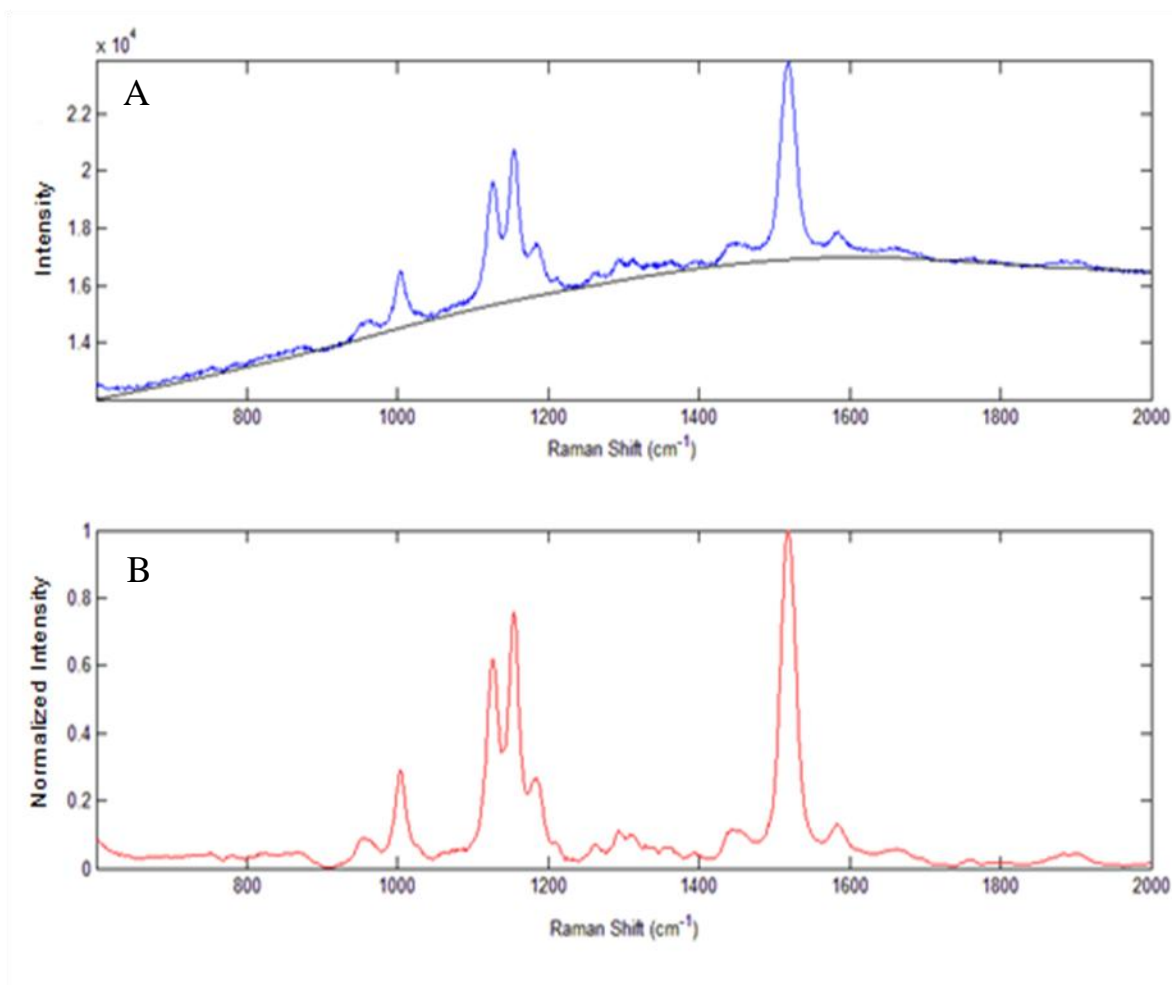


**Figure 3.6:** (A) Raw Raman spectrum of bacteria in blue and the best polynomial fit of the background in black. (B) The same Raman spectrum after processing (background subtraction and normalization).

### 3.4 Multivariate Statistical Methods

Due to the complexity of the bacterial Raman spectrum, which consists of many overlapping features, and the subtle differences between the spectra obtained from different samples, extracting quantitative and qualitative information from the spectra is not straight forward. Advanced statistical techniques are required to conveniently handle the huge amount of data and obtain the relevant results. Many methods have been found to analyze a large number of multivariate data in which the data contains a number of objects (Raman spectra in our case) with a large number of variables (the Raman intensities of observed peaks) and analyze the simultaneous relationships among the variables.<sup>4</sup> Principal component analysis (PCA)<sup>5,6,7</sup> and discriminant function analysis (DFA)<sup>8,9,10</sup> are powerful multivariate analysis strategies that can be applied successfully for this spectral data analysis. PCA followed by DFA was used in this work to minimize the dimensions of the data and for discrimination and classification purposes.

#### 3.4.1 Principal Component Analysis (PCA)

PCA is a statistical technique that is used to reduce the number of dimensions of data with a minimum loss of information. The goal of PCA is to determine the data patterns and underlying factors that cause the similarities and differences of the original data without any prior knowledge. These factors are called principal components (PCs).<sup>11</sup>

Mathematically, the original data matrix with  $i$  objects (spectra) and  $j$  variables (intensity) is decomposed into two matrices, the scores matrix related to the object (and having the same dimensions of the data matrix ( $i,j$ )) and loadings matrix related to the variables with ( $j,j$ ) rank. The PCs are the eigenvectors of the score matrix and the eigenvalues represent the data variance captured by the PCs. The first PC is associated with the eigenvector of the highest eigenvalue so it has the largest variance and the following PCs follow the same order. In general, the number

of PCs is equal to the number of variables, but we can ignore those of lesser significance in order to get a data set which maintains as much of the original variation as possible with fewer dimensions ( $n$  variables). In other words, PCA not only reduces the number of variables from  $j$  to  $n$  but also makes the important features for classification easily predictable. The grouping between the spectra (objects) can be observed by drawing a 2-dimensional plot of the first and second principal components scores for each spectrum and the relation between the original variables can be shown by constructing a plot of the loadings where the variables are plotted versus Raman shift. In this case observed bands in this plot will represent the variables (Raman features) that are responsible for the discrimination.<sup>12</sup> An example of the loadings plot is given in Figure 3.7. PCA is often utilized as a first step for other multivariate analyses which will then use component scores instead of the original data. This speeds up the subsequent analysis and makes it easier.<sup>5</sup>

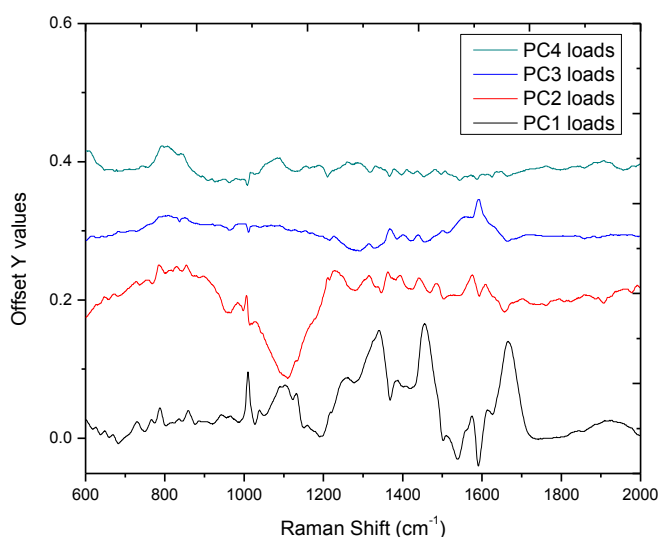


**Figure 3.7:** Principal component loadings of the PCA performed on the Raman spectra acquired from three different bacterial samples.

### 3.4.2 Discriminant Function Analysis (DFA)

DFA is a statistical tool which is used to classify the multivariate data into groups. In our case the groups consist of spectra from identical types of bacteria and spectra from other bacteria strains or species. DFA uses a set of independent variables from each spectrum (principal component scores) to predict the differences between groups with minimum misclassification error.<sup>13</sup> This is done by minimizing the within-group-variance and maximizing the between-group-variance. The first step in DFA is to obtain linear combinations of the independent variables that best discriminate the groups, which are called canonical discriminant function scores. If the number of groups (types of bacteria) is  $i$ , the number of objects (different Raman spectra obtained from the same bacterium) is  $j$  and the number of variables (principal component scores) is  $k$ , then the discriminant function scores for group  $i$  and object  $j$  ( $f_{ij}$ ) is given by equation 3.1,<sup>14</sup>

$$f_{ij} = w_0 + w_1x_{1ij} + w_2x_{2ij} + \dots + w_kx_{kij} \quad 3.1$$

where  $x_{1ij}, x_{2ij}, \dots, x_{kij}$  are the independent variables for object  $j$  in the known groups  $i$ ,  $w_0, \dots, w_k$  are the weight coefficients of the function (eigenvectors) which can be achieved by maximizing the difference between groups. The total numbers of the discriminant functions should be less than the total number of groups by one ( $i-1$ ).

A test of “hypothesis for significance in the discriminant function” is performed by checking the differences between group means. The null hypothesis means that all data are sampled from the same normal distribution with a single mean and variance, while significantly different groups will exhibit means that differs by an amount greater than the variance. If a sample of data passes the significance test, the discriminant function scores will be calculated by

a vector product of the independent variables and the coefficients of the discriminant function. The first discriminant function score represents the most significant differences between groups and a spectrum's score can be used as the abscissa in a plot. The second score is used as the ordinate, while the higher order scores do not perform much of the discrimination so usually they are not utilized.<sup>10</sup> In the plot each spectrum represent a data point where the clustered data point represent related spectra, the centroid (group mean) is also calculated and plotted for each cluster.

In order to calculate the weight coefficients of the discriminant function ( $w_k$ ), we must define two matrices, the within-group sums of squares and cross product matrix ( $W$ ) and the between-groups sums of square and cross product matrix ( $B$ ). The matrix elements of  $W$  is given by equation 3.2,

$$W_{kl} = \sum_{i=1}^m \sum_{j=1}^{n_i} (X_{kij} - \bar{X}_{ki})(X_{lij} - \bar{X}_{li}) \quad (3.2)$$

where  $m$  is the total number of groups,  $n_i$  is the number of objects in group  $i$ ,  $X_{kij}$  is the  $k^{\text{th}}$  variable of object  $j$  in group  $i$ , and  $\bar{X}_{ki}$  is the average values of the  $k^{\text{th}}$  variables for all objects in group  $i$ . In order to calculate  $B$ , we have to define the matrix of the total sums of squares and cross products ( $T$ ), its elements given by equation 3.3.

$$T_{kl} = \sum_{i=1}^m \sum_{j=1}^{n_j} (X_{kij} - \bar{X}_k)(X_{lij} - \bar{X}_l) \quad (3.3)$$

The matrix of between-groups sums-of-squares can be calculated from the difference between  $T$  and  $W$ :

$$B = T - W \quad (3.4)$$

The goal is to maximize the between-groups differences and minimize the within-group differences, this can be achieved by solving the eigenvalue problem which maximizing the value of  $\{\det(B)/\det(W)\}$ . The resultant eigenvalues  $\lambda$  are given by equation 3.5,

$$\lambda = \frac{\hat{b}^T B \hat{b}}{\hat{b}^T W \hat{b}} \quad (3.5)$$

where  $b$  represent the corresponding eigenvectors. Equation 3.5 can be written as,

$$(B - \lambda W) \hat{b} = 0 \quad (3.6)$$

The solution of equation 3.6 leads to a set of eigenvalues  $\lambda$  and eigenvectors  $b$ , the eigenvector corresponding to the highest eigenvalue represent the most significant discriminant function responsible for the major variations between the groups. Then the discriminant function scores can be calculated easily from the equation  $f = \hat{b}^T X$ , and so the location of all the objects in all groups in 2-dimensions can be determined by plotting the first and second discriminant function scores. The DFA plot represent the classification of the spectra obtained from different bacterial samples based on the intensity of the Raman features that reflect the molecular compositions of the samples.

To sum up, multivariate methods are important in analyzing Raman spectra because the spectra are high dimensional and contain many features, so the identification of the microorganisms cannot be achieved without those statistical tools. Figure 3.8 shows a schematic diagram representing the procedure of multivariate statistical analysis performed on the Raman spectra in this dissertation. PCA reduces the dimensionality of the processed data from 2070

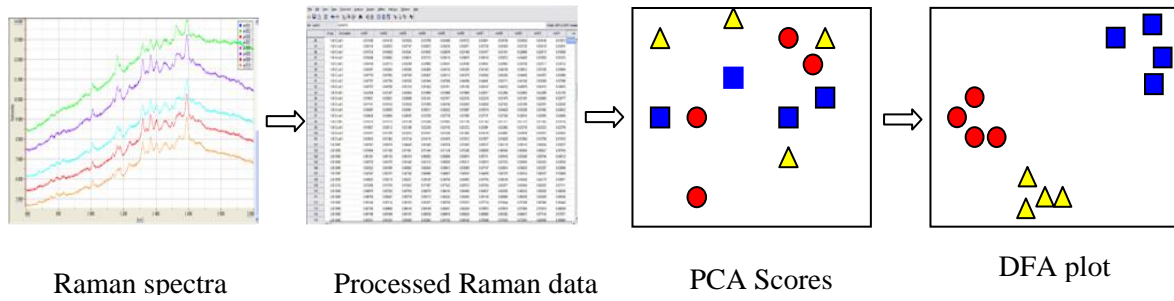


**Figure 3.8:** The procedure of multivariate analysis on Raman spectra.

down to approximately 13 uncorrelated PC scores. A DFA is then performed on the PC scores to discriminate between groups based on the PC scores.<sup>15</sup> As an example of the results of such an analysis, a PC/DFA plot of three different strains of bacterial spectra is shown in Figure 3.9. Again each colored data point represents the first two discriminant scores of a single spectrum in this 2-dimensional plot.

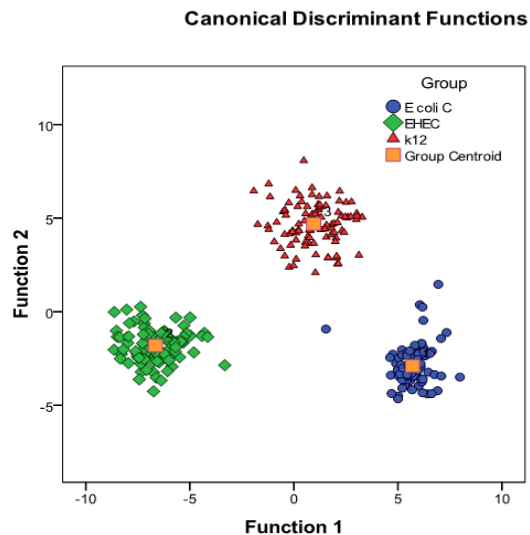


**Figure 3.9:** Example of DFA plot using two discriminant functions.

### CHAPTER 3 REFERENCES

- <sup>1</sup> E.H. van Veen and M.T.C. de Loos-Vollebregt. "Application of mathematical procedures to background correction and multivariate analysis in inductively coupled plasma-optical emission spectrometry," *Spectrochimica Acta B* **53**:639–669 (1998).
- <sup>2</sup> C.A. Lieber and A. Mahadevan-Jansen. "Automated method for subtraction of fluorescence from biological Raman spectra," *Applied Spectroscopy* **57**:1363-1367 (2003).
- <sup>3</sup> A. Cao, A. K. Pandya, G.K. Serhatkulu, R.E. Weber, H. Dai, J.S. Thakur, V.M. Naik, R. Naik, G.W. Auner, R. Rabah, and D.C. Freeman, "A robust method for automated background subtraction of tissue fluorescence," *J. Raman Spectr.* **38**:1199-1205 (2007).
- <sup>4</sup> W. R. Dillon and M. Goldstein, *Multivariate Analysis Methods and Applications*, John Wiley & Sons (1984).
- <sup>5</sup> I. T. Jolliffe, *Principal Component Analysis*, Springer-Verlag: New York (1986).
- <sup>6</sup> D. Naumann, *Infrared spectroscopy in microbiology*, in *Encyclopedia of Analytical Chemistry*, R.A. Meyers (Ed.), John Wiley & Sons Ltd, Chichester (2000).
- <sup>7</sup> A.M.C. Davies, *Back to the basics: applications of principal component analysis*, *Spectroscopy Europe* 17(2): 30-31 (2005).
- <sup>8</sup> B.F.J. Manly, *Multivariate Statistical Methods: A Primer*, Chapman &Hall: London (1994).
- <sup>9</sup> S.K. Kachigan, *Statistical Analysis- An Interdisciolar Introduction to Univariate and Multivariate Methods*, New York (1986).
- <sup>10</sup> P.A. Lachenbruch, *Discriminant Analysis*, NY: Hafner (1975).
- <sup>11</sup> K. Yang and J. Trewn, *Multivariate Statistical Methods in Quality Management*, New York (2004).
- <sup>12</sup> R.G. Brereton, *Applied chemometrics for scientists*. Chapter 5, "Pattern recognition." John Wiley & Sons Ltd., Chichester (2007).
- <sup>13</sup> J.F. Hair, W.C. Black, B.J. Babin, and R.E. Anderson, *Multivariate Data Analysis*, 7<sup>th</sup> Edition, Prentice Hall (2009).
- <sup>14</sup> W.R. Klecka, *Discriminant Analysis*, Newbury Park, Sage publications Inc., CA (1980).
- <sup>15</sup> R. Goodacre, E.M. Timmins, R. Burton, N.Kaderbhai, A.M. Woodward, D.B. Kell, and P.J. Rooney, "Rapid Identification of Urinary Tract Infection Bacteria Using Hyperspectral Whole-Organism Fingerprinting and Artificial Neural Networks", *Microbiology*, **144**, 1157-1170 (1998).

## Chapter 4

### Raman Spectroscopy for the Discrimination of Bacterial Strains

#### 4.1 *E. coli* bacterial strains

##### 4.1.1 Introduction

*Escherichia coli* is a Gram-negative bacterium named after the German bacteriologist Escherich who discovered it in 1885.<sup>1</sup> This genera includes many non-pathogenic strains such as the useful strains that live in the gastrointestinal tract, it produces vitamin K<sub>2</sub>,<sup>2</sup> and stops the growth of other pathogenic bacteria.<sup>3</sup> Some pathogenic strains such as the O157:H7 strain can cause major public health concerns due to its ability to poison food.<sup>4,5</sup>

The harmless strains of *E. coli* are also used as an indicator of water contamination in rivers and lakes. Since they can survive for a short time outside the host intestine, their presence in a certain number (in Michigan 300 or more per 100 ml water) in the surface water of beaches indicates that there is a fecal contamination which requires a closure of that beach to avoid any disease risk in the region.<sup>1</sup>

The fact that *E. coli* can be cultured and duplicated *in vitro* easily makes it a good model of bacteria to be studied using Raman spectroscopy. Many strains were fully characterized genetically which allow a good comparison between the results.

In this work Raman spectroscopy was evaluated as a sensitive identification tool of *Escherichia coli* at the strain level. Four closely-related well-characterized strains of *E. coli* including an avirulent laboratory derivative of the pathogenic strain *E. coli* O157:H7, and three non-pathogenic laboratory strains (*E. coli* C, *E. coli* Hfr K-12 and *E. coli* HF4714, a hybrid of

strains K-12 and C), were selected for this study. A previous study of the chromosome sequence of *Hfr* K-12 and *E. coli* O157:H7 revealed that *E. coli* O157:H7 has evolved from *Hfr* K-12 after the attack of a lysogenic bacteriophage.<sup>6,7</sup> Many Raman spectra were obtained from multiple colonies of each strain to investigate the reproducibility of the spectra and to provide a large data base for this study. Principal component analysis was used to reduce the dimensionality of data from 2070 to 40 PCs and discriminant function analysis classified all the PCA-reduced-spectra into independent categories depending on similarities and differences in the molecular composition of the bacterial strains.

Blind classification tests were performed using reference libraries composed of varying numbers of model spectra to determine if the Raman spectrum alone is sufficient to classify the bacteria by strain and to determine how large a pre-compiled reference library of model spectra needs to be (relative to the number of unknown spectra being identified) to insure accurate identification.

#### **4.1.2 Bacterial Strains and Culture Conditions**

All *E. coli* samples were prepared in a similar manner. Bacterial cells were cultured overnight in a nutrient broth medium at 37 °C, then 1 µL of the suspension was streaked on a trypticase soy agar TSA plates using a sterilized inoculating loop. The plates were then incubated at 37 °C for 24 hours. Single colonies of grown cells were harvested from the plates using an inoculating loop and suspended in 1.5 ml of deionized water. These aliquots were centrifuged for 3 minutes at 5000 rev/min at room temperature to create a suspension. The supernatant and traces of the media were discarded. In all cases, a final bacterial titer of approximately 10<sup>8</sup> cells was utilized.

### 4.1.3 Internal Validation

Internal validation of our data was performed by constructing a PCA-DFA model from known bacterial strains and testing new unknown spectra from the same strains against the model.<sup>8</sup> The complete dataset of 478 Raman spectra from all four strains was divided into two sets: a training set that contained model spectra whose identities were known and a test set that contained the rest of the spectra with their identities removed. Determining the appropriate size of the training set relative to the test set was a key goal of this study. The data sets were then input into the SPSS software as either “known” or “unknown” and PCA and DFA were performed. Classifications of the unknown test set spectra were then made based on the similarities and differences between the test set spectra and the known training set spectra.

## 4.2 *E. coli* Results and Discussion

478 bacterial Raman spectra were acquired in the spectral region (600-2000)  $\text{cm}^{-1}$  from numerous aliquots isolated from multiple cultures to eliminate day-to-day variations, to reduce the effects of growth condition variability, and to ensure data reproducibility. Figure 4.1 shows the average of all the processed Raman spectra acquired for each of the strains under investigation. Bacterial Raman spectra consist of bands representing the cell contents, primarily proteins, lipids, carbohydrates and nucleic acids. For example the peaks located at 1005 and 1662  $\text{cm}^{-1}$  were assigned for proteins,<sup>9,10</sup> the peak at 1585  $\text{cm}^{-1}$  assigned for lipids,<sup>11</sup> the peak at 1451  $\text{cm}^{-1}$  assigned for carbohydrates or lipids,<sup>9,10</sup> the small peaks located at 1035 and 1128  $\text{cm}^{-1}$  were assigned for carbohydrates,<sup>12</sup> while the peak at 784  $\text{cm}^{-1}$  was assigned for nucleic acids.<sup>9</sup> These spectral bands were found to be consistent with those published previously.<sup>13,12</sup>

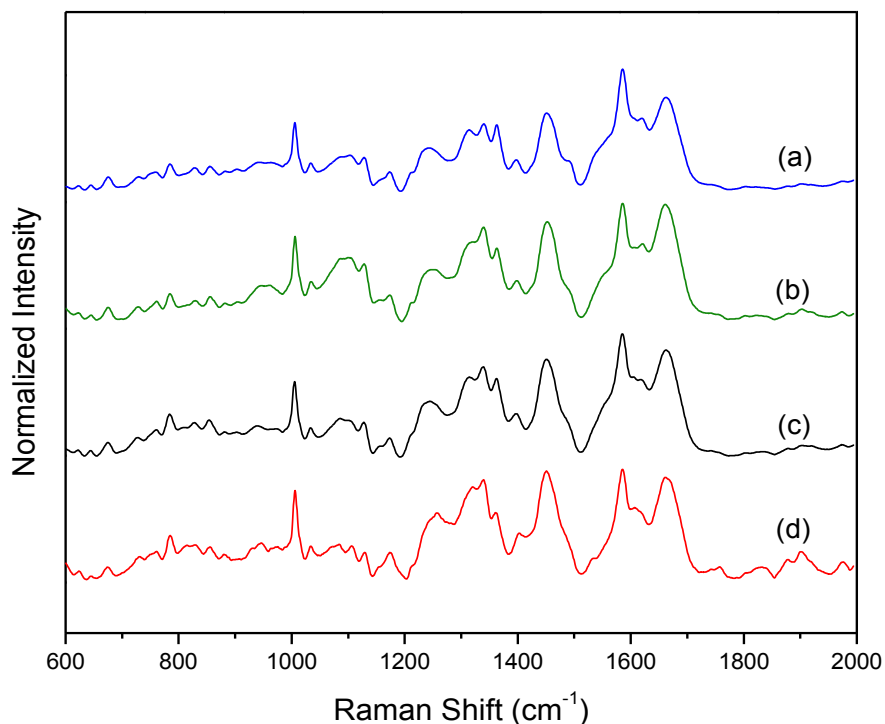


**Figure 4.1:** A comparison of the normalized averaged Raman spectra of the four *E.coli* strains studied in this work: (a) *E.coli* C, (b) *E. coli* O157:H7, (c) *E.coli* K-12, (d) *E.coli* HF4714. Spectra have been offset vertically for clarity.

The observed qualitative similarity of the spectra reveals the similarity of the biochemical compositions of the strains. To evaluate the quantitative differences between these strains, the multivariate statistical methods of PCA and DFA were utilized, as explained above. Figure 4.2 shows the PC-DFA plot for the four *E. coli* strains. Each colored point represents a spectrum which is plotted against its DF1 and DF2 scores. The four main groups were recovered with high reproducibility and the avirulent pathogenic strain (*E. coli* O157:H7) was recovered in a cluster much separated from the other strains. The classification accuracy of this PC-DFA as determined by a “leave one out” analysis was: 100% of *E. coli* O157:H7, 99.3% of *E. coli* C, 99.4% of *E. coli* K-12, and 98.7% of *E. coli* HF4714 spectra were correctly identified.

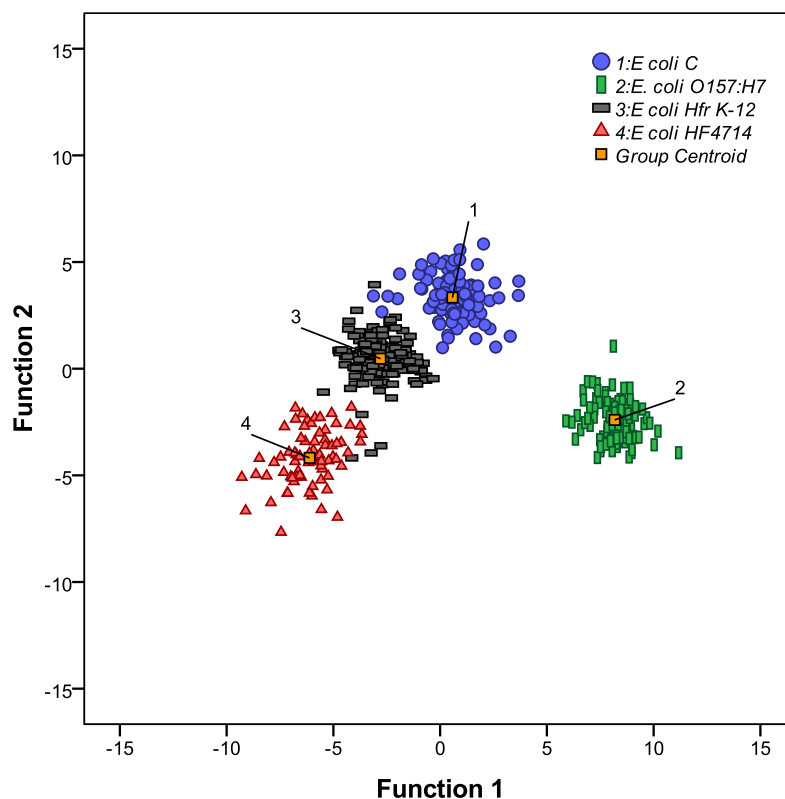


**Figure 4.2:** A PC-DFA plot showing the first two discriminant function scores of all the Raman spectra. The clustering of the spectra about their respective centers of mass demonstrates the high-degree of reproducibility of the spectra and the ability to discriminate between the four strains.

In order to investigate the reason for the large difference between *E. coli* O157:H7 spectra and the spectra from the non-pathogenic strains, we identified the spectral regions most important for discrimination by comparing the plot of the first PC loading with the spectral differences between the average spectra. This difference was obtained by simply subtracting the spectra from each other. Figure 4.3 reveals the similarity between the PC1 loading plot and the difference between the average spectra of *E. coli* O157:H7 and the average spectrum of *E. coli* C. The differences in the intensities of the main strong peaks located at 1338, 1454, and 1658  $\text{cm}^{-1}$  represent the spectral features that possess the most variance in the data and are thus utilized as

the main basis for discrimination. Those peaks are observed in all spectra and have been previously assigned for protein or DNA,<sup>14,15</sup> carbohydrates, and protein respectively.

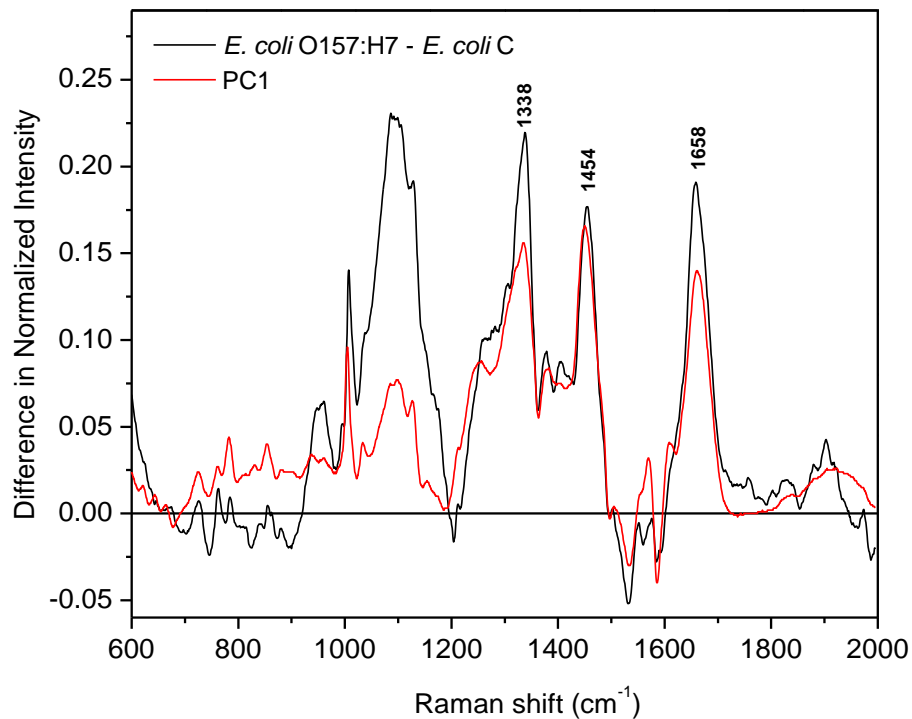


**Figure 4.3:** The first principal component loading of the PCA (red) plotted with the difference of the average Raman spectrum of *E. coli* O157:H7 and *E. coli* C bacteria (black). A strong correlation between these two shows that the difference between pathogenic *E. coli* O157:H7 and *E. coli* C particularly in the Raman bands at 1658, 1454, and 1338 cm<sup>-1</sup> represents a significant amount of the overall variance in the data.

#### 4.2.1 Blind Study: Internal Validation

Internal validation was used to evaluate the ability of Raman spectroscopy to accurately differentiate closely related *E. coli* strains based on the strains' biochemical variation. In our initial study, of the 478 total Raman spectra, 161 spectra (1/3) were utilized in the model as a training set and 317 spectra (2/3) were used as a blind test set to be classified against the training set using the PC-DFA. To do this, spectra from each of the strains were randomly selected such that 1/3 of the spectra from each strain were represented in the training set and 2/3 of the spectra from each strain were present in the test set. The identities of the four species in the training set were not provided, but they were classified generically as "Group 1," "Group 2," etc. No information about the test set spectra was provided at all and the order of all the spectra in the test set was randomly shuffled in every analysis. The PC-DFA was then performed on the test set using the model constructed by the training set and the unidentified test spectra were classified. Only then were the identities of the test spectra revealed.

This PC-DFA correctly identified 312 of the 317 spectra in the test set, yielding a 98.4% overall identification accuracy at the strain level. Figure 4.4 shows the PC-DFA ordinate plot of all the spectra. 100% (66/66) of the *E. coli* O157:H7 spectra, 94% (47/50) of the HF4714 spectra, 99% (106/107) of the K-12 spectra, and 98.9% (93/94) of the C spectra were identified correctly. In this Figure solid symbols represent spectra in the training sets and open symbols represent the unidentified test sets.

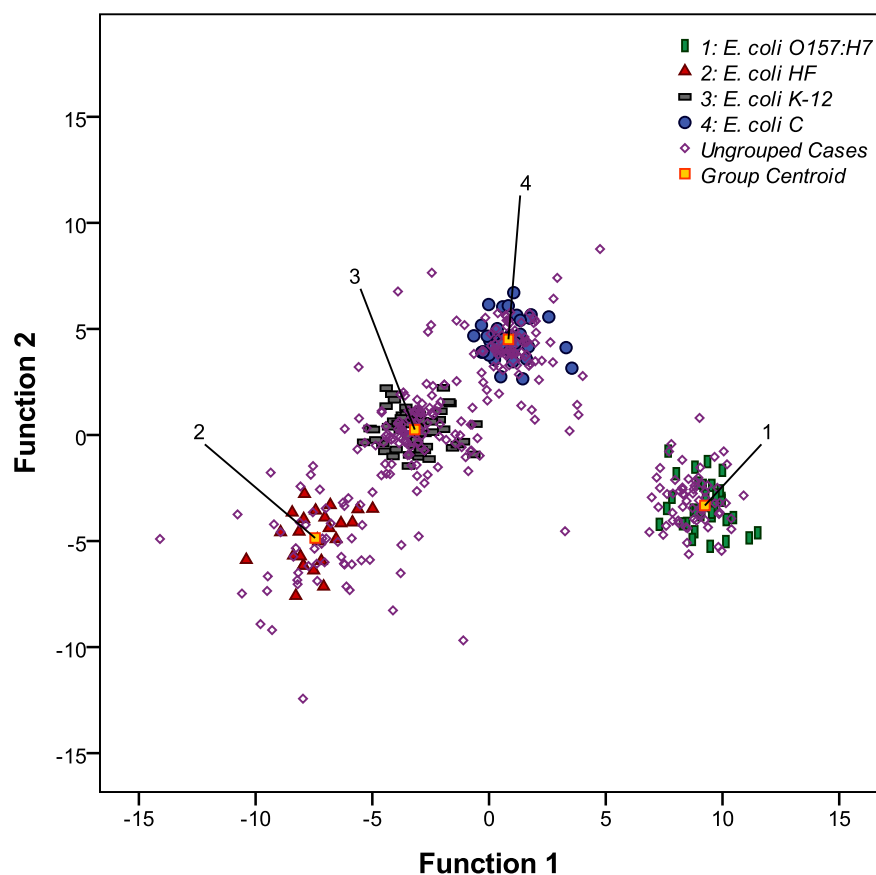


**Figure 4.4:** PC-DFA plot of 478 spectra obtained from four *E. coli* strains. The identified grouped cases (1 through 4) represent the 161 model spectra of the training set and the unidentified ungrouped cases represent the 317 spectra of the test set. The ungrouped cases clustered around their respective model spectra as revealed after the identities of the unknown spectra were revealed.

To investigate the effect that the size of the training set relative to the size of the test set had on identification accuracy, this internal validation test was repeated with different numbers of model spectra in the training set relative to the size of the test set. Table 4.1 shows the results for all the replicates. In all cases, almost equal fractions of the spectra from all strains were used in the training sets rather than equal numbers of spectra. For example in the replicate with the smallest number of model spectra in the training set, 12.6%, 11%, 11.3%, and 12% of the spectra

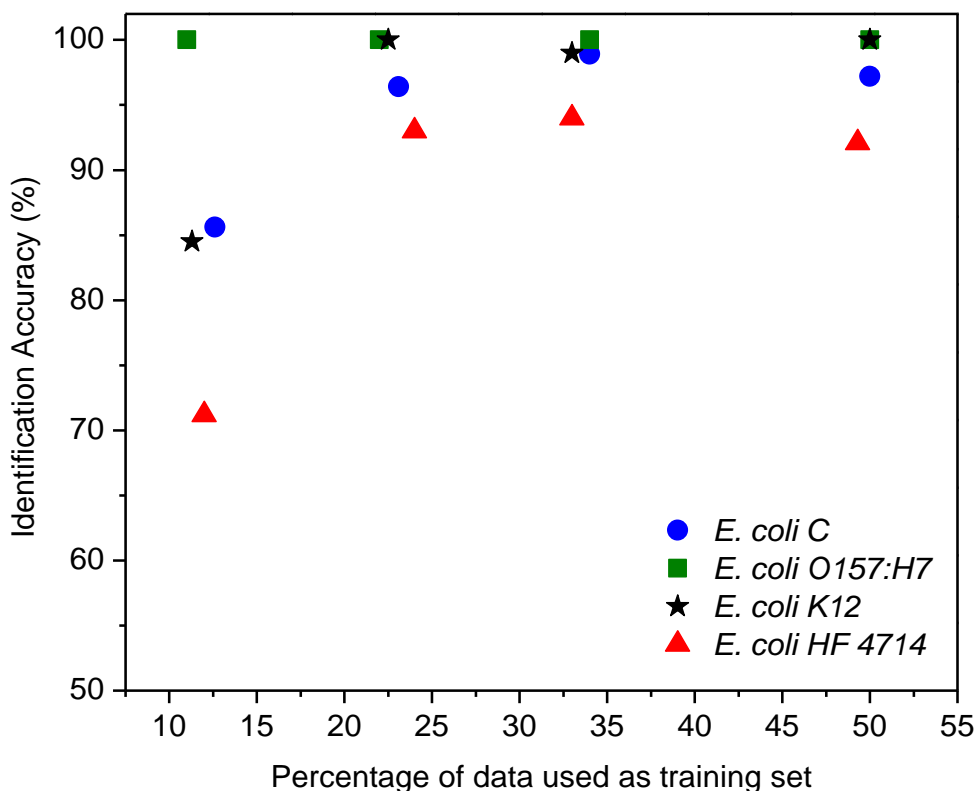
obtained from the four strain groups was used in the training set. When the smallest training set consisting of 56 model spectra was used, the correct identification accuracy of the 422 remaining spectra in the test set was lowest at 86%. This indicated that the number of spectra in the training set (representing about 11% of the total data) was not enough for accurate identification.

Table 4.1: Identification results of the internal validation test.

<b>E. coli strain</b>	<b># of Spectra in Training Set (percentage)</b>	<b># of Spectra in Test Set (percentage)</b>	<b># of Misidentified Spectra</b>	<b>% Correct Classification Rate</b>
<i>E. coli</i> C	18 (12.6%)	125 (87.4%)	18	85.6%
	33(23.1%)	110 (76.9%)	4	96.4%
	49 (34%)	94 (66%)	1	98.9%
	72 (50%)	71 (50%)	2	97.2%
<i>E. coli</i> O157:H7	11 (11%)	89 (89%)	0	100%
	22 (22%)	78 (78%)	0	100%
	34 (34%)	66 (66%)	0	100%
	50 (50%)	50 (50%)	0	100%
<i>E. coli</i> K-12	18 (11.3%)	142 (88.7%)	22	84.5%
	36 (22.5%)	124 (77.5%)	0	100%
	53 (33%)	107 (67%)	1	99%
	80 (50%)	80 (50%)	0	100%
<i>E. coli</i> HF4714	9 (12%)	66 (88%)	19	71.2%
	18 (24%)	57 (76%)	4	93%
	25 (33%)	50 (67%)	3	94%
	37 (49.3%)	38 (50.7%)	3	92.1%

By increasing the size of the training set to include 109 spectra (representing about 22% of the total data) the accuracy of the unidentified test set spectra increased to 97.8% and it increased further to 98.4% for a training set containing 161 spectra (representing about 33% of the total data). Beyond this point, the identification accuracy did not increase due to the addition of more spectra in the training set. This established there is a minimum amount of data that must be used as a training set to construct a model, but that there is a diminishing return in accuracy as the size of the training set increases. The general correlation between the size of the training set relative to the test set and the accuracy of identification is shown in Figure 4.5.

Interestingly, the results revealed that the pathogenic strain (*E. coli* O157:H7) was correctly identified even when a low number of model spectra were used in the training set. This indicated that the pathogenic *E. coli* spectra are identifiably distinct from the spectra of the other non-pathogenic strains. For the other, more similar non-pathogenic *E. coli*, identification accuracy dropped considerably when only 12% of the available spectra were included in the training set.



**Figure 4.5:** The general correlation between the size of the training set used in the model to identify the unknown spectra (as a function of percentage of the total number of spectra) and the accuracy of identification of the unidentified test spectra, by strain. *E. coli* O157:H7 was always reliably identified in the PC-DFA, but accuracy dropped significantly for the other more similar strains when the trainings set consisted of only approximately 12% of the data.

#### 4.2.2 *E. coli* Conclusions

In this study Raman spectroscopy combined with the multivariate statistical techniques of PCA and DFA have been used to distinguish between four *E. coli* strains and to classify unknown Raman spectra for rapid, autonomous identification. The spectra showed a high degree of reproducibility over days and months which can be noticed by visual inspection of the spectra. The results of the analysis showed that the Raman spectrum of the pathogenic strain *E. coli*

O157:H7 was significantly different from the other non-pathogenic strains under investigation. Moreover, the identification results obtained by an internal validation test showed a high identification accuracy at the strain level that has never been achieved before. Specifically, a 100% discrimination ability was found for the pathogenic strain compared to three non-pathogenic strains even when the number of model spectra included in the training set was relatively low.

### **4.3 *E. coli* Summary**

Visible wavelength Raman spectroscopy has been used for the discrimination of four closely related *Escherichia coli* strains: *E. coli* O157:H7, *E. coli* C, *E. coli* Hfr K-12, and *E. coli* HF4714. Raman spectra were acquired from live bacterial aliquots obtained from cultures grown on trypticase soy agar plates. A principal component-discriminant function analysis of the full Raman spectra revealed robust, reproducible differences between these strains, allowing accurate identification of unknown bacterial spectra by comparison against a precompiled library of known spectra. The laboratory avirulent strain of pathogenic *E. coli* O157:H7 possessed the most significant spectral differences and was easily discriminated from the other non-pathogenic *E. coli* strains. A blind study approach was used to evaluate the potential of this technique to identify or classify unknown bacteria at the strain level. The results of the test revealed a 100% correct identification for the *E. coli* O157:H7 strain, 98.9% for *E. coli* C, 99% for *E. coli* K-12, and 94% for *E. coli* HF4714 when the training set contained 1/3 of the total number of spectra taken and the other two-thirds of the data were used as unknown test spectra. A correlation between the number of spectra present in the training set and the identification accuracy was

found. This study suggests that non-surface-enhanced visible wavelength Raman spectroscopy is potentially useful for the identification and classification of bacteria at the strain level.

## **4.4 *Staphylococcus aureus* Bacterial Strains**

### **4.4.1 Introduction**

*Staphylococcus aureus* is a Gram-positive pathogenic bacteria species responsible for a wide range of diseases like skin infections and pneumonia. Many of its strains can cause food poisoning due to their production of toxins. Hospital-acquired infections (HAI) and community-acquired infections (CAI) due to *Staphylococcus aureus* is one of the leading concerns to public health. For example, methicillin-resistant *Staphylococcus aureus* (MRSA) that is carried by about 60% of nurses nasally or on their skin<sup>16</sup> is responsible for pneumonia and infections in open wounds, the respiratory tract, and the urinary tract which can lead to death in hospitalized patients.<sup>17</sup> According to an estimation of the Centers for Disease Control and Prevention (CDC), MRSA infections doubled from 1999 to 2005 and the number of deaths increased significantly in this time period.<sup>18</sup> Because the antibiotic resistance in this pathogenic strain is so commonly observed and so dangerous, there is a need for a system which can discriminate between the different strains rapidly in order to initiate the proper treatment in a timely fashion.

Raman spectroscopy has already been presented as an efficient technique for discrimination between different *Staphylococcus* strains belonging to different species.<sup>10</sup> Also, Raman spectroscopy has been used to characterize methicillin-resistant coagulase staphylococci (MR-CNS) isolates obtained from hospital patients' skin.<sup>19</sup>

In this study, the efficacy of Raman in differentiating the strains of *S. aureus* which were resistant to different classes of antimicrobials ( $\beta$ -lactam, macrolide, and tetracycline) was

evaluated. The Raman instrumentation discussed previously was used to collect the data from bacterial colonies in the spectral region  $600\text{-}2000\text{ cm}^{-1}$ , PCA was performed to reduce the data dimension from 2070 to 13 PCs, and DFA was performed on the PCs to distinguish between the different spectra.

#### **4.4.2 Bacterial Strains and Culture Conditions**

Four different strains of *Staphylococcus aureus* were used in this study: methicillin resistant *Staphylococcus aureus* (MRSA), methicillin sensitive *Staphylococcus aureus* (MSSA), tetracycline resistant *Staphylococcus aureus* (TRSA), and multi-drug resistant *Staphylococcus aureus* (DRSA). The isolates were isolated from retail meat and confirmed by PCR. They were characterized by antimicrobial susceptibility testing. .

The isolates were stored at  $-80^{\circ}\text{C}$  in brain heart infusion broth containing 40% glycerol until they were used. All isolates were grown overnight on trypticase soy agar (TSA). These plates were incubated for 24 h at  $35^{\circ}\text{C}$ . For sample preparation, a sterilized cotton swab was filled with biomass and suspended in 50  $\mu\text{l}$  of sterilized demineralized water. This was followed by centrifugation for 2 min at  $13,000 \times g$ . The pellet was transferred to quartz slide and was allowed to dry.

## 4.5 *S. aureus* Results and Discussion

The collected Raman spectra from different bacterial samples were processed (background subtracted and normalized) and then the average spectra for the strains were calculated to represent the molecular changes between them. Figure 4.6 shows the averaged spectra for the studied strains of *S. aureus* with the main peaks labeled from 1 to 9.

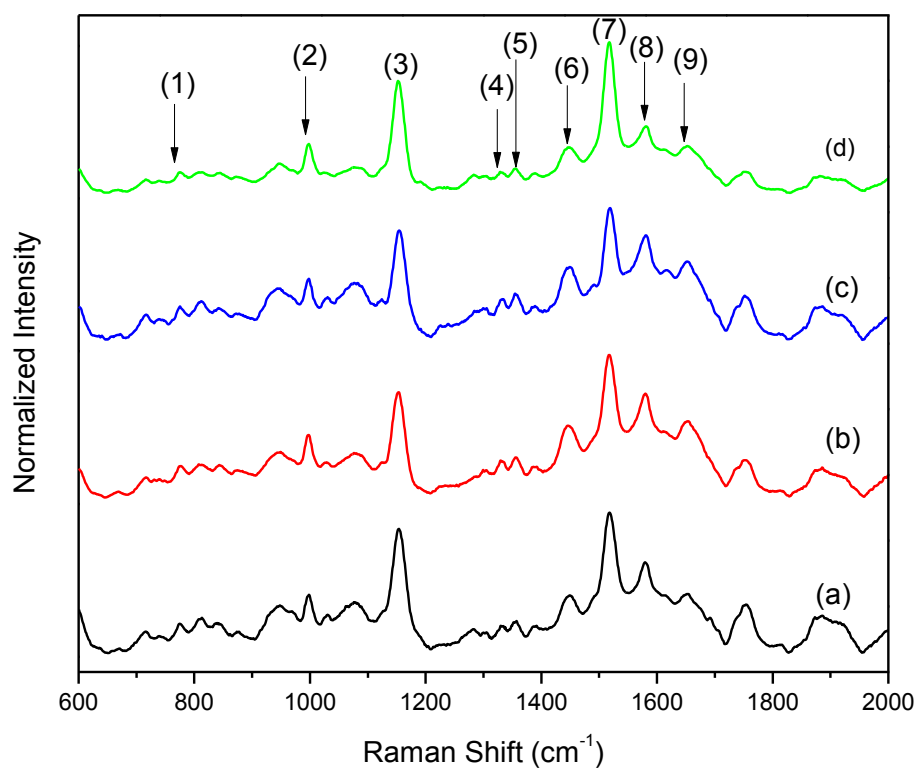


**Figure 4.6:** A comparison of the normalized averaged Raman spectra of the four *S. aureus* strains studied in this work, (a) MRSA, (b) MSSA, (c) TRSA, (d) DRSA. Spectra have been offset vertically for clarity.

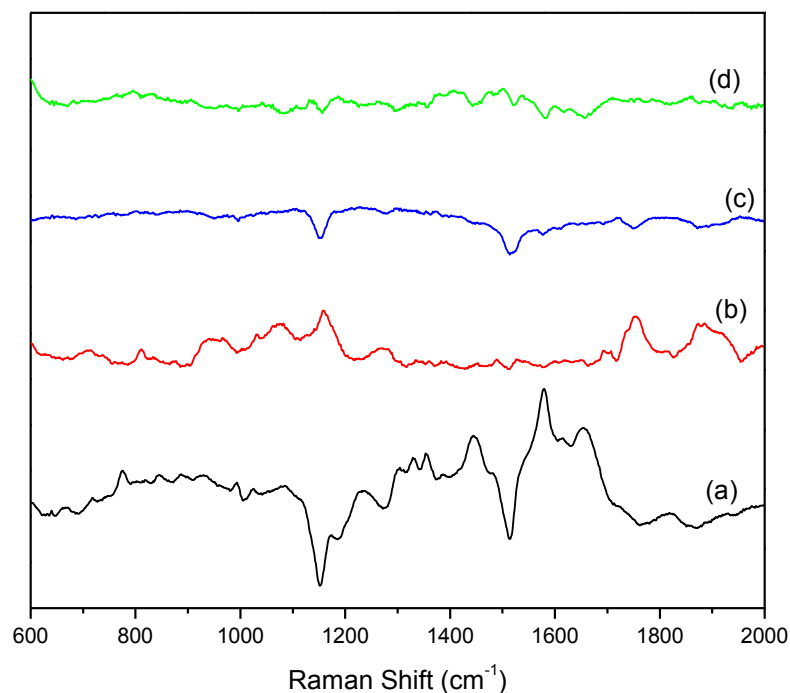
The peaks observed in Raman spectra represent the molecular composition of the dried bacterial cells which seems to be about the same for all the strains (the peak assignments are given in Table 4.2). However, a careful look at the figure reveals some slight changes between the intensities of those peaks; the differences could be addressed by the application of PCA and DFA as will be discussed below.

Table 4.2: Assignment of the Raman vibrational bands observed in *S. aureus* Raman spectra.

Raman shift (cm <sup>-1</sup> )		Assignments	
Label	<i>S. aureus</i>	Vibrational modes	Location
(1)	776 (w)	Nucleotides (Cytosine, uracil) ring stretching <sup>10,20</sup>	DNA/RNA
(2)	998 (m)	$\nu$ (C-C) aromatic ring breathing of phenylalanine <sup>10,20</sup>	Protein
(3)	1154 (s)	$\nu$ (C-C) <sup>21,22,14,23</sup>	Protein
(4)	1329 (w)	$\delta$ (C-H) <sup>10,11</sup>	Carbohydrate, protein
(5)	1355 (w)	C-H bend <sup>11</sup>	Protein
(6)	1448(m)	$\delta$ (C-H <sub>2</sub> ) scissoring <sup>10,20,,24,25</sup>	Carbohydrate, Lipid
(7)	1518(s)	$\nu$ (C=C) <sup>21,22</sup>	Protein
(8)	1580(s)	$\nu$ (C=C) <sup>11</sup>	Lipid
(9)	1653(m)	Amide I and unsaturated lipids, <sup>20,24</sup> amide I and $\nu$ (C=C) in lipid <sup>14</sup>	Protein, Lipid

$\delta$ : deformation vibration,  $\nu$ : stretching vibration,  $\rho$ : rocking vibration; s: strong, m: medium, w: weak.

To quantify the spectral differences responsible for discrimination, I compared the plot of the PC loadings with the differences between the averaged spectra of the different strains. 13 PCs were obtained from the PCA analysis, the first PC score included most of the data variance (76.8%) while the second PC included 13.1%, the third one included 3.2%, and the fourth PC just counted for 1.8% of the total variance of the data. The plots of the loadings of those PCs (shown in Figure 4.7) consist of features that represent the data variance that is considered by the statistical analysis as the discrimination basis.



**Figure 4.7:** A plot of first four PC loadings in the spectral region 600-2000  $\text{cm}^{-1}$ . (a) loads of PC1, (b) loads of PC2, (c) loads of PC3, and (d) loads of PC4.

Figure 4.8 identifies the main features in the plot of the first PC loading which contains most of the data variance. Those positive and negative peaks were related to the dominant features in the *S. aureus* strains' Raman spectra.

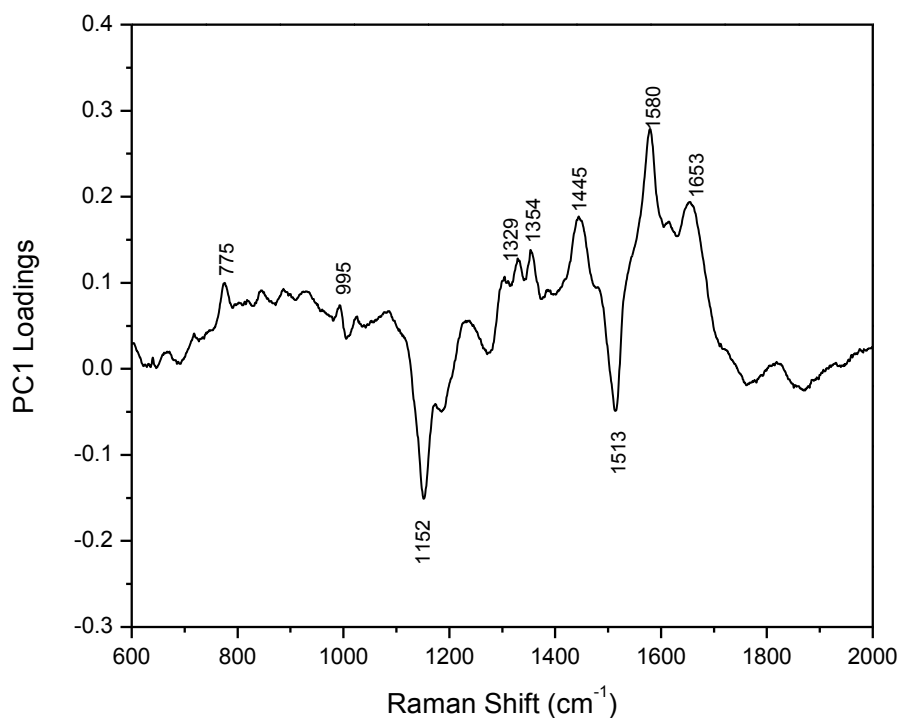


**Figure 4.8:** The loadings of the first PC with the main spectral features identified.

The first PC loadings plot was compared with the differences between the averaged spectra of different strains as shown in Figure 4.9. The comparison revealed a similarity between the PC1 loads and the difference between DRSA and the other strains spectra in the spectral region 1300-1700 cm<sup>-1</sup> as appeared in Figure 4.9(A) and 4.9(B). A match between the PC1 peak located at 1152 cm<sup>-1</sup> and the difference between MRSA and other strains spectra at this location was observed (Figure 4.9(C) and (D)). This indicates that those spectral variations

associated with a variation in the corresponding molecular compositions of the different bacteria strains were used by the statistical techniques as a fingerprint to identify each strain.

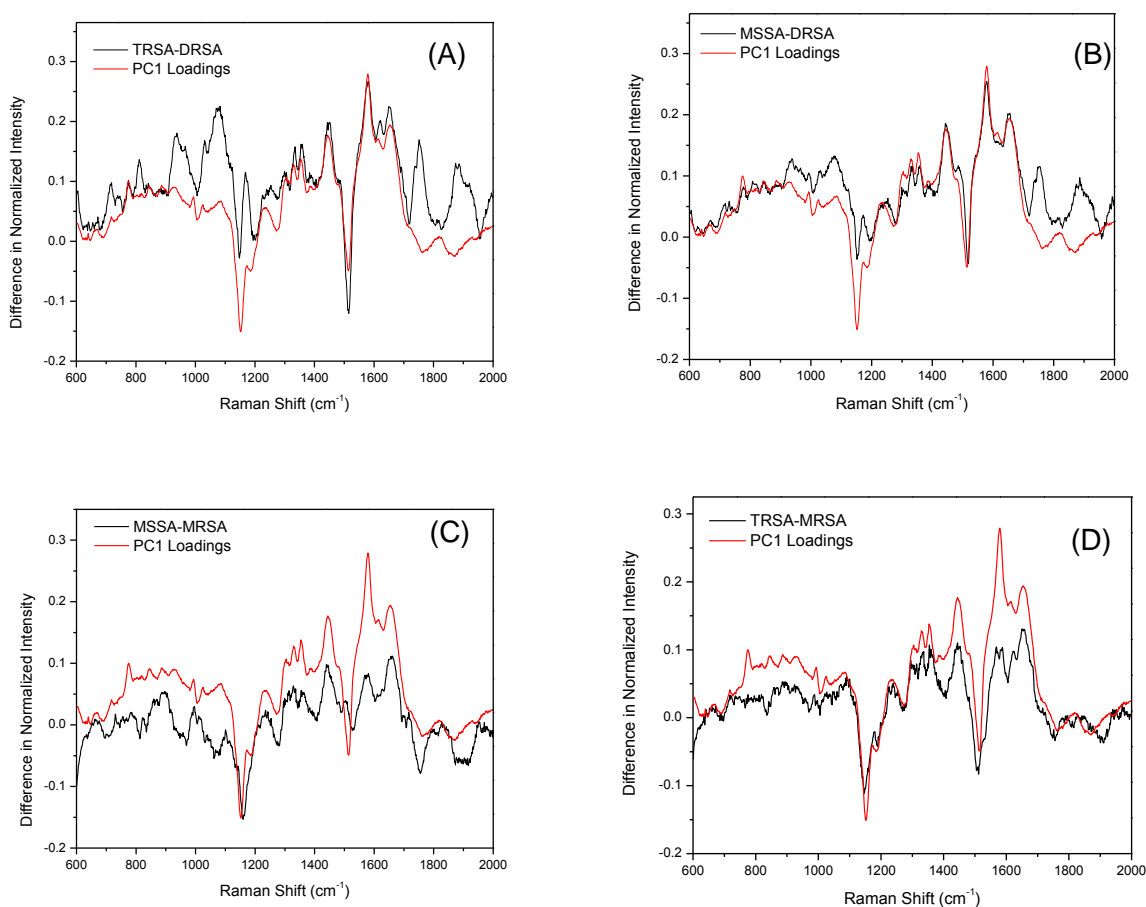


**Figure 4.9:** Principal component loadings of the PCA performed on the Raman spectra acquired from four *S. aureus* strains, (A) The loadings of the first PC plotted with the difference of the average spectrum of DRSA and TRSA. (B) PC1 loadings plotted with the difference of the average Raman spectrum of DRSA and MSSA. (C) PC1 loadings plotted with the difference of the average Raman spectrum of MRSA and MSSA. (D) PC1 loadings plotted with the difference of the average Raman spectrum of MRSA and TRSA.

To address the contribution of the second PC loadings, a correlation was found between the spectral variations between MRSA and DRSA and PC2 loading plot as shown in Figure 4.10.

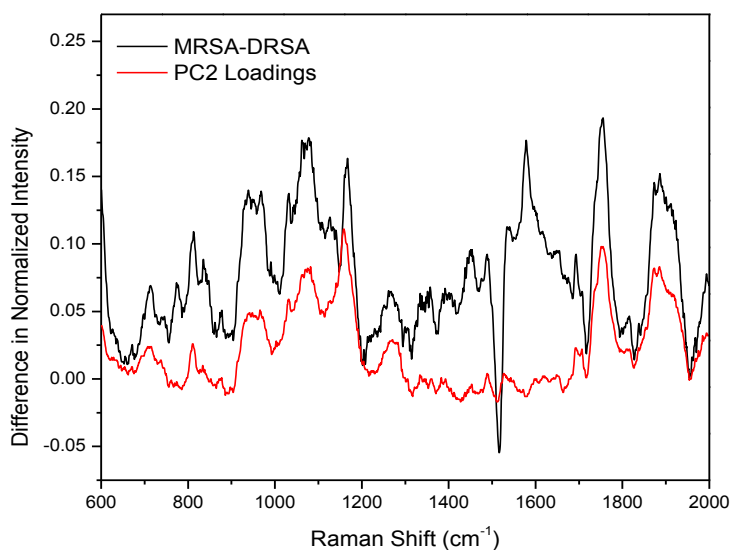


**Figure 4.10:** The loadings of the second PC plotted with the difference of the average spectrum of DRSA and MRSA.

The 13 PC scores were used as input independent variables in a discriminant function analysis. The classification results of this statistical analysis as determined by a “leave one out” analysis were: 100% of DRSA, 96% of MSSA, 96% of TRSA, and 88% of MRSA spectra were correctly identified. The grouping of the spectra representing those strains is shown in the resultant PC-DFA plot (Figure 4.11).

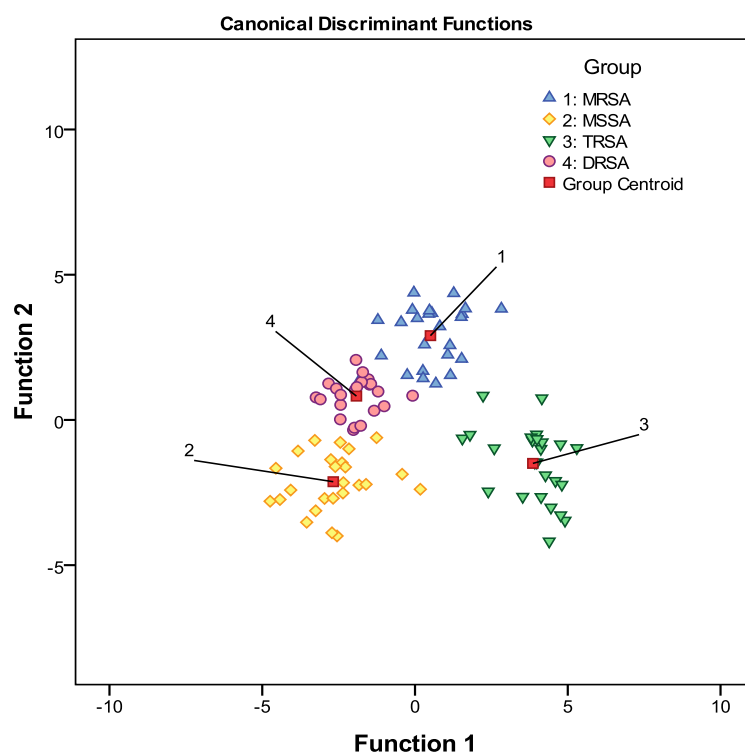


**Figure 4.11:** A PC-DFA plot showing the first two discriminant function scores of all the Raman spectra obtained from the four strains of *S. aureus*.

#### 4.6 *S. aureus* Conclusions and Summary

In this study Raman spectroscopy combined with the multivariate statistical techniques of PCA and DFA have been used to distinguish between three antibiotic resistance *S. aureus* strains: MRSA, TRSA, DRSA, and one antibiotic sensitive strain MSSA. Raman spectra were obtained from live bacterial aliquots obtained from cultures grown on trypticase soy agar plates. Reproducible variations between these strains were noticed utilizing the principal component-discriminant function analysis of the full Raman spectra. 13 PC scores accounting for 97.83% of the data variation were obtained and used as the input independent variables in DFA. The results of the analysis showed a 100% correct identification for the DRSA strain, 96% of MSSA, 96%

of TRSA, and 88% of MRSA strain spectra. The main peaks that were responsible for the classification were identified. These preliminary results are so encouraging since they verify the ability of Raman spectroscopy to differentiate those important strains. In the long-term, many more spectra are required to confirm this result and more experiments should be conducted to see if there are any commonalties among all the resistant strains or are they all just randomly different, so the ultimate goal is to use Raman fingerprint of different strains of antibiotic resistant *Staphylococcus aureus* to cure the infections in hospitals by identifying the particular strain/antibiotic in a short time.

## CHAPTER 4 REFERENCES

- <sup>1</sup> P. Feng, S. Weagant, and M. Grant. "Enumeration of *Escherichia coli* and the coliform bacteria," (2002). *Bacteriological Analytical Manual (8th ed.)*. FDA/Center for Food Safety & Applied Nutrition. Retrieved (2007).
- <sup>2</sup> R. Bentley and R. Meganathan. "Biosynthesis of vitamin K (menaquinone) in bacteria," *Microbiology Revision* **46**:241–280 (1982).
- <sup>3</sup> S. Hudault, J. Guignot, and A.L. Servin. "*Escherichia coli* strains colonising the gastrointestinal tract protect germfree mice against *Salmonella typhimurium* infection," *Gut* **49**:47–55 (2001).
- <sup>4</sup> P.S. Mead and P.M. Griffin. "*Escherichia coli* O157:H7," *Lancet* **352**:1207-1212 (1998).
- <sup>5</sup> H.M. Al-Qadiri, M. Lin, A.G. Cavinato, and B.A. Rasco. "Fourier transform infrared spectroscopy, detection and identification of *Escherichia coli* O157:H7 and *Alicyclobacillus* strains in apple juice," *International Journal of Food Microbiology* **111**:73-80 (2006).
- <sup>6</sup> T. Hayashi, K. Makino, M. Ohnishi, K. Kurokawa, K. Ishii, K. Yokoyama, C.-G. Han, E. Ohtsubo, K. Nakayama, T. Murata, M. Tanaka, T. Tobe, T. Iida, H. Takami, T. Honda, C. Sasakawa, N. Ogasawara, T. Yasunaga, S. Kuhara, T. Shiba, M. Hattori, and H. Shinagawa. "Complete genome sequence of Enterohemorrhagic *Escherichia coli* O157:H7 and genomic comparison with laboratory strain K-12," *DNA Research* **8**:11-22 (2001).
- <sup>7</sup> R. Claender, *The bacteriophages*. Plenum, New York, (1998).
- <sup>8</sup> H. Oberreuter, H. Seiler, and S. Scherer. "Identification of coryneform bacteria and related taxa by Fourier-transform infrared (FT-IR) spectroscopy," *International Journal of Systematic and Evolutionary Microbiology* **52**:91-100 (2002).
- <sup>9</sup> E. Huang, R.I. Griffiths, I.P. Thompson, M.J. Bailey, and A.S. Whiteley. "Raman microscopic analysis of single microbial cells," *Analytical Chemistry* **76**:4452-4458 (2004).

- <sup>10</sup> M. Harz, P. Rosch, K.-D. Peschke, O. Ronneberger, H. Burkhardt, and J. Popp. “Micro-Raman spectroscopic identification of bacterial cells of the *genus Staphylococcus* and dependence on their cultivation conditions,” *Analyst* **130**:1543-1550 (2005).
- <sup>11</sup> M.L. Laucks, A. Sengupta, K. Junge, E J. Davis, and B.D. Swanson. “Comparison of psychroactive arctic marine bacteria and common mesophilic bacteria using surface-enhanced Raman spectroscopy,” *Applied Spectroscopy* **59**:1222-1228 (2005).
- <sup>12</sup> Y. Liu, L.He, A. Mustapha, H. Li, Z.Q. Hu and M. Lin. “Antibacterial activities of zinc oxide nanoparticles against *Escherichia coli* O157:H7,” *Journal of Applied Microbiology* **107**:1193-1201 (2009).
- <sup>13</sup> J.W. Chan, H. Winhold, M.H. Corzett, J.M. Ulloa, M. Cosman, R. Balhorn, and T. Huser. “Monitoring dynamic protein expression in living *E. coli* bacterial cells by laser tweezers Raman spectroscopy,” *Cytometry A* **71A**:468-474 (2007).
- <sup>14</sup> I. Notingher. “Raman spectroscopy cell-based biosensors,” *Sensors* **7**:1343-1358 (2007).
- <sup>15</sup> L.J. Goeller and M. R. Riley. “Discrimination of bacteria and bacteriophages by Raman spectroscopy and surface-enhanced Raman spectroscopy,” *Applied Spectroscopy* **61**:679-685 (2007).
- <sup>16</sup> E. Klein, D.L. Smith, and R. Laxminarayan. “Hospitalizations and deaths caused by methicillin-resistant *Staphylococcus aureus*, United States, 1999-2005,” *Emerging Infectious Diseases* **13**:1840-1846 (2007).
- <sup>17</sup> M. Longmore, I. Wilkinson and E. Torok, *Oxford handbook of clinical medicine* (6th ed), Oxford University Press, New York (2004).
- <sup>18</sup> UK office for national statistics online. “MRSA deaths continue to rise in 2005,” (2007).

- <sup>19</sup> H.F.M. Willemse-Erix, J. Jachtenberg, H. Barutci, G.J. Puppels, A. van Belkum, M.C Vos, and K. Maquelin. "Proof of principle for successful characterization of methicillin-resistant coagulase-negative *Staphylococci* isolated from skin by use of Raman spectroscopy and pulsed-field gel electrophoresis," *Journal of Clinical Microbiology* **48**:736-740 (2009).
- <sup>20</sup> A.C. Singer, W.E. Huang, J. Helm, and I.P. Thompson. "Insight into pollutant bioavailability and toxicity using Raman confocal microscopy," *Journal of Microbiological Methods* **60**:417-422 (2005).
- <sup>21</sup> W.F. Howard, JR., W.H. Nelson, and J.F. Sperry. "A resonance Raman method for the rapid detection and identification of bacteria in water," *Applied Spectroscopy* **34**:72-75 (1980).
- <sup>22</sup> R.A. Dalterio, M. Baek, W.H. Nelson, D. Britt, J.F. Sperry, and F.J. Purcell. "The resonance Raman microprobe detection of single bacterial cells from a chromobacterial mixture," *Applied Spectroscopy* **41**:241-244 (1987).
- <sup>23</sup> A.C. Williams and H.G.M. Edwards. "Fourier transform Raman spectroscopy of bacterial cell walls," *Journal of Raman Spectroscopy* **25**:673-677 (1994).
- <sup>24</sup> W.E. Huang, R.I. Griffiths, I.P. Thompson, M.J. Bailey, and A.S. Whiteley. "Raman microscopic analysis of single microbial cells," *Analytical Chemistry* **76**:4452-4458 (2004).
- <sup>25</sup> K. Maquelin, L.P. Choo-Smith, T. van Vreeswijk, H.P. Endtz, B. Smith, R. Bennett, H.A. Bruining, and G.J. Puppels. "Raman spectroscopic method for identification of clinically relevant microorganisms growing on solid culture medium," *Analytical Chemistry* **72**:12-19 (2000).

## Chapter 5

### Raman Spectroscopy Study of Xylitol Uptake and Metabolism in Gram-Positive and Gram-Negative Bacteria and the Stability of Xylitol Metabolic Derivatives in Viridans Group Streptococci.

#### 5.1 Introduction

Xylitol is a natural five-carbon-sugar alcohol with molecular formula  $(\text{CHOH})_3(\text{CH}_2\text{OH})_2$ . Figure 5.1 shows the xylitol crystals and molecular structure.



**Figure 5.1:** Xylitol crystals (left) and xylitol molecular structure (right).

Although the exact mechanism of the efficacy of xylitol on pathogenic bacteria is not known, there is an impressive collection of clinical reports claiming its preventive action in a number of pediatric diseases. Xylitol can be safely applied as a preventive measure for diseases like pneumonia, acute otitis media (AOM), dental caries, and meningitis.<sup>1,2,3,4,5,6,7</sup> The causative pathogens of pneumonia in children are the Gram-positive *Streptococcus pneumoniae* and the Gram-negative *Klebsiella pneumoniae* with polysaccharide capsules. Both classes of bacteria are morphologically diplococci.<sup>8</sup> The pathogens causing acute otitis media (middle-ear infection of children) are the Gram-positive *S. pneumoniae* (30% of cases), the Gram-negative

bacteria *Haemophilus influenzae* (25% of cases), and *Moraxella catarrhalis* (20% of cases).<sup>9</sup> They are also diplococci.<sup>10</sup> It remains to be seen if all these pathogenic organisms contain xylitol operons and if they are capable of utilizing xylitol even in the presence of other sugars or carbon sources.

One likely explanation for xylitol efficacy involves the phosphotransferase system of streptococci and its ability to take in and metabolize different sugars depending on the current sugar environment.<sup>11</sup> It has been hypothesized that xylitol is metabolized to xylitol-5-phosphate in a “futile cycle,” which mutans group streptococci cannot utilize further and which may even be toxic to bacteria.<sup>12</sup> It has also been observed that exposure to low concentrations of xylitol results in a reduction of cell adherence to epithelial cells,<sup>13</sup> perhaps due to a disruption of polysaccharide production in the xylitol-exposed bacteria.<sup>14</sup> There is also evidence for significant ultrastructure alteration in xylitol-exposed *S. mutans*<sup>15</sup> and *S. pneumoniae*.<sup>4</sup> Careful Raman spectroscopic studies of the molecular alteration induced in xylitol-exposed streptococci may shed new light on one or more of these biomolecular processes.

The four structurally related known pentitols (or C5 polyol epimers) are xylitol, ribitol, D-arabitol, and L-arabitol. Only D-arabitol and ribitol are abundant in nature.<sup>16</sup> D-arabitol which forms 10% dry weight of certain mushrooms is capable of binding to capsules and teichoic acids of several Gram-positive bacteria. Ribitol is also present in free form in some higher plants.<sup>17,18</sup> Most of the previous work on catabolism of these compounds was done with various *Aerobacter aerogenes* strains which are now classified as *Klebsiella* or *Enterobacter* species.<sup>19,20</sup>

Reiner and Scangos have characterized the catabolism of ribitol (*rtl*+) and D-arabitol (*atl*+) in *E. coli* C and the disadvantages of a constitutive catabolite pathway.<sup>21,22</sup> Briefly, each operon contains genes for a dehydrogenase and a kinase and is under negative control. They have also shown that constitutive production of ribitol catabolic enzymes selected in response to xylitol render the same mutant more sensitive to certain other 5-carbon sugar alcohols. The ribitol operon is inducible by ribitol and the D-arabitol operon is inducible by D-arabitol. Significantly, these two operons are very closely linked and located in the *E. coli* chromosome between *metG* and *his* (histidine) genes in a mirror image arrangement, *rtlB-rtlA-rtlC-atlC-atlA-atlB*.<sup>21</sup> The *rtl* and *atl* operons are well-characterized in *E. coli* C, *Aerobacter aerogenes*, and *Klebsiella aerogenes*.<sup>23</sup> The species *Proteus*, *Klebsiella* and *Enterobacter* species are common urinary tract pathogens. However, the two other extensively used *E. coli* strains, *E. coli* K-12 and *E. coli* B, are genetically very close to *E. coli* C but surprisingly they lack the DNA region or xylitol operon (about 2.5 kb) loci involved in the utilization of ribitol (*rtl*) and D-arabitol (*atl*). The xylitol operon is located between *his* and *metG* loci and is genetically linked to the bacteriophage P2 attachment site.<sup>24</sup>

In this Chapter, I will describe the use of Raman spectroscopy to analyze the uptake and retention of xylitol in *E. coli* and *S. viridans*.<sup>25,26</sup> Also, the stability of xylitol inside *S. viridans* cells measured with Raman spectroscopy will be discussed.

## **5.2 Materials and Methods**

### **5.2.1 Bacterial Strain Selection and Growth Conditions**

I have compared the uptake of xylitol by the four well characterized strains of *E. coli*: *E. coli* K-12, JW1881-1, *E. coli* C, *E. coli* HF4714, and an ATCC strain of *Streptococcus viridans*.

*E. coli* K-12 and its flagella- and pili-negative mutant strain JW1881-1 lacking the genes to ferment xylitol were used as xylitol non-fermenting Gram-negative controls. *E. coli* C was chosen because it possesses the xylitol operon in a repressed state and *E. coli* HF4714 was chosen because it possesses the xylitol operon in a de-repressed state (operator constitutive). HF4714, as constructed by a genetic recombination between the *E. coli* K-12 donor and the *E. coli* C recipient, contains the xylitol operon in a functional state. *E. coli* C is sensitive to a single-stranded DNA-containing semi-temperate bacteriophage  $\phi$ X174 but produces very turbid plaques to its amber mutant of  $\phi$ X174am3 while HF4714 is equally sensitive to both wild type  $\phi$ X174 and  $\phi$ Xam3. *E. coli* K-12 is known to be resistant to these phages but sensitive to another temperate phage P2. The attachment site of this phage is closely linked to the ribitol or xylitol operon in *E. coli* C. Some of these characteristics are extremely useful to routinely test the genetic purity of all the *E. coli* strains used in our experiments.

The selection of a well-characterized *S. viridans* strain for this study was predicated on several factors. *S. pneumoniae*, on which the action of xylitol has previously been studied, is highly pathogenic and its inclusion in this study was not suggested for this reason. The dental pathogen *S. mutans* is a better candidate to study, however it has a well-established growth problem in common laboratory nutrition media as it is multiply auxotrophic with numerous nutritional requirements for normal growth.<sup>27</sup> *S. viridans* has several common characteristics with *S. mutans* and *S. pneumoniae*, both of which have already been shown to possess susceptibility to xylitol,<sup>4</sup> and is known to cause a variety of infections commonly associated with dental caries.<sup>28</sup> Using PCR technology with primers of 16s rRNA gene sequence, others in my research group have verified that *S. viridans* and *S. mutans* do not differ in DNA sequences. Since we are primarily concerned with the dental applications of prophylactic xylitol use, this

safe and relatively easy to grow bacterium was a very appropriate organism with which to initiate my Raman studies.

The *S. viridans* and the above mentioned *E. coli* strains were grown in BHI or TSB broth (rich liquid medium) containing a minimal amount of dextrose together with xylitol (0 - 2%). Considerable dilution of the bacteria prior to growth in xylitol was very important in these experiments. The titer was significantly reduced from  $10^8$ /ml to  $10^4$ /ml to make sure the population consisted only of planktonic cells, which ensured that the entire population attained log phase during growth in xylitol. After growth for 24 hours, both aerobically and anaerobically at 37°C, these bacterial cultures were used for Gram-staining. Then the Gram-positive *S. viridans* and the Gram-negative *E. coli* were spread respectively on two selective media, CNA and BHI, for a comparison of their purity and titer. The BHI with 1.5% agar and TSA are rich nutrient agar media and the CNA is a differential blood-agar medium that contains two antibiotics, colistin (polymyxin B) and a quinolone drug (nalidixic acid). The *Streptococci* pathogens were selectively grown on the CNA medium while the Gram-negative isolates were selected on bile-containing MacConkey-lactose media. The blood agar medium without antibiotics was used to distinguish the alpha, beta, and gamma hemolysis. *S. viridans* shows gamma hemolysis.

To study the retention of xylitol as a function of time, specimens of *S. viridans* and *E. coli* obtained from the xylitol-containing broth cultures (grown in a CO<sub>2</sub> jar) were diluted 1000-fold and then spread on xylitol-free tryptic soy agar (TSA) plates and incubated for 24 hours both aerobically and anaerobically at 37°C. To study the stability of xylitol in *S. viridans*, the incubation time of the TSA plates was increased to 72 hours. Colonies were collected every 24 hours avoiding the transfer of agar media. Bacteria were also obtained directly from the pellet

obtained by centrifugation of the xylitol-containing overnight cultures before they were spread on the TSA plates (“0 hr”). Bacterial pellets were similarly obtained from the xylitol-free broth cultures, spread on xylitol-free TSA plates and harvested at 0 hr, 24hr, 48hr and 72 hours.

In all cases, colonies were collected from these plates, suspended in 50  $\mu\text{l}$  of sterile distilled water, centrifuged, and the pellet was used for Raman spectroscopy. 10  $\mu\text{l}$  of the moist pellet was mounted on a low-fluorescence quartz microscope slide and allowed to dry in air prior to Raman spectroscopy. In all cases, a final bacterial titer of approximately  $10^8$  cells was utilized.

### **5.2.2 Raman Data Collection**

Raman spectra were obtained using the same Raman instruments that were described earlier. Bacterial Raman spectra were obtained from dense pellets obtained from multiple cultures grown on different days and these spectra were then averaged together to create “average” spectra. The spectra averaged in this way were always 100% representative of the changes being measured. No differences between spectra from bacteria prepared in a specific manner were ever observed. This was confirmed in hundreds of spectra acquired from multiple aliquots. Therefore the averaging of spectra, while not necessary, was a highly-effective way to reduce noise in the Raman spectrum while accentuating real changes in the spectrum. Typically 40-50 spectra from a single quartz slide were averaged. Spectra were acquired from the bacteria prepared in three different ways as described in the materials and methods section: control (non-xylitol exposed), xylitol-exposed (0-2% for 24-30 hours), and post-xylitol exposure (incubated for 24 hour in a xylitol-free medium subsequent to growth in xylitol). To highlight and accentuate differences in the Raman spectra, the differences of the normalized averaged spectra were calculated so that deviations from zero (which would represent no significant change) could

be more easily identified. In all of the Raman studies described here, we did not attempt to directly compare the absolute intensity of Raman signals by varying the bacterial titer. Attempts were made to illuminate approximately equal numbers of cells for all bacterial specimens and species.

Powdered dry xylitol was pressed and compacted to form a flat solid surface and Raman measurements were recorded and used for comparison purposes. In addition, different xylitol concentrated solutions were prepared and tested using Raman spectroscopy.

## 5.3 Results

### 5.3.1 Differential Gram-Staining

The results of the post-xylitol-exposure Gram-staining revealed that xylitol-exposed *S. viridans* behaved differently under differential Gram-staining than the non-exposed control. The xylitol-exposed *S. viridans* populations appeared like Gram-negative or dead bacteria rather than

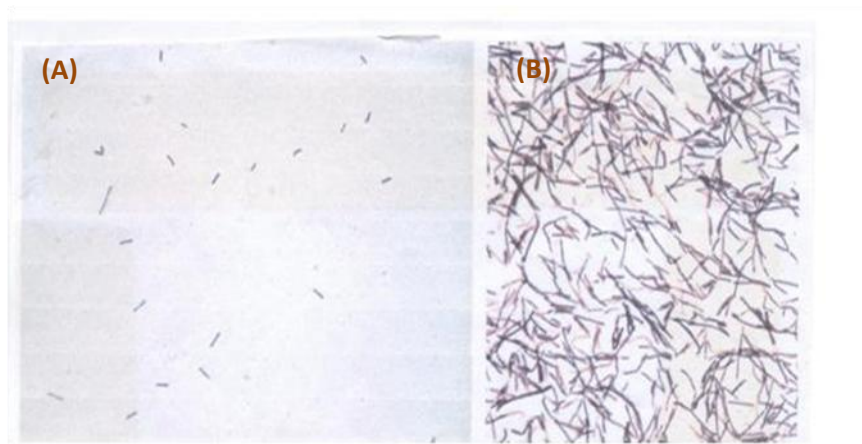
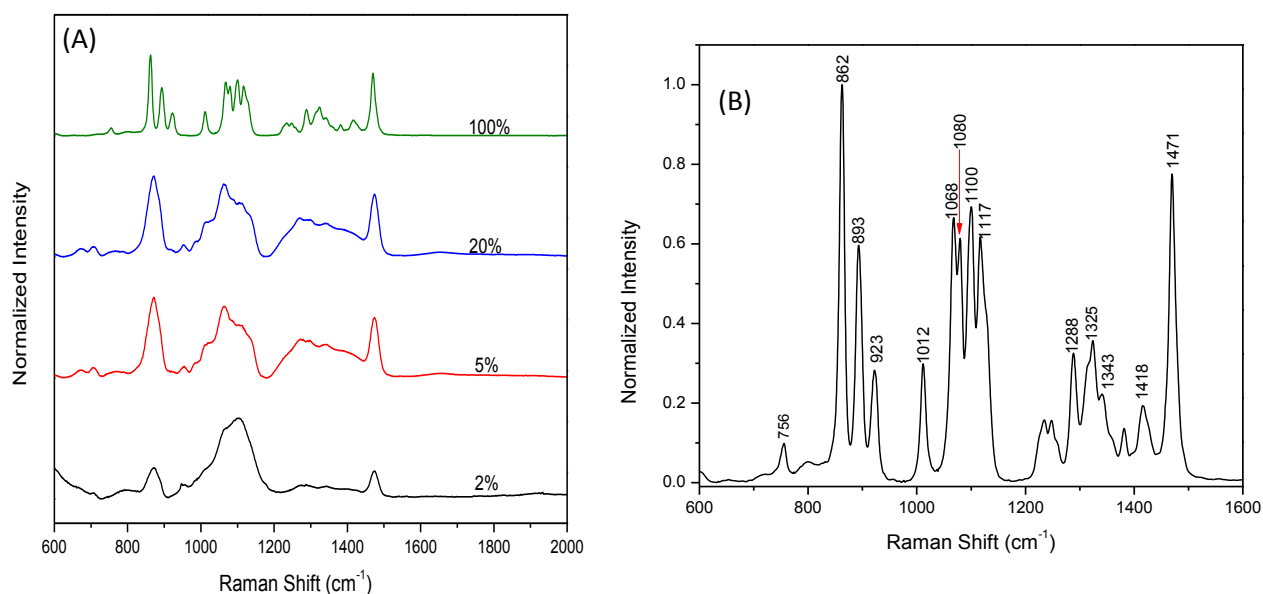


**Figure 5.2:** Action of 2% xylitol on *S. viridans* ultrastructure as revealed by differential Gram-staining imaged with the same magnification. (A): Planktonic cells of *S. viridans* cultured in BHI medium, 0% xylitol, anaerobically for 24 hrs prior to growth in xylitol. The titer has been reduced 10,000 fold to ensure that all bacteria attain log-phase growth in the presence of the xylitol. (B): Gram-stained *S. viridans* bacteria cultured in BHI medium, 2% xylitol, anaerobically for 24 hours. The xylitol-exposed (2% or higher) bacterial population demonstrated a remarkable change; 50% of them stained pink, appearing like Gram-negative or dead bacteria instead of purple.

retaining the crystal violet-iodine complex stain. Figure 5.2(A) shows the low titer of the *S. viridans* population after 10,000-fold dilution prior to growth in xylitol. Figure 5.2(B) shows the effect of the xylitol in the nutrient broth on the *S. viridans* Gram-staining after 24 hours of growth (approximately 13 generations). All *S. viridans* control populations (not exposed to xylitol) stained purple, as expected (not shown). Growth studies of *S. viridans* comparing the colony forming units (cfu) after 24-hours of growth at 37°C under anaerobic conditions in BHI (blood-heart-infusion) medium with and without xylitol confirm the observations of others that xylitol affected the normal growth patterns. Differential Gram-staining showed that xylitol disturbed the retention of the crystal violet in the *S. viridans*. In rich-growth media (BHI or TSB) *S. viridans* appeared normally purple and in a population of diplococci while the xylitol-exposed bacterial population demonstrated a remarkable change; 30-50% of them were in long chains and stained pink (appearing like Gram-negative or dead bacteria) instead of purple diplococci (Fig. 5.2). As our control, after acetone alcohol wash, the Gram-positive bacteria retained the crystal violet-iodine complex (blue or purple), but the Gram-negative organisms usually lose this and the counter stain safranin adds its pink color.

### 5.3.2 Raman Spectroscopy of Xylitol Powder and Solution

Raman spectra from powdered xylitol and different concentrated solution (2%, 5%, and 20%) were obtained in the spectral region 600-2000  $\text{cm}^{-1}$ . Figure 5.3(A) shows a representative spectrum for each case. Raman spectra obtained from low concentration samples (which represents the amount of xylitol that the bacteria were exposed to) showed the main features of xylitol only. The main peaks of powdered xylitol were labeled in Figure 5.3(B) and their assignments are given in table 5.1.



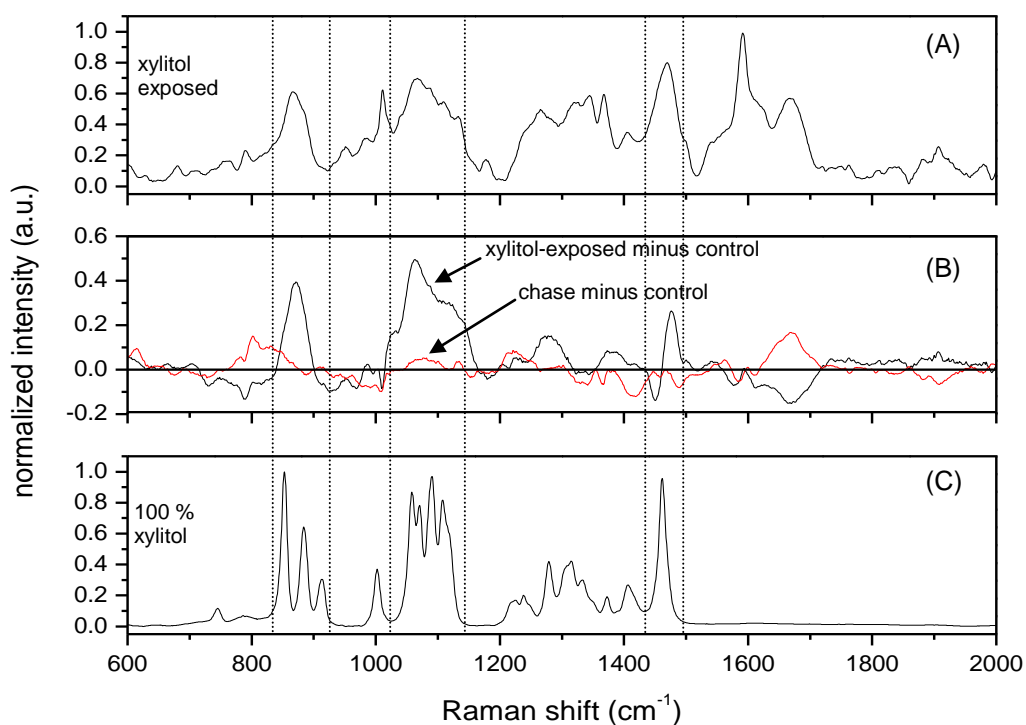
**Figure 5.3:** (A) Raman spectra for different concentrated spots of xylitol, (B) The main peaks of xylitol Raman spectrum.

Table 5.1: The band assignments for the main Raman peaks of 100% xylitol.

Raman Shift (cm <sup>-1</sup> )	Assignments (Vibrational modes)
756	$\nu$ (CO) in Polysaccharides <sup>29</sup>
862	$\nu$ (COC) 1,4-glycosidic link <sup>30</sup> , $\nu$ (CO) <sup>29</sup>
893	CH <sub>2</sub> out-of-plane wag, $\nu$ (CO) <sup>29</sup>
923	$\nu$ (CO) <sup>29</sup> in Disaccharides
1012	Out-of-phase $\nu$ (CCO) <sup>31</sup>
1068	$\delta$ (O-H) <sup>29</sup>
1080	$\delta$ (O-H) <sup>29</sup>
1100	$\nu$ (COC) 1,4-glycosidic link (carbohydrates) <sup>30</sup> , Out-of-phase $\nu$ (CCO) <sup>31</sup>
1117	Out-of-phase $\nu$ (CCO) <sup>31</sup>
1288	$\delta$ (CH <sub>2</sub> ) <sup>30</sup>
1325	$\delta$ (OH), $\delta$ (CH <sub>2</sub> ) <sup>30</sup>
1343	$\delta$ (CH) <sup>32</sup>
1418	$\delta$ (CH <sub>3</sub> ) <sup>30</sup>
1471	$\delta$ (CH <sub>2</sub> ) <sup>25</sup>

### 5.3.3 Raman Spectroscopy of the Uptake of Xylitol by *E. coli* K-12 (xylitol operon-deficient), its Pili- and Flagella-Deficient Derivative *E. coli* JW1881-1, and *E. coli* C (xylitol operon-positive, but in a repressed state)

Raman spectra in the spectral range from 600 to 2000  $\text{cm}^{-1}$  obtained from *E. coli* K-12 which does not possess the xylitol operon are shown in Figure 5.4. Figure 5.4(A) shows the averaged Raman spectrum from the xylitol-exposed *E. coli* K-12. Figure 5.4(B) shows two spectra, one is the difference of the xylitol-exposed and the control *E. coli* K-12 spectra (black) and the other is the difference of the post-exposure chase and the control *E. coli* K-12 spectra



**Figure 5.4:** Raman spectra of *E. coli* K-12 and xylitol. (A) The averaged Raman spectrum from xylitol-exposed *E. coli* K-12. (B) The difference of the xylitol-exposed spectra and the control *E. coli* K-12 (black) and the difference of the post-exposure chase spectra and the control *E. coli* K-12 (red). Deviations from zero denote changes from the control bacteria and are observed strongly in the spectral regions located between the dashed lines in the xylitol-exposed minus control spectra. (C) Raman spectrum from 100% dried, powdered, and compacted xylitol.

(red). Deviations from the zero-line indicate alterations of the Raman spectrum due to xylitol-exposure. Several significant new peaks appear in spectral regions corresponding to strong Raman bands in xylitol (which is shown in Figure 5.4(C) for comparison). Specifically, a new broad Raman feature (not a narrow isolated peak) centered at  $861\text{ cm}^{-1}$  was observed corresponding to the three xylitol Raman bands at  $862$ ,  $893$ , and  $923\text{ cm}^{-1}$ . A second very broad new feature between  $1030$  and  $1140\text{ cm}^{-1}$  was observed in *E. coli* corresponding to the multiple Raman-peak band of xylitol between  $1030$  and  $1140\text{ cm}^{-1}$  and a fairly sharp new feature at  $1470\text{ cm}^{-1}$  was correlated with a very sharp isolated Raman peak in xylitol at  $1471\text{ cm}^{-1}$ . Taken together, we interpret these new features as direct observation of the xylitol molecule in a semi-liquid/liquid environment that allows the xylitol to retain its molecular stoichiometry and structure but significantly reduces signal-to-noise and broadens Raman-active bands. The spectrum in Figure 5.4(C) was obtained from 100% dried, crushed, and powdered xylitol, therefore it was not unexpected that the Raman spectrum from xylitol within the bacterial body would appear significantly altered.

Conversely, the averaged spectrum of the *E. coli* K-12 grown for 24 hours in a xylitol-free medium exhibited no Raman bands which are indicative of the presence of xylitol. These data confirm a passive (unregulated) entry of xylitol into *E. coli* K-12 (black) and a silent exit (red) from the cell without affecting bacterial growth or metabolism. However, we would conclude that the xylitol molecule is quite stable in the growing bacterial cell for the twenty four hours of their growth - the early log phase to the stationary phase. Significantly, the xylitol pool of these bacteria is immediately depleted when they are re-grown in BHI agar medium without xylitol (chase) for approximately ten generations.

The Raman spectra of the *E. coli* C which carries the xylitol operon in a repressed state is shown in Figure 5.5. Comparison of the spectra between 600 to 2000  $\text{cm}^{-1}$  of the *E. coli* C with that of *E. coli* K-12 shows that these two strains of *E. coli* exhibited near-identical behavior both in their uptake of xylitol and in their inability to retain it during post-exposure growth. No significant reproducible differences were observed in the Raman spectra obtained from the *E. coli* K-12 and *E. coli* C strains which thus indicated the passive uptake, stable presence, and passive exit of xylitol without any participation in bacterial metabolism.

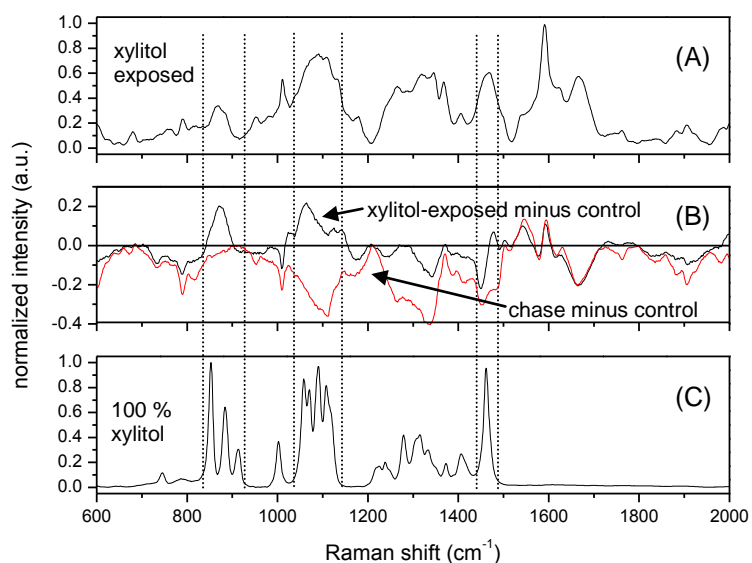


**Figure 5.5:** Raman spectra of *E. coli* C and xylitol. (A) The averaged Raman spectrum from xylitol-exposed *E. coli* C. (B) The difference of the xylitol-exposed spectra and the control *E. coli* C (black) and the difference of the post-exposure chase spectra and the control *E. coli* C (red). Deviations from zero denote changes from the control bacteria and are observed strongly in the spectral regions located between the dashed lines in the xylitol-exposed minus control spectra. (C) Raman spectrum from 100% dried, powdered, and compacted xylitol

Identical experiments were carried out with the pili- and flagella-negative *E. coli* mutant JW 1881-1. The major peaks of xylitol were again observed in the Raman spectra and the intensity of those peaks showed no significant difference from the other strains. The spectra of the JW1881-1 were very similar to that of K-12 and *E. coli* C as shown in Figure 5.6. These data lead us to an important conclusion that the flagella or common pili (motility) apparently play no role either in the passive entry of xylitol into the bacterial cells or in the exit of xylitol from the bacterial pool.

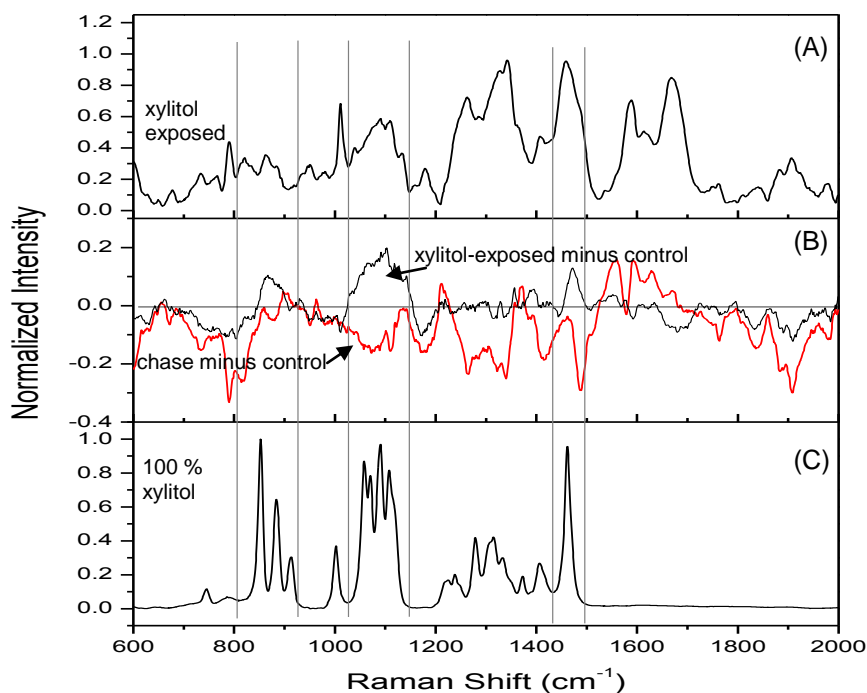


**Figure 5.6:** Raman spectra of *E. coli* JW1881-1 and xylitol. (A) The averaged Raman spectrum from xylitol-exposed *E. coli* JW1881-1. (B) The difference of the xylitol-exposed spectra and the control *E. coli* JW1881-1 (black) and the difference of the post-exposure chase spectra and the control *E. coli* JW1881-1 (red). Deviations from zero denote changes from the control bacteria and are observed strongly in the spectral regions located between the dashed lines in the xylitol-exposed minus control spectra. (C) Raman spectrum from 100% dried, powdered, and compacted xylitol

### 5.3.4 Xylitol-Uptake and Stability in *E. coli* HF4714

Experiments identical to those performed on the other *E. coli* strains were performed on *E. coli* strain HF4714 which contains the de-repressed xylitol operon. The results are shown in Figure 5.7. Contrary to the other *E. coli* strains, the peaks observed in *E. coli* HF4714 due to xylitol did not disappear from the progeny when chased in the absence of xylitol. Specifically the very broad feature between 1030 and 1140  $\text{cm}^{-1}$  was observed in both the xylitol-exposed mother cells and the progeny *E. coli* HF4714 with comparable intensity. This band corresponds to the multiple Raman-peak pattern observed in xylitol between 1030 and 1140  $\text{cm}^{-1}$ . The retention of this Raman feature attributed to xylitol is broadly indicative of the stable accumulation of xylitol in this *E. coli* strain with minimal or no catabolism of the xylitol.

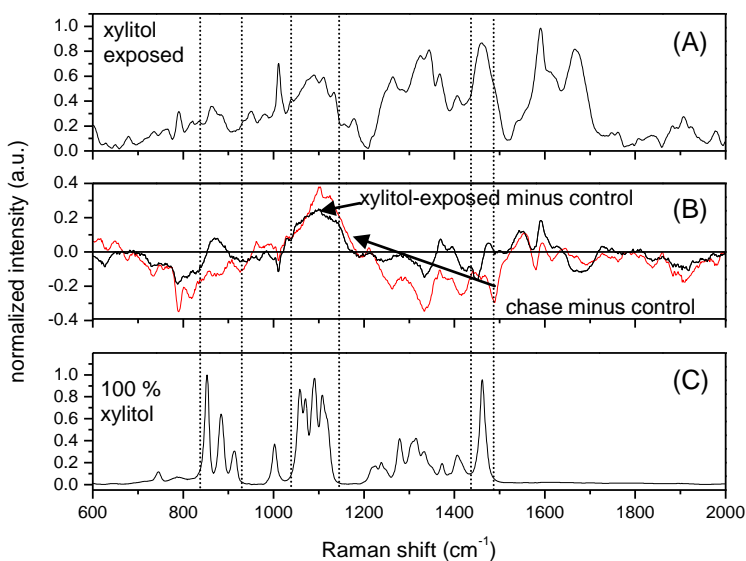


**Figure 5.7:** Raman spectra of *E. coli* HF4714 and xylitol. (A) The averaged Raman spectrum from xylitol-exposed *E. coli* HF4714. (B) The difference of the xylitol-exposed spectra and the control *E. coli* HF4714 (black) and the difference of the post-exposure spectra and the control *E. coli* HF4714 (red). Deviations from zero denote changes from the control bacteria and are observed consistently in the spectral regions located between the dashed lines in the xylitol-exposed minus control spectrum and also in the chase minus control spectrum. (C) Raman spectrum from dried, powdered, and compacted xylitol.

### 5.3.5 Xylitol Metabolism by Gram-Positive *S. viridans*

To characterize the molecular changes responsible for the observed Gram-staining change observed in *S. viridans* as shown in Figure 5.2, Raman spectroscopy was performed on aliquots of the same bacterial samples. Figure 5.8 shows the Raman spectra obtained from the *S. viridans* (control), from the *S. viridans* grown in 2% xylitol for 24 hours, and the same *S. viridans* washed of xylitol and re-grown in BHI-agar medium for an additional 24 hours without xylitol. Comparison of the Raman spectra as presented in Figure 5.7 and Figure 5.8 show that the Raman spectra of the Gram-positive *S. viridans* are completely different from that of the Gram-negative *E. coli*. Two new Raman features are observed in both the xylitol-exposed mother cells and the post-exposure progeny cells. These two new features at  $1165\text{ cm}^{-1}$  and at  $1527\text{ cm}^{-1}$  are not present at all in the xylitol spectrum or the spectrum of the control *S. viridans*

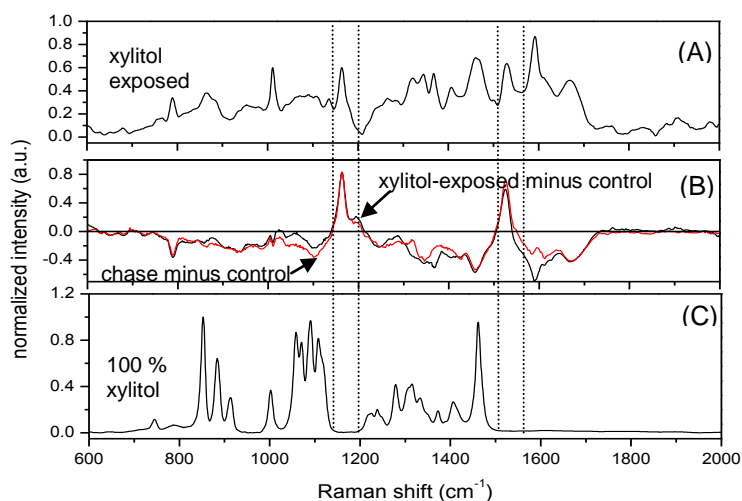


**Figure 5.8:** Raman spectra of *S. viridans* and xylitol. (A) The averaged Raman spectrum from xylitol-exposed *S. viridans*. (B) The difference of the xylitol-exposed spectra and the control *S. viridans* (black) and the difference of the post-exposure spectra and the control *S. viridans* (red). Deviations from zero denote changes from the control bacteria. New Raman peaks not observed at all in xylitol or the control *S. viridans* spectra are observed at  $1165\text{ cm}^{-1}$  and at  $1527\text{ cm}^{-1}$  in both spectra. (C) Raman spectrum from dried, powdered, and compacted xylitol. No xylitol Raman peaks appear in the spectral regions located between the dashed lines.

and could be assigned to a COO stretch vibration in sucrose<sup>31</sup> and a protein NH/CH bend or C=C stretch vibration,<sup>33</sup> respectively. Biochemically, the xylitol is partially metabolized by such *Streptococci* bacteria resulting in insoluble intermediates. Definitive assignment of these peaks at 1165 cm<sup>-1</sup> and at 1527 cm<sup>-1</sup> awaits further study and possibly the chemical purification of these xylitol intermediates and analysis by Raman spectroscopy. Nonetheless, it is apparent that these peaks are evidence of the use of xylitol by the *S. viridans* bacteria. These peaks either originate from smaller sugar by-product molecules resulting from xylitol catabolism or cellular proteins formed as a result of the xylitol catabolism. In future experiments, further growth of *S. viridans* in a medium containing only xylitol as a sole carbon source, (after the complete utilization of dextrose) would confirm the relationship of these peaks at 1165 cm<sup>-1</sup> and at 1527 cm<sup>-1</sup> with xylitol catabolism.

### **5.3.6 The Stability of Xylitol Derivative(s) Formed in Xylitol-Grown *S. viridans* Measured by Raman Spectroscopy**

Raman spectra from 600 to 2000 cm<sup>-1</sup> were acquired from slides of all *S. viridans* specimens prepared as described above. Figure 5.9 shows the Raman spectra from the *S. viridans* cells directly after harvesting from the xylitol-fed bacterial cultures (marked “0 hours”) and collecting the progeny of these bacterial cells after 24 and 72 hours of growth in the xylitol-free TSA solid media. The three spectra have been offset vertically for clarity. Agar media is preferred in order to avoid the lysis of the xylitol derivative borne bacteria population.

Five significant Raman peaks were selected for investigation on the basis of their intensity and what appeared to be changes in their intensities as a function of time. These five peaks were labeled one through five and are identified in Table 5.2. A 10-15 cm<sup>-1</sup> shift in the Raman peak locations was observed between our previous study and this study due to a

recalibration of the linearity of the Raman spectrometer grating scan. Thus the peaks previously identified at 1165 and 1527  $\text{cm}^{-1}$  were measured at 1152 and 1517  $\text{cm}^{-1}$ , respectively, in this study. This is a small wave number shift that is due only to the spectrometer calibration and a careful review of the literature of Raman spectroscopy on bacteria routinely reveals small shifts in the absolute measured wave number on the order of 10  $\text{cm}^{-1}$ . It is the relative location of these peaks which is most important. As well, a visual examination of the spectra leaves no doubts that these broad peaks are definitely the Raman features observed in our earlier study.

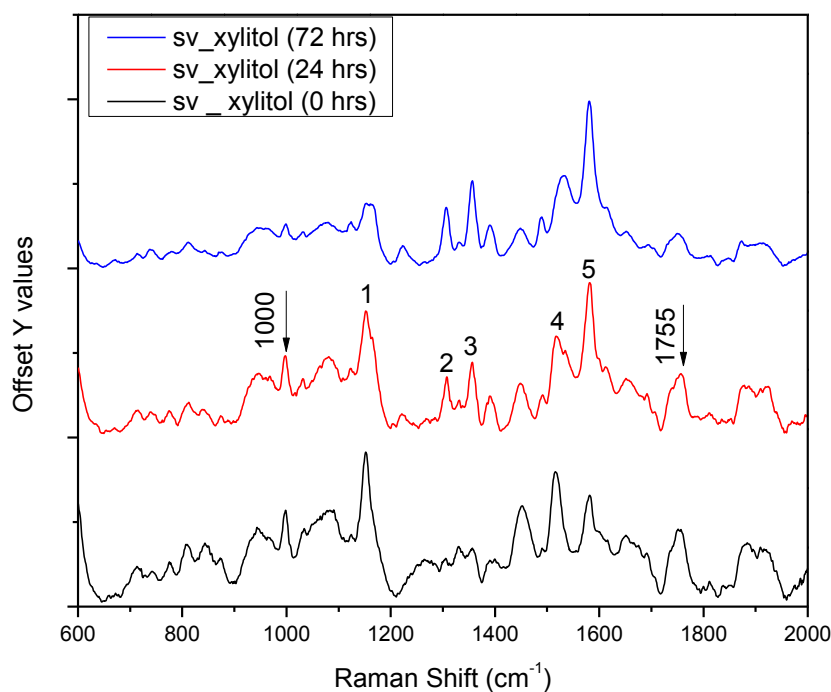


**Figure 5.9:** Raman spectra from the *S. viridans* cells directly after harvesting from the xylitol-fed bacterial cultures (0 hours) and after 24 and 72 hours of growth in the xylitol.

Table 5.2: Assignment of the main Raman vibrational bands observed in *S. viridans* Raman spectra.

Main peaks		Assignments	
Label	Raman shift (cm <sup>-1</sup> )	Vibrational modes	Location
(1)	1152	C-C, C-N stretch <sup>34,35,36</sup>	Protein
(2)	1305	CH <sub>2</sub> twist in lipids <sup>36,37</sup>	Lipid
(3)	1356	C-H bend <sup>38</sup>	Protein
(4)	1517	$\nu(\text{C}=\text{C})$ <sup>35</sup>	Protein
(5)	1582	$\nu(\text{C}=\text{C})$ <sup>38</sup> , Nucleic acids (G,A) <sup>36</sup>	Lipid, DNA/RNA

Two smaller, but more constant peaks were selected for normalization of the five peaks under study. Absolute Raman intensity measurements are often difficult to make, so to determine whether the peaks in each spectrum were increasing or decreasing in intensity as a function of time, the intensity of the five peaks relative to the smaller but constant normalization peaks was calculated. Figure 5.10(A) shows the intensity of the five peaks relative to a normalization peak at 1000 cm<sup>-1</sup> and 5.10(B) shows the intensities relative to a normalization peak at 1755 cm<sup>-1</sup>. Use of either normalization peak yielded the same changes from 0 to 72 hours: a strong increase was observed in the peak 1582 cm<sup>-1</sup>; no statistically significant change was observed in the peak at 1152 cm<sup>-1</sup>; and small increases in the peak intensities at 1305, 1356, and 1517 cm<sup>-1</sup> were observed.

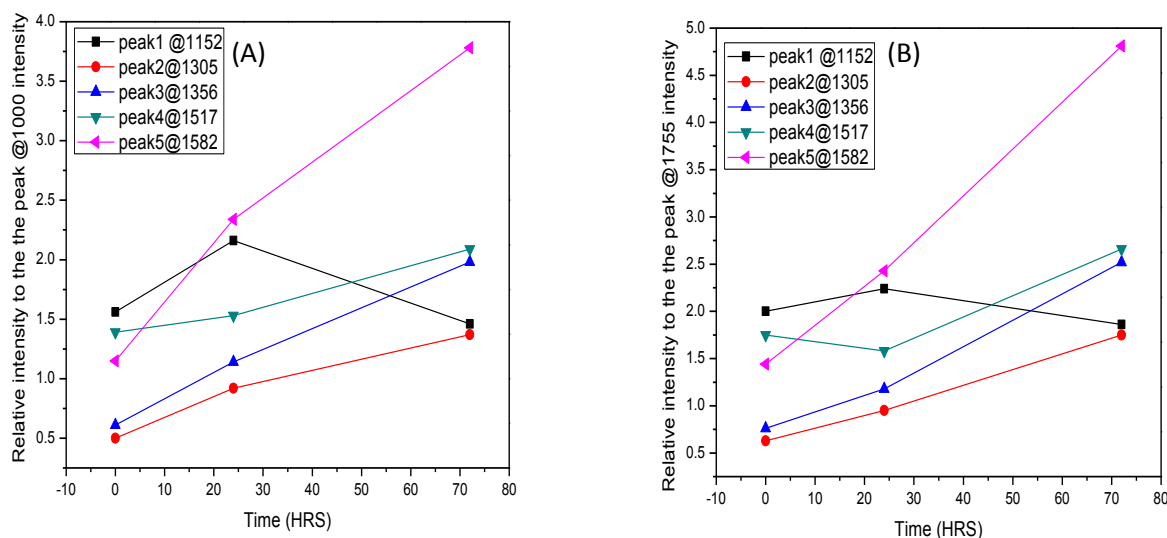


**Figure 5.10:** The intensity of the five labeled peaks as a function of time relative to a normalization peak at  $1000\text{ cm}^{-1}$  (A), and relative to a normalization peak at  $1775\text{ cm}^{-1}$  (B).

To insure that these observed spectral increases were due to the prior growth in xylitol and the presence of the xylitol time bomb, the same analysis was performed on xylitol-free bacterial colonies harvested from the TSA growth medium at 24, 48, and 72 hours (Figure 5.11). Figure 5.12 shows the intensity of the five important peaks relative to the two normalization peaks. Due to the weakness of the peak at  $1755\text{ cm}^{-1}$ , as can be seen in Figure 5.11, a new normalization peak at  $1392\text{ cm}^{-1}$  was utilized. It can be seen that the peak at  $1582\text{ cm}^{-1}$  again experienced some growth over the course of 72 hours incubation on the TSA; but its increase was not as significant as in the xylitol-exposed cultures. All other peaks demonstrated no statistically significant change.

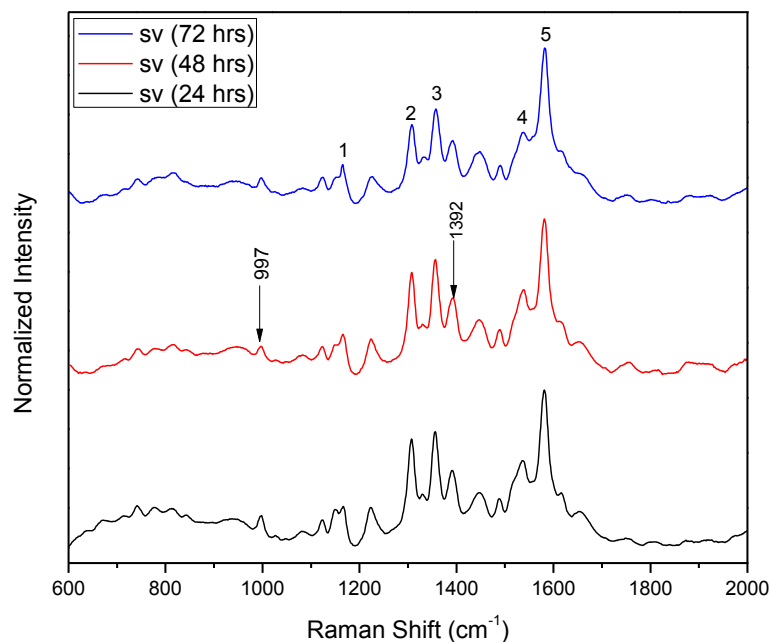


**Figure 5.11:** Raman spectra from the *S. viridans* cells harvested from the TSA growth media at 24, 48, and 72 hours.

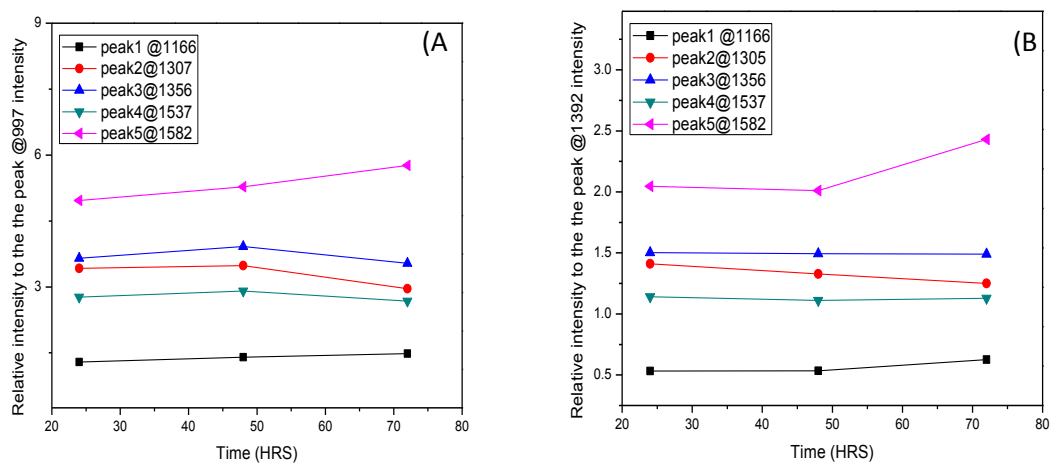


**Figure 5.12:** The intensity of the labeled five peaks as a function of time (A) relative to a normalization peak at  $997\text{ cm}^{-1}$ , (B) relative to a normalization peak at  $1392\text{ cm}^{-1}$ .

## 5.4 Discussion

I have compared the uptake of xylitol by four genetically well defined strains of *E. coli*: *E. coli* K-12, its pili- and flagella-deficient derivative JW1881-1, *E. coli* C and an *E. coli* C derivative HF4714 as well as a Gram-positive strain of *Streptococcus viridans* (ATCC 19950). It is known that the *E. coli* C contains a xylitol operon in a repressed state apparently to avoid the disadvantages of a constitutive catabolic pathway (toxicity to galactitol and arabitol). What is more, the flagella and pili responsible for motility are conspicuously absent on the surface of the *E. coli* C as compared to *E. coli* HF4714 when visualized by scanning electron microscopy. Thus the *E. coli* C may have avoided a fatal pathway to chemo-attraction but this is not a very unusual occurrence in an aquatic environment. These *E. coli* strains show comparable levels of xylitol uptake, despite their genetic differences.

Significantly, the *E. coli* HF4714 which contains the xylitol operon in a de-repressed state is capable of xylitol metabolism whenever the other carbon sources are exhausted. The preferred carbon source, dextrose in BHI-agar growth medium, is first utilized before the metabolic use of xylitol begins. These experiments were conducted with a BHI medium containing a minimal amount of dextrose and 2% xylitol. Because of the availability of dextrose, the HF4714 may have developed a metabolic imbalance resulting in an accumulation of xylitol that far exceeds the rate of its utilization (Fig. 5.7). After growth in BHI-agar medium for two days, the *E. coli* C and *E. coli* K-12 stopped growing as evidenced by the colony size and bacterial titer, while the colonies of the HF4714 continued increasing in size.

In a similar manner, the *S. viridans* which has an incomplete metabolic pathway of xylitol is not capable of growing into larger colonies in the presence of 2% xylitol. The Gram-staining of these colonies picked up from CNA or BHI-agar plates with 2% xylitol demonstrates the

elongated shapes or the diplococcic bacteria in chains, an index of abnormality in bacterial septum formation or abnormality during stages of cell division or cytokinesis (Figure 5.2).

#### **5.4.1 Anti-Adhesion Effects of Xylitol**

It is known that pneumonia claims a considerable number of deaths worldwide in the very young and the elderly, especially given the rise of antibiotic- and/or immuno-resistant organisms.<sup>39</sup> Billions of dollars are spent annually to treat these diseases, usually with antibiotics and surgical intervention, but the rise of bacterial resistance to conventional drugs has become a serious problem in infection control. It seems logical to determine the efficacy of xylitol alone or in combination with other agents, such as fluoride, on such drug resistant pathogens. My data support the work of others that it could be the anti-adherence effect of nasally administered xylitol which might lead to a significant reduction in the occurrence of AOM and pneumonia in children.<sup>40</sup>

Alteration of surface structures after exposure to xylitol and a lessening of the bacterial adhesion to both biotic and abiotic surfaces have been reported<sup>41,13,42</sup> as has a lessening of the bacterial adhesion of *E. coli* to uroepithelial cells subsequent to cranberry juice exposure<sup>43</sup> and could probably minimize persistent urinary tract infections. Significantly, it has been reported that xylitol can damage the ultrastructure of pneumococci, when compared to the effect of fructose or sucrose.<sup>44</sup> Xylitol is a 5-carbon sugar and the Gram-positive diplococci are permeable to xylitol except there seems to be an antagonistic competition between fructose and xylitol<sup>45</sup> at the initial stages of biochemical pathways. The molecular basis of such competition has not been properly investigated although surface ultrastructure modification is indicated.

The observations of surface ultrastructure modification and reduction in adhesion are intriguing. The majority of the Gram-negative bacteria have grown flagella and pili (or fimbriae) emerging out of the cell envelope but our data show that the presence of these fimbriae does not seem to affect xylitol uptake. It remains to be seen if an adhesion change is measurable in xylitol-exposed pathogens and if this adhesion change is pili-motivated.<sup>46,47,48,49</sup>

The change in adhesion of 2% xylitol-exposed *S. viridans* to abiotic surfaces was studied in our department utilizing atomic force microscopy (AFM). These experiments were conducted by Dr. Michael Giangrande in the laboratory of Professor Peter Hoffmann.

The results revealed a clear reduction in adherence to the abiotic AFM tip, probably caused by ultrastructure changes,. The average force of adherence between the AFM tip and a single non-xylitol-exposed bacterial cell is approximately 80 pN. The average force of adherence between the AFM tip and the xylitol-exposed *S. viridans* was measured to be approximate 35 pN in one set of measurements, and 38 pN in the second set of measurements. This reveals an approximately 50% reduction in the measured adherence force of xylitol-exposed Streptococci relative to the non-xylitol-exposed control. We hope to correlate the appearance of the new Raman molecular peaks observed in Figure 5.8 with an alteration of surface ultrastructures responsible for adhesion changes. It may also be possible to visualize such ultrastructure modification via AFM or STM.

The second set of experiments confirms that the xylitol remains relatively stable in *Streptococci viridans* and interferes in bacterial cell division. The results showed that the compounds formed in the Streptococci are the xylitol derivatives since they are only seen in the

bacteria with functional xylitol operons when they are grown for many generations in the TSA medium containing 2% xylitol.

#### **5.4.2 Bacterial Morphology and Physiology and Their Importance to Xylitol Treatment**

A remarkable coincidence is that the pathogens interacting with xylitol are all morphologically diplococcal organisms, regardless of their Gram-staining classification.<sup>8</sup> All possible structures of bacteria are well-characterized, but their specific interactions with different sugar and sugar-alcohol molecules have not been considered. I believe that the morphological shapes of these bacteria may play a critical role in their effective interactions with specific structures of sugar molecules (five-carbon, six-carbon, or sugar alcohols) and subsequent uptake. Since Gram-positive *S. pneumoniae* cross-reacts with the capsular Gram-negative *Klebsiella pneumoniae* and both are morphologically diplococcal, the xylitol seems to be equally accessible to these pathogens. In this work, the Gram positive pathogen *S. viridans* are not fully capable of metabolizing the five-carbon sugar alcohol xylitol, but intermediate chemical compounds are formed and continue to exist in the bacterial metabolic pool. Such presence may adversely affect the thickness of peptidoglycan walls of bacteria. This in turn probably weakens the stable stacking of crystal violet (CV) and therefore a confusion may arise in the identification of Gram-positive bacteria by Gram-staining.<sup>50</sup> Our data as shown in Figure 5.1, if proven, may challenge the century-old method of Gram-stain classification when the thickness of the Gram-positive cell wall is affected by xylitol or other adverse growth conditions.

#### **5.4.3 Fluoride and Xylitol**

It is already known that the use of 1 ppm fluoride is effective in minimizing dental decay.<sup>51</sup> Furthermore, the simultaneous application of xylitol and fluoride produces a synergistic effect, but the precise mechanism of synergism is unknown.<sup>52</sup> Analyses of intracellular

glycolytic intermediates have shown that the fluoride inhibits the lower part of the glycolytic pathway and that xylitol affects the upper pathway. It is not known if fluoride affects the biofilm formation and or the growth of diplococci in chains. Reversion of chains into single diplococci populations may allow a higher percentage of the bacterial population (or their receptors) to effectively interact with the xylitol molecules. Thus the probability of success of the preventive therapy would highly increase and save many young lives. This would provide us a molecular basis for the successful use of the synergistic approach towards a preventative therapy.

## 5.5 Summary

Visible wavelength Raman spectroscopy was used to investigate the uptake and metabolism and the stability of the five-carbon sugar alcohol xylitol by a Gram-positive *Streptococcus viridans* and the two extensively used strains of Gram-negative *Escherichia coli*, *E. coli* C and *E. coli* K-12. The *E. coli* C, but not the *E. coli* K-12, contains a complete xylitol operon, and the *Streptococci viridans* contains an incomplete xylitol operon used to metabolize the xylitol. Raman spectra from xylitol-exposed *S. viridans* exhibited significant changes that persisted even in progeny grown from the xylitol-exposed mother cells in a xylitol-free medium for 24 hours. This behavior was not observed in the *E. coli* K-12. In both *S. viridans* and the *E. coli* C derivative HF4714, the metabolic intermediates are stably formed to create an anomaly in bacterial normal survival. The uptake of xylitol by Gram-positive and Gram-negative pathogens occurs even in the presence of other high-calorie sugars and its stable integration within the bacterial cell wall may discontinue bacterial multiplication. This could be a contributing factor for the known efficacy of xylitol when taken as a prophylactic measure to prevent or reduce occurrences of persistent infection. Specifically, these bacteria are causative agents for several important diseases of children like pneumonia, otitis media, meningitis, and dental caries. If

properly explored, such an inexpensive and harmless sugar-alcohol, alone or used in conjunction with fluoride, would pave the way to an alternative preventive therapy for these childhood diseases when the causative pathogens have become resistant to modern medicines like antibiotics and vaccine immunotherapy.

## CHAPTER 5 REFERENCES

- <sup>1</sup> T.Kontiokari, M. Uhari and M. Kosela. "Effect of xylitol on growth of nasopharyngeal bacteria in vitro," *Antimicrobial Agents and Chemotherapy* **39**:1820-1823 (1995).
- <sup>2</sup> L. Trahan. "Xylitol: A review of its actions on Mutans Streptococci and dental plaque. Its clinical significance," *International Dental Journal* **45**:77-92 (1995).
- <sup>3</sup> M. Uhari, T. Tapiainen, and T. Kontiokari. "Xylitol in preventing acute otitis media," *Vaccine* **19**:S144-S147 (2000).
- <sup>4</sup> T. Tapiainen. *Microbiological effects and clinical uses of xylitol in preventing acute otitis media*, Ph.D. thesis, University of Oulu, Oulu, Finland (2002).
- <sup>5</sup> E. Söderling, T. Ekman and T. Taipale. "Growth inhibition of Streptococcus mutans with low xylitol concentrations," *Current Microbiology* **56**:382-385 (2008).
- <sup>6</sup> K. Mäkinen, P. Alanen, P. Isokangas, K. Isotupa, E. Söderling, P.-L. Mäkinen, W. Wenhui, W. Weijian, C. Xiaohi, W. Yi, and Z. Boxue. "Thirty-nine month xylitol chewing gum program in initially 8 year old school children: a feasibility study focusing on mutans streptococci and lactobacilli," *International Dental Journal* **58**:41-50 (2008).
- <sup>7</sup> E. Honkala, S. Honkala, M. Shyama, and S.A. Al-Mutawa. "Field trial on caries prevention with xylitol candies among disabled school students," *Caries Research* **40**:508-513 (2006).
- <sup>8</sup> A.A. Salyers and D.D. Whitt. *Bacterial pathogenesis, a molecular approach*, 2<sup>nd</sup> Ed., ASM Press, Washington DC (2002).
- <sup>9</sup> S. Yokota, A. Harimaya, and K. Sato. "Colonization and turnover of *S. pneumonia*, *Haemophilus influenza*, and *Moraxella catarrhalis* in otitis-prone children," *Microbiology and Immunology* **51**:223-230 (2007).
- <sup>10</sup> M. Gladwin and B. Trattler. *Clinical Microbiology*, 4<sup>th</sup> ed. MedMaster, Miami (2008).

- <sup>11</sup> C. Vadeboncoeur and M. Pelletier. “The phosphoenolpyruvate: sugar phosphotransferase system of oral streptococci and its role in the control of sugar metabolism,” *FEMS Microbiology Reviews* **19**:187–207 (1997).
- <sup>12</sup> L. Trahan, M. Bareil, L. Gauthier, and C. Vadeboncoeur. “Transport and phosphorylation of xylitol by a fructose phosphotransferase system in *Streptococcus mutans*,” *Caries Research* **19**:53–63 (1985).
- <sup>13</sup> T. Kontiokari, M. Uhari, and M. Koskela. “Antiadhesive effects of xylitol on otopathogenic bacteria”, *Journal of Antimicrobial Chemotherapy* **41**:563-565 (1998).
- <sup>14</sup> E. Söderling, L. Alaräisänen, A. Scheinin, and K.K. Mäkinen. “Effect of xylitol and sorbitol on polysaccharide production by and adhesive properties of *Streptococcus mutans*,” *Caries Research* **21**:109-116 (1987).
- <sup>15</sup> H. Tuompo, J.H. Meurman, K. Lounatmaa, and J. Linkola. “Effect of xylitol and other carbon sources on the cell wall of *Streptococcus mutans*”, *Scandinavian Journal of Dental Research* **91**:17-25 (1983).
- <sup>16</sup>W.T. Charnetzky and R.P. Mortlock. “Close genetic linkage of the determinants of the ribitol and D-arabitol catabolic pathways in *Klebsiella aerogenes*,” *Journal of Bacteriology* **119**:176-182 (1974).
- <sup>17</sup> J.S. Brimacombe and J.M. Webber. *Alditols and derivatives*, p. 479-519. In W. Pigman and D. Horto (ed.), *The Carbohydrates*, Vol IA, 2<sup>nd</sup> ed. Academic Press, London 1972.
- <sup>18</sup> K. Hattori and T. Suzuki. “Microbial Production of D-arabitol by n-alkane-grown *Candida tropicalis*,” *Agricultural Biology and Chemistry* **38**:1203–1208 (1974).
- <sup>19</sup> E.J. Saint Martin and R.P. Mortlock. “Natural and altered induction of the L-fructose catabolic enzymes in *Klebsiella aerogenes*,” *Journal of Bacteriology* **127**:91-97 (1976).
- <sup>20</sup> W.A. Wood. “Ribitol and D-arabitol utilization by *Aerobacter aerogenes*,” *Journal of Biological Chemistry* **236**:2190-2195 (1961).
- <sup>21</sup> A.M. Reiner. “Genes for Ribitol and D-arabitol catabolism in *E. coli*: their loci in C strains and absence in K-12 and B strains,” *Journal of Bacteriology* **123**:530-536 (1975).

- <sup>22</sup> G.A. Scangos and A. M. Reiner. "Ribitol and D-arabitol catabolism in *E. Coli*," Journal of Bacteriology **134**:492-500 (1978).
- <sup>23</sup> R.P. Mortlock. "Catabolism of unnatural carbohydrates by micro-organisms," Advances in Microbial Physiology **13**:1-53 (1976).
- <sup>24</sup> M.K. Waldor, D.I. Friedman, and S.L. Adhya (ed.). *Phages, their role in bacterial pathogenesis and biotechnology*, ASM Press, Washington DC (2005).
- <sup>25</sup> K. Maquelin, C. Kirschner, L.-P. Choo-Smith, N. Van den Braak, H. Ph. Endtz, D. Naumann, and G.J. Puppels. "Identification of medically relevant microorganisms by vibrational spectroscopy," Journal of Microbiological Methods **51**:255-271 (2002)
- <sup>26</sup> M. Navratil, G.A. Mabbott, and E.A. Arriaga. "Chemical microscopy applied to biological systems," Analytical Chemistry **78**:4005-4019 (2006).
- <sup>27</sup> R.J. Lamont, M. Meila, Q. Xia, and M. Hackett. Mass spectrometry-based proteomics and its application to studies of *Porphyromonas gingivalis* invasion and pathogenicity," Infectious Disorders – Drug Targets. **6**:311-325 (2006).
- <sup>28</sup> P.R. Murray, W.L. Drew, G.S. Kobayashi, and J.H. Thompson. *Medical Microbiology*, CV Mosby Company, St. Louis (1990).
- <sup>29</sup> D. Lin-Vein, N. B. Colthup, W.G. Fatety, J.G. Grasselli, *The Handbook of INFRARED and Raman Characteristic Frequencies of Organic Molecules*, Academic press, London, (1991).
- <sup>30</sup> A.C. Williams and H.G.M. Edwards. "Fourier transform Raman spectroscopy of bacterial cell walls," Journal of Raman Spectroscopy **25**:673-677 (1994).
- <sup>31</sup> M. Veij, P. Vandenabeela, T. De Beer, J. Remon, and L. Moens, "Reference database of Raman spectra of pharmaceutical excipients," Journal of Raman Spectroscopy **40**: 297-307 (2009).
- <sup>32</sup> L.J. Goeller and M. R. Riley. "Discrimination of bacteria and bacteriophages by Raman spectroscopy and surface-enhanced Raman spectroscopy", Applied Spectroscopy **61**:679-685 (2007).

- <sup>33</sup> A. Sengupta, M. L. Laucks, and E. J. Davis. "Surface-enhanced Raman spectroscopy of bacteria and pollen," *Applied Spectroscopy* **59**:1016-1023 (2005).
- <sup>34</sup> W.F. Howard, JR., W.H. Nelson, and J.F. Sperry. "A resonance Raman method for the rapid detection and identification of bacteria in water,": *Applied Spectroscopy* **34**:72-75 (1980).
- <sup>35</sup> R.A. Dalterio, M. Baek, W.H. Nelson, D. Britt, J.F. Sperry, and F.J. Purcell. "The resonance Raman microprobe detection of single bacterial cells from a chromobacterial mixture," *Applied Spectroscopy* **41**:241-244 (1987).
- <sup>36</sup> I. Notingher. "Raman spectroscopy cell-based biosensors," *Sensors* **7**:1343-1358 (2007).
- <sup>37</sup> L.J. Goeller and M.R. Riley. "Discrimination of bacteria and bacteriophages by Raman spectroscopy and surface-enhanced Raman spectroscopy," *Applied Spectroscopy* **61**:679-685 (2007).
- <sup>38</sup> M.L. Laucks, A. Sengupta, K. Junge, E J. Davis, and B.D. Swanson. "Comparison of psychro-active arctic marine bacteria and common mesophilic bacteria using surface-enhanced Raman spectroscopy," *Applied Spectroscopy* **59**:1222-1228 (2005).
- <sup>39</sup> O.S. Levine, K. L. O'Brien, M. Knoll, R. A. Adegbola, S. Black, T. Cherian, R. Dagan, D. Goldblatt, A. Grange, B. Greenwood, T. Hennessy, K. P. Klugman, S. A. Madhi, K. Mulholland, H. Nohynek, M. Santosham, S. K. Saha, J. A. Scott, S. Sow, C. G. Whitney, and F. Cutts. "Pneumococcal vaccination in developing countries," *Lancet* **367**:1880-1882 (2006).
- <sup>40</sup> A. Jones. "The next step in infectious disease: taming bacteria," *Medical Hypotheses* **60**:171-174 (2003).
- <sup>41</sup> P. Naaber, E. Lehto, S. Salminen and M. Mikelsaar. "Inhibition of adhesion of *Clostridium difficile* to Caco-2 cells," *FEMS Immunology and Medical Microbiology* **14**:205-209 (1996).
- <sup>42</sup> A. Modesto and D. Drake. "Multiple exposures to chlorhexadine and xylitol; adhesion and biofilm formation by *Streptococcus mutans*," *Current Microbiology* **52**:418-423 (2006).
- <sup>43</sup> P.A. Pinzón-Arango, Y. Liu, and T. A. Camesano. "Role of cranberry on bacterial adhesion forces and implications for *Escherichia coli*-uroepithelial cell attachment," *Journal of Medicinal Food* **12**:1-12 (2009).

- <sup>44</sup> T. Tapiainen, R. Sormunen, T. Karjalainen, T. Kontiokari, I. Ikaheimo, and M. Uhari. "Ultrastructure of *Streptococcus pneumoniae* after exposure to xylitol," *Journal of Antimicrobial Chemotherapy* **54**:225-228 (2004).
- <sup>45</sup> T. Tapiainen, T. Kontiokari, L. Sammalkivi, I. Ikaheimo, M. Koskela, and M. Uhari. "Effect of xylitol on growth of the *Streptococcus pneumoniae* in the presence of fructose and sorbitol," *Antimicrobial Agents and Chemotherapy* **45**:166-169 (2001).
- <sup>46</sup> J.R. Scott and D. Zahner. "Pili with strong attachments: Gram-positive bacteria do it differently," *Molecular Microbiology* **62**:320-330 (2006).
- <sup>47</sup> J.L. Telford, M.A. Barocchi, I. Margarit, R. Rappuoli, and G. Grandi. "Pili in Gram-positive pathogens," *Nature Reviews Microbiology* **4**:509-519 (2006).
- <sup>48</sup> J. Mattick. "Type IV pili and twitching motility," *Annual Review of Microbiology* **56**:289-314 (2002).
- <sup>49</sup> L.S. Dorobantu, S. Bhattacharjee, J.M. Foght, and M.R. Gray. "Analysis of force interactions between AFM tips and hydrophobic bacteria using DLVO theory," *Langmuir* **25**:6968-6976 (2009).
- <sup>50</sup> H.J. Rogers, H.R. Perkins, and J.B. Ward. *Microbial cell walls and membranes*, Chapman and Hall, New York (1980).
- <sup>51</sup> E. Honkala, S. Honkala, M. Shyama, and S.A. Al-Mutawa. "Field trial on caries prevention with xylitol candies among disabled school students," *Caries Research* **40**:508-513 (2006).
- <sup>52</sup> H. Maehara, Y. Iwami, H. Mayanagi, and N. Takahashi. "Synergistic inhibition by combinations of fluoride and xylitol on glycolysis of Mutans Streptococci and its biochemical mechanism," *Caries Research* **34**:231-234 (2005).

## Chapter 6

# The Effect of Wag31 Phosphorylation on the Cells and the Cell Envelope Fraction of Wild-Type and Conditional Mutants of *Mycobacterium Smegmatis* Studied in Vivo by Visible-Wavelength Raman Spectroscopy

### 6.1 Introduction

Tuberculosis (TB) is a worldwide health problem with a high mortality, infecting one out of every three people globally.<sup>1</sup> Latency, which creates a reservoir of persons with the potential to develop active tuberculosis, is especially important in the epidemiology and pathogenicity of tuberculosis. Despite its importance, it is still not clear how *M. tuberculosis* controls the latent state in a human host.<sup>2</sup> However, to achieve, maintain, or escape from the latent state, *M. tuberculosis* must carefully regulate cell division, requiring a wide variety of signaling molecules.

Two protein kinases, PknA and PknB, are thought to be essential for signal transduction in this microorganism and have been shown to play an important role in regulating cell morphology and cell division.<sup>3,4,5,6,7</sup> Wag31, a substrate of PknA and PknB, is a homolog of the Gram-positive cell division protein DivIVA that is localized in the cell poles in mycobacteria including *M. smegmatis* and *M. bovis* BCG and controls cell morphology.<sup>8,9,10</sup>

The phosphorylation of Wag31 plays a key role in the cell division of mycobacterium. It has previously been shown that the expression of phosphomimetic *M. tuberculosis wag31* (*wag31T73E<sub>Mtb</sub>*) in the *wag31* conditional mutant of *M. smegmatis* showed higher growth rate

than cells expressing wild-type *wag31*<sub>Mtb</sub> or phosphoablative *wag31T73A*<sub>Mtb</sub> and that the phosphorylation of Wag31 regulates *M. smegmatis* peptidoglycan biosynthesis and growth of mycobacteria.<sup>10,11</sup>

In this study, I attempt to quantify molecular differences in the three *wag31* conditional mutants of *M. smegmatis* in vivo by using the visible-wavelength Raman spectroscopy apparatus. I also attempted to localize these molecular changes in the cell by performing experiments on the P60 cell envelope fraction of these cells.

## 6.2 Materials and Methods

### 6.2.1 Microorganisms and Growth Conditions

*M. smegmatis* conditional mutant strains of *wag31* containing tetracycline-inducible P<sub>tet</sub>-*wag31*, P<sub>tet</sub>-*wag31T73A* or P<sub>tet</sub>-*wag31T73E* at the *attB* locus were used in our study.<sup>12,13</sup> All cells were prepared in the laboratory of Dr. Choong-Min Kang (WSU, Department of Biological Sciences) with the kind assistance of Charul Jani. Cells were grown on 7H9-ADC agar plates containing 5 ng/ml tetracycline and 50 mg/ml hygromycin. Well-isolated colonies from the plate were then inoculated in 7H9 liquid medium with 10 µg/ml hygromycin without inducer (tetracycline) and cultured overnight to deplete the residual cytosolic inducer and Wag31 inside the cells. Cells from overnight culture were then reinoculated in fresh 7H9-ADC liquid medium supplemented with 20 ng/ml tetracycline as an inducer followed by OD<sub>600</sub> measurement every 3 hours. *M. smegmatis* cells expressing *wag31WT*, *wag31T73A* and *wag31T73E* were harvested during log phase and cell pellets were washed once with 1X phosphate buffer (137 mM NaCl, 2.7 mM KCl and 11.9 mM phosphates) to remove traces of the media.

### 6.2.2 Cell Envelope Isolation

The cell envelope fraction (P60) was prepared as described in detail previously.<sup>14</sup> Briefly, the harvested cells with *wag31T73A* and *wag31T73E* allele were stored at -80°C, then 8 g of harvested cells were resuspended in 30 ml of buffer A (50 mM MOPS (pH 8.0), 10 mM MgCl<sub>2</sub>, and 5 mM β-mercaptoethanol) and subjected to probe sonication using 10 cycles of 60 sec with 90 sec cooling on ice between the cycles. The cell lysates were centrifuged at 23,000 X g (Beckman, JLA10.500) at 4°C for 30 min. then the pellet was resuspended in buffer A and Percoll (GE Healthcare) was added to achieve a 60% final concentration. The resulting mixture was centrifuged at 23,000 X g for 60 min at 4°C. The upper, flocculent band was recovered and washed with buffer A three times to remove residual Percoll. The pellet containing membranes and cell wall was then resuspended in buffer A using a Dounce homogenizer. The final concentrations of total protein from cells expressing *wag31T73E* and *wag31T73A* were 10 and 8 mg/ml, respectively.

Raman measurements were performed on dried spots of cells and cell envelopes using the same Raman system described previously. As mentioned earlier the data were processed using a Matlab program<sup>15</sup> and analyzed using the multivariate techniques of PCA, which reduced the dimensionality of the spectra from 1993 channels into 13 PCs, and DFA, which uses the PCs to discriminate between the different groups of bacteria.

## 6.3 Results and Discussion

### 6.3.1 Raman Spectra from Bacteria Cells

To insure the reproducibility of the Raman spectra, approximately 100 spectra of each *M. smegmatis* mutant were obtained from suspensions of several cultures prepared over several

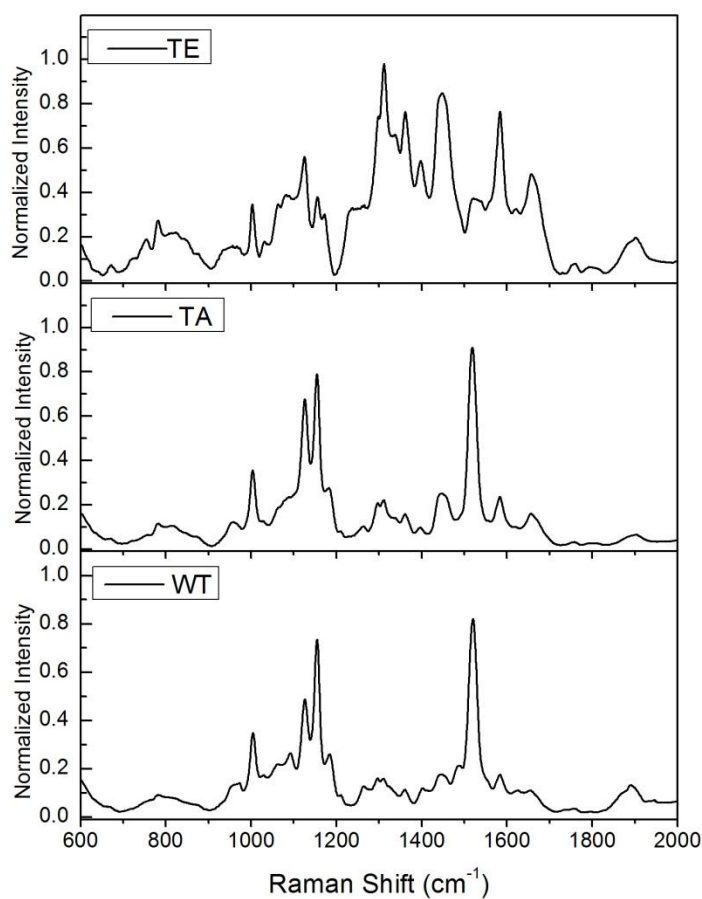


**Figure 6.1:** Typical Raman spectra of *M. smegmatis* expressing phosphomimetic *M. tuberculosis* *wag31* (*wag31T73E<sub>Mtb</sub>*) (TE), wild-type *wag31<sub>Mtb</sub>* (WT), or phosphoablative *wag31T73A<sub>Mtb</sub>* (TA). Spectra were acquired in vivo with 514.5 nm laser excitation.

weeks. Figure 6.1 shows the average of the processed Raman spectra from cells expressing *wag31WT* (WT), *wag31T73A* (TA), and *wag31T73E* (TE). The spectra obtained from WT cells and TA cells are reproducibly similar while there are considerable differences between them and the spectra obtained from TE cells. The observed features in the Raman spectra reveal the composition of the bacterial cell namely protein, carbohydrates, lipid, and nucleic acids. The major peaks and their assignments are listed in Table 6.1. WT and TA spectra have significantly stronger protein peaks at  $1518\text{ cm}^{-1}$  and at  $1154\text{ cm}^{-1}$ , which have the assignment of carbon-carbon double-bond and single bond stretching mode vibration. TE has significant features at  $1310$ ,  $1361$ , and  $1396\text{ cm}^{-1}$  which have previously been attributed to D-glutamic acid, D-alanine, and *N*-acetylglucosamine; at  $1448$  and  $1582\text{ cm}^{-1}$  tentatively assigned to lipid vibrations; and at  $1656\text{ cm}^{-1}$  which is a broad peak resulted from the overlapping of two peaks assigned for Amid I in protein and a carbon-carbon double bond stretching mode vibration in lipid.

The most statistically significant differences were revealed by performing a Principal Component Analysis on all of the spectra together. The original spectra consisted of 1993 intensity channels which the PCA was able to reduce into 13 principal components (PCs) which maintained 99.3% of the variance in the data sets. The first PC accounted for 70.9% of the data variation, while PC2 and PC3 accounted for 17.9% and 3.5%, respectively. A plot of PC loadings (shown in Figure 6.2) can provide significant information about the biochemical basis of the mathematical discrimination.<sup>16</sup> The loadings of PC1 are shown in Figure 6.2(A). This plot has strong negative peaks at  $1154$ ,  $1518$ , and  $1182\text{ cm}^{-1}$  (assigned to proteins) which are associated with the dominant features in the spectra from TA and WT cells. PC1 also has strong

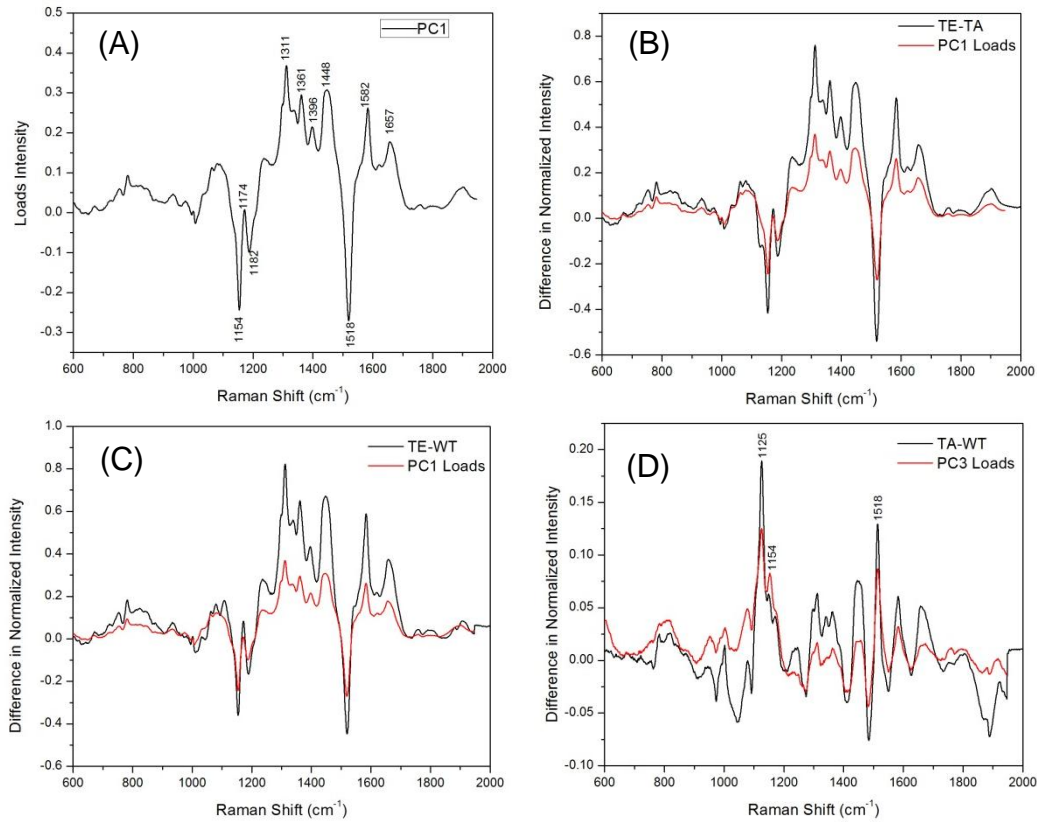
positive peaks associated with the dominant features in the spectra from TE cells, which were discussed above.

Table 6.1: Assignment of the Raman vibrational bands observed in this study.

Raman shift (cm <sup>-1</sup> )				Assignments	
TA Envelope	TE Envelope	TA Cells WT Cells	TE Cells	Vibrational modes	Location
748(m)	747(m)		752(w)	Ring I deformation in flavin <sup>17,18,19</sup>	Vitamin
		782(w)	782(w)	Cytosine, <sup>20,21,22</sup> uracil, <sup>20,22,23</sup> ring stretching <sup>21</sup>	DNA/RNA
845(w)	845(w)			v(C-N) from tyrosine group in proteins, <sup>18,19,24</sup> v(C-C) ring breathing <sup>21,25</sup>	Protein
894(w)	894(w)			v(C-O-C) <sup>22</sup> in carbohydrates, <sup>26</sup> v(C-N) in proteins <sup>19</sup>	Carbohydrate, Protein
931(m)	931(m)			v(C-O-C) 1,4-glycosidic link in carbohydrates, <sup>25,27</sup> v(C-C) in proteins, <sup>27</sup> ρ(CH <sub>3</sub> ) terminal <sup>26</sup>	Carbohydrate, Protein
1001(w)	1001(w)	1004(m)	1004(m)	v(C-C) aromatic ring breathing of phenylalanine <sup>20,21,22,25,26,27,28</sup>	Protein
1036(sh)	1036(sh)			v(C-C) skeletal, <sup>26</sup> v(PO <sub>2</sub> ), <sup>24</sup> δ(CH) in-plane <sup>27</sup>	Protein
	1060(sh)		1064(sh)	v(C-N), <sup>20,27</sup> v(C-C) <sup>20</sup>	Protein
1123(s)	1121(m)	1125(s)	1125(m)	v(C-C) <sup>20,21,22</sup> skeletal <sup>26</sup> , v(C-N) in protein, <sup>19,20,21,27</sup> v(C-O) in carbohydrate, <sup>27</sup> v(C-C) in lipid, <sup>22,27</sup> =CC= in lipids <sup>19</sup>	Protein, Carbohydrate, Lipid
1150(sh)		1154(s)	1154(w)	v(C-C) <sup>25,26,27,28,29,30</sup>	Protein
	1170(sh)		1174(sh)	Aromatic amino acids, <sup>18,19,31</sup> δ(C-H) in tyrosine <sup>25,27,32</sup>	Protein
		1182(sh)		δ(C-H) in tyrosine <sup>25,27</sup>	Protein
1228(m)	1227(m)			amide III <sup>20,21,22,25</sup>	Protein
1307(m)	1310(s)	1296,1311(w)	1311(s)	δ(CH <sub>2</sub> ), <sup>26</sup> twist in lipids, <sup>25,27</sup> δ(OH) <sup>26</sup>	Lipid
1363(m)	1360(m)	1361(w)	1361(m)	C-H bend, amino acids <sup>18,19,31</sup>	Protein
	1394(w)	1396(vw)	1396(m)	v(COO), <sup>19</sup> amino acids <sup>31</sup>	Protein
1447(s+b)	1447(vs+b)	1448(m+b)	1448(s+b)	δ(C-H <sub>2</sub> ) scissoring <sup>20,21,22,23,24,26</sup>	Carbohydrate, Lipid
1514(s)	1513(w)	1518(s)	1518(vw)	v(C=C) <sup>29,30</sup>	Protein
1582(m)	1582(s)	1582(m)	1583(s)	v(C=C) <sup>18,19</sup>	Lipid
1655(m+b)	1655(m+b)	1657(w+b)	1656(m+b)	Amide I and unsaturated lipids, <sup>20,23</sup> amide I and v(C=C) in lipid <sup>25</sup>	Protein, Lipid

δ: deformation vibration, v: stretching vibration, ρ: rocking vibration.

b: broad, m: medium, s: strong, sh: shoulder, vs: very strong, vw: very weak, w: weak.



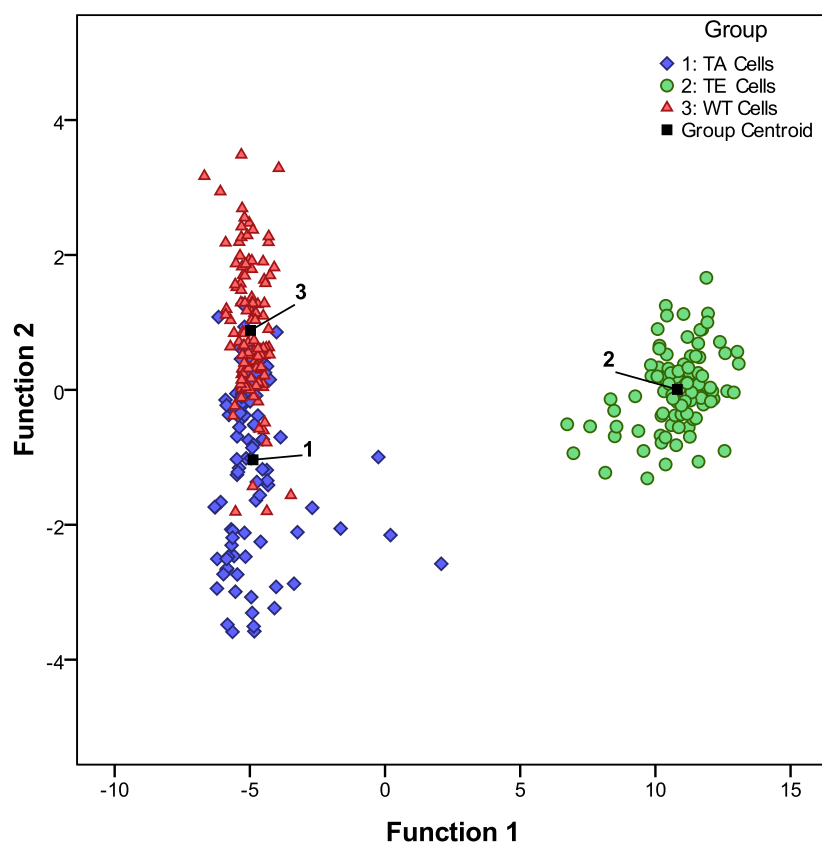
**Figure 6.2:** Principal component loadings of the PCA performed on the Raman spectra acquired from three mutants of *M. smegmatis*. (A) The loadings of the first PC. Prominent spectral features are identified. (B) PC1 loadings plotted with the difference of the average Raman spectrum of TA cells and TE cells. (C) PC1 loadings plotted with the difference of the average Raman spectrum of WT cells and TE cells. (D) PC3 loadings plotted with the difference of the average Raman spectrum of TA bacteria and WT bacteria.

Figure 6.2 indicates that PC1 is constructed to maximize the spectral differences between TE cells and WT/TA cells and identifies the important biochemical components of these differences. PC1 does not show a considerable difference between TA and WT bacteria. To further highlight the significance of PC1, Figure 6.2(B) shows a plot of PC1 and the resulting difference spectrum when the average spectrum of TA cells is subtracted from the average spectrum of TE cells and Figure 6.2(C) shows a plot of PC1 and the resulting difference

spectrum when the average spectrum of WT cells is subtracted from the average spectrum of TE cells. The similarities in these plots reinforce the interpretation that the basis of discrimination between spectra is the change in the Raman spectral features of the cells expressing phosphomimetic *wag31T73E*. It has been found that the third PC (PC3) is significant in the discrimination between TA and WT cells, based on the subtle differences in their spectra. Figure 6.2(D) shows the similarity between the PC3 loadings plot and the resulting difference spectrum when the average spectrum of WT cells is subtracted from the average spectrum of TA cells. The main changes were observed in protein peaks at 1518, 1125, and 1154  $\text{cm}^{-1}$ , although none of these are as large as the dominant features in 6.2(B) or 6.2(C).

The thirteen PC scores were used as independent input variables in a discriminant function analysis (DFA), which further reduced the dimensionality of the spectra. For discrimination among the three bacterial cell types, two discriminant function (DF) scores were calculated for each individual spectrum. The DFA allows a rapid sorting or grouping of unknown spectra on the basis of the discriminant functions, and also gives an immediate measurement of the reproducibility of the spectra, as highly similar spectra should possess highly similar DF scores, and thus should be grouped closely in a DFA. Figure 6.3 shows the DFA performed on the 316 Raman spectra from the three bacterial cell types. In this figure, each colored point in the plot is a spectrum that is represented by the two scalar discriminant functions scores, DF1 and DF2. All the spectra from Group 1 (TA cells) and Group 3 (WT cells) possess an almost identical DF1 score, indicating their high degree of similarity. DF1 always accounts for a greater percentage of variance in the data than does DF2. On the basis of their differing DF2 scores, we conclude that these two cell types are still reproducibly different, however. All

the spectra from Group 2 (TE cells) possess a very different DF1 score, indicating their high degree of difference from the other two groups. In this analysis, 100% of the spectra obtained from the TE cells were correctly classified by the DFA, indicating that these bacteria are reproducibly molecularly distinct from the other two. Only 69% of the TA bacteria and 88.9% of the WT bacteria were correctly classified, indicating that their spectra were similar due to an almost identical molecular composition.



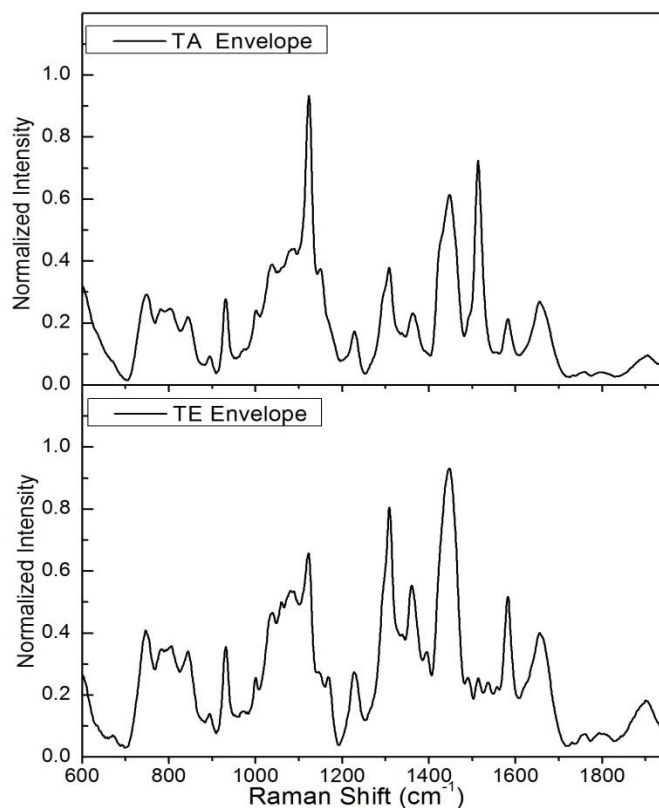
**Figure 6.3:** A discriminant function analysis (DFA) of the Raman spectra from the three *M. smegmatis* cell types studied in this work. 13 principal component loadings from a PCA were used as the independent variables for each spectrum. The high similarity of discriminant function one scores indicates that the TA and WT cells are highly similar, yet still differentiable. TE cells show the greatest biochemical difference.

### 6.3.2 Raman Spectra from Bacterial Cell Envelope

In order to localize the molecular changes that occur between the bacteria with the phosphorylated form of Wag 31 and that with the non-phosphorylated form of Wag31 within the cell, the P60 cell envelope fraction was isolated and Raman measurements were performed on a dried suspension of the cell envelope. Figure 6.4(A) shows the averaged Raman spectra for the P60 cell membrane fraction of bacteria with Wag31T73A (labeled “TA envelope” – top) and with Wag31T73E (labeled “TE envelope” – bottom).

Ninety-nine TA envelope spectra and 101 TE envelope spectra were averaged to make these spectra. Spectra of the P60 cell envelope fraction of the wild-type bacteria were not taken. Significant differences between TA cell envelope and TE cell envelope can be observed at the same locations as were measured in the bacterial cells, indicating that significant cellular changes occurred in the cell envelope. Table 6.1 provides the detailed assignments for the main features which appeared in the cell envelope spectra. It was observed that the lipid peaks which are located at 1448 and 1582  $\text{cm}^{-1}$  seem to be stronger in the TE envelope spectrum than in the TA envelope spectrum indicating that TE cell envelope contains more lipid than the TA cell envelope. Moreover, TE envelope spectra show an enhancement in the peaks assigned for amino acids in protein such as the peaks at 1311, 1361, and 1396  $\text{cm}^{-1}$ . This result is consistent with the results of a study which revealed a higher enzymatic activity of peptidoglycan biosynthetic pathway (MurX and MurG) and a greater production of lipid II in cells expressing *wag31T73E<sub>Mtb</sub>* than cells expressing *wag31<sub>Mtb</sub>* or *wag31T73A<sub>Mtb</sub>*.<sup>11</sup> These Raman spectroscopic results indicate that cells with the *wag31T73E<sub>Mtb</sub>* allele produce more peptidoglycan precursor molecules than those expressing *wag31<sub>Mtb</sub>* or *wag31T73A<sub>Mtb</sub>*.

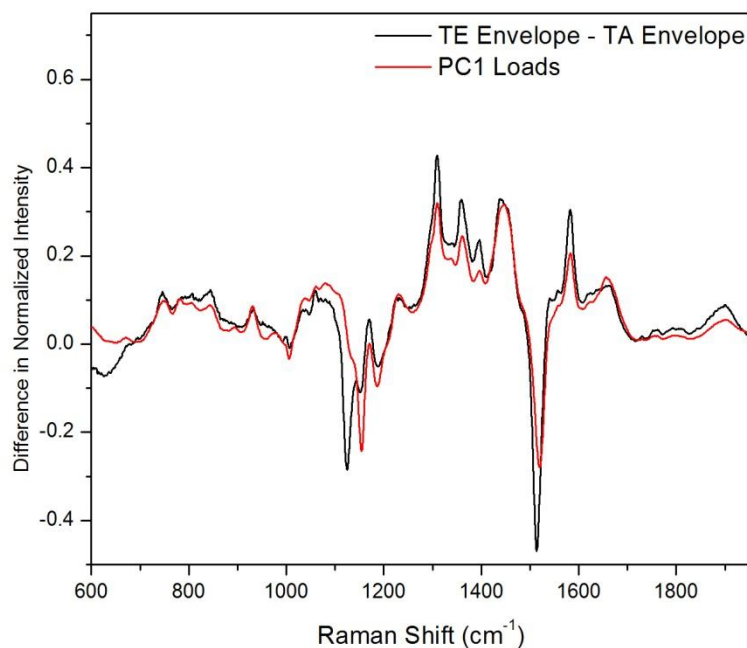
To accentuate the differences in these spectra, in Figure 6.5 the average spectrum of the TA cell envelope has been subtracted from the average spectrum of the TE cell envelope and



**Figure 6.4:** The average Raman spectra of P60 cell envelope fraction of the *M. smegmatis* cells expressing phosphoablative *wag31T73A<sub>Mtb</sub>* (TA) and phosphomimetic *M. tuberculosis wag31 (wag31T73E<sub>Mtb</sub>)* (TE).

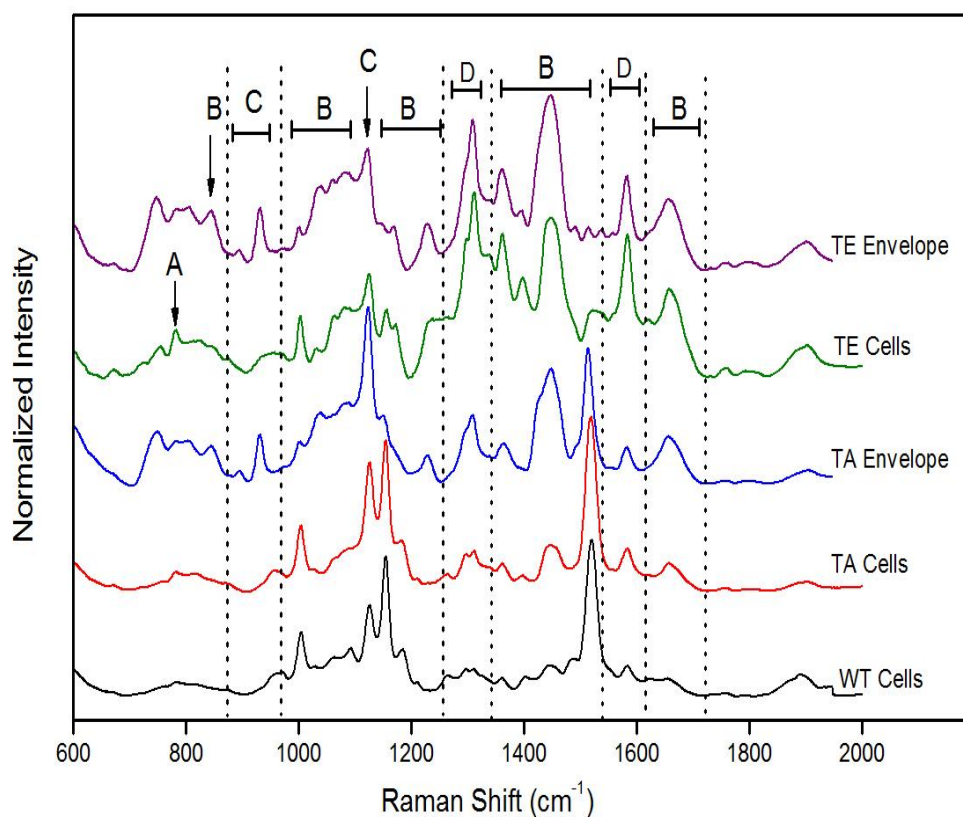
plotted with the PC1 loading from a PCA performed on these data. This analysis demonstrates that the PCA classification of these data relies on the main spectral changes in the Raman spectra of the samples under investigation.

Figure 6.6 compares the average spectrum of the whole bacteria cells with their corresponding average spectrum obtained from the cell envelope fraction. Noticeably,



**Figure 6.5:** The difference between the average spectrum of the TA and TE cell envelope fraction (black) plotted with the PC1 loadings (red).

considerable differences are observed between the spectra obtained from cells possessing the phosphoablative Wag31T73A and cells possessing the phosphomimetic Wag31T73E. Strong similarities (with some slight differences) in the spectra obtained from bacterial cells and the spectra obtained from the corresponding bacterial cell envelope indicate that the significant spectral changes observed between cells with Wag31T73A and Wag31T73E are primarily due to biochemical changes localized in the cell membrane and wall.



**Figure 6.6:** A comparison of the average Raman spectra of the five classification groups studied in this work (the spectra of the cells of the three *wag31* conditional mutants of *M. smegmatis* and the spectra of the cell envelope fraction of two of them).

Molecular identification of these differences suggests an increase in peptidoglycan biosynthesis and production of lipid II. These results are consistent with previous enzymatic studies and reports of the differences observed in cell-division and multiplication between cells with the *wag31T73E<sub>Mtb</sub>* allele and those expressing *wag31<sub>Mtb</sub>* or *wag31T73A<sub>Mt</sub>*. Raman spectra from cells expressing *wag31<sub>Mtb</sub>* or *wag31T73A<sub>Mt</sub>* were almost identical. Figure 6.6 shows the regions of the tentative assignments corresponding to the main components of the bacterial cells, namely, nucleic acids (A), proteins (B), carbohydrates (C), and lipids (D).

All the 516 spectra obtained from the five different samples (TE cell and envelope fraction, TA cell and envelope fraction, and WT cells) were analyzed using PCA followed by DFA as described above. The analysis resulted in the 100% correct classification of TE bacterial cell spectra, 99% correct classification of TE cell envelope spectra, 95% correct classification of TA cell envelope spectra, 67% correct classification of TA bacterial cell spectra, and 85.5% correct classification of WT bacterial cell spectra. The resulting PC-DFA plot (Figure 6.7) demonstrates the power of non-surface-enhanced visible-wavelength Raman spectroscopy to easily reveal subtle molecular differences in bacterial cells expressing different alleles and to localize those molecular differences in a specific domain of the cell structure. The clustering of data points around the group centroid in this graph which is composed of hundreds of spectra acquired from multiple cultures over an extended period of time also demonstrates that there is little variation in day-to-day measurements within the same group. The residual scatter in the data is indicative of typical measurement noise and is relatively small for similar studies of this nature. It is noticed that WT bacterial cells and TA bacterial cells are highly similar due to the similarity of the values of DF1 and DF2 for their spectra, while significant differences were observed between the other three classification groups (TE bacterial cells, as well as TA and TE cell envelopes). This result is a statistical chemometric way of quantifying the similarities and dissimilarities between the average spectra shown in Figure 6.6.

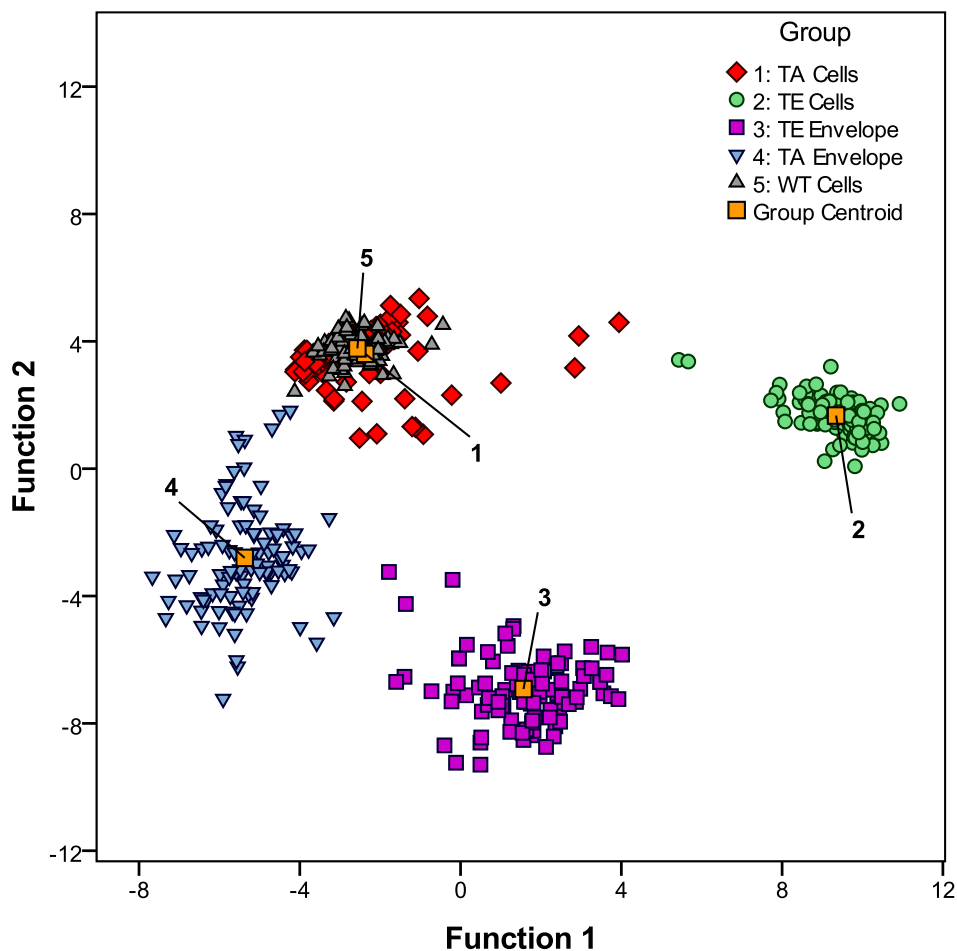


**Figure 6.7:** A PCA-DFA plot of all the Raman spectra showing the high-degree of similarity between wild-type and TA cells, and the ability to easily distinguish spectra from other groups.

The results presented here demonstrate that visible wavelength Raman-spectroscopy can be an effective tool to reveal the biomolecular differences in the *wag31* conditional mutants of *M. smegmatis*, that this spectroscopy can be performed with excellent signal-to-noise on the cell envelope fraction of these cells, and that significant biochemical and/or structural changes in the cell envelope can be measured, indicating that *wag31* and its phosphorylation play an important role in peptidoglycan synthesis and the growth of mycobacteria.

## 6.4 Raman Spectroscopy on Protein

The next proposed step in this project is to study the three different forms of the wag31 protein spectroscopically. An effort to purify *wag31T73E<sub>Mtb</sub>* and *wag31T73E<sub>Mtb</sub>* proteins for Raman spectroscopy was carried out in the laboratory of Dr. Kang. All Raman spectra collected from these proteins were dominated by the strong protein-fixing buffer features as can be seen in Figure 6.8.

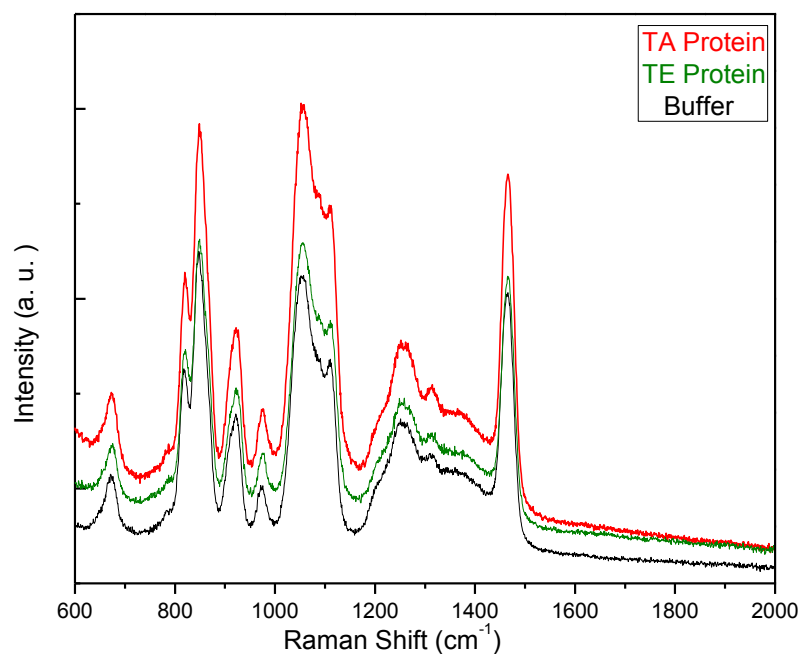


**Figure 6.8:** A typical Raman spectra obtained from *wag31T73E<sub>Mtb</sub>* and *wag31T73E<sub>Mtb</sub>* protein compared with the Raman spectrum obtained from the protein-fixing buffer.

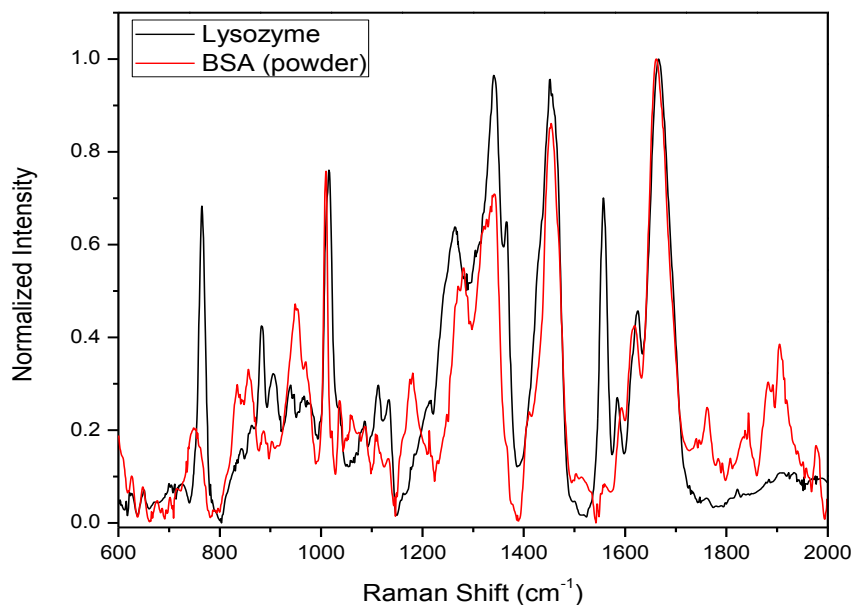


**Figure 6.9:** A comparison between typical spectra obtained from powdered lysozyme and BSA proteins.

The ability to detect biomolecular conformation differences in different protein forms is very important, but the very small Raman differences expected between proteins with different conformations will require a high Raman signal to noise and no contribution from the buffer. To begin this study, I investigated two easy to procure and produce proteins: lysozyme and BSA. First the powdered forms of the protein samples were tested using Raman spectroscopy. Figure 6.9 compares a typical spectrum for each one of these common proteins. Considerable differences at 765 cm<sup>-1</sup>, 1557 cm<sup>-1</sup> and after 1800 cm<sup>-1</sup> were easily observed, indicating the ability of Raman spectroscopy to differentiate different solid protein samples.

To further investigate the ability of Raman spectroscopy to detect these differences and to quantify the concentration of protein necessary for such an experiment, a solution of the powdered proteins using 1X PBS buffer was made with two different concentrations (15 mg/ml and 7.5 mg/ml). 10  $\mu$ l of each solution was transferred to the quartz slide and left two hours to dry. Figure 6.10 shows micrographs of the dried solution for BSA (to the right) and lysozyme

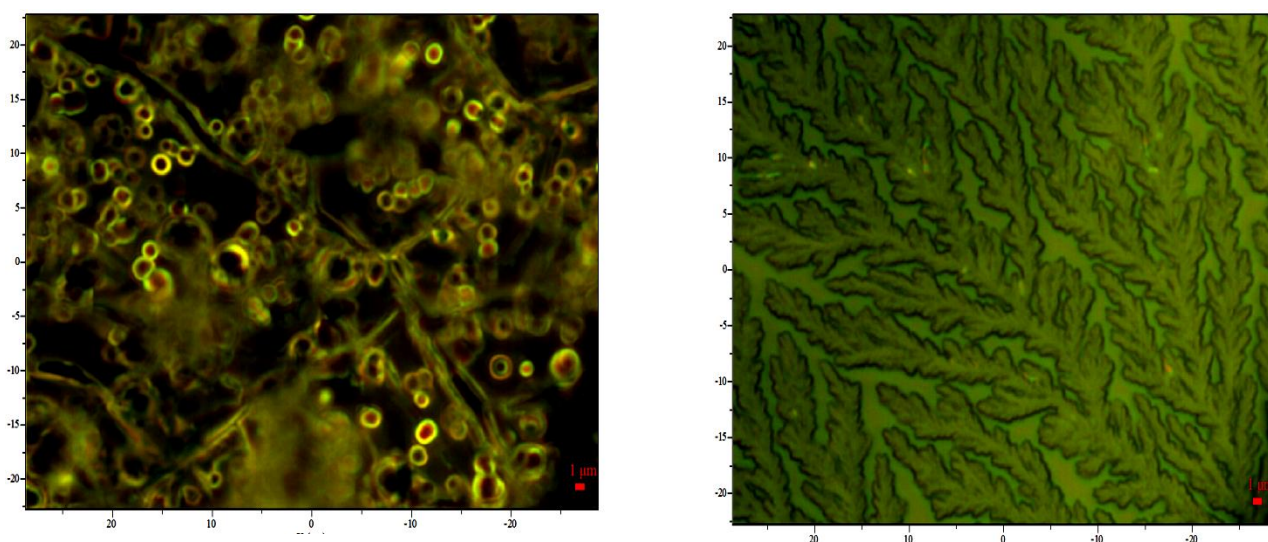


**Figure 6.10:** Micrographs of dried protein residue from solutions of lysozyme (left) and BSA (right).

(to the left) as they appeared under the 100X Raman microscope objective.

Figure 6.11 shows typical Raman spectra obtained from each case. A comparison between the three different spectra of each protein type (one powdered, two dried solutions) revealed no changes for the lysozyme case, but for BSA there were some differences due to the noise (Figure 6.12).

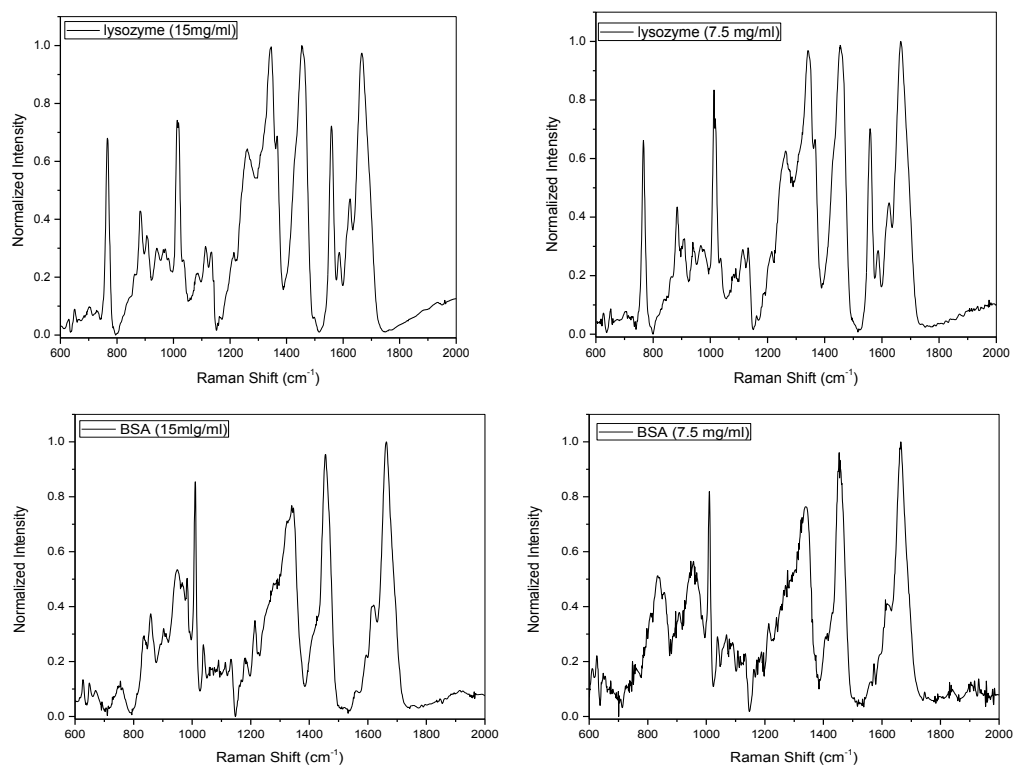


**Figure 6.11:** Raman spectra obtained from lysozyme (top) and BSA (bottom) protein solutions with different concentrations (labeled for each graph).

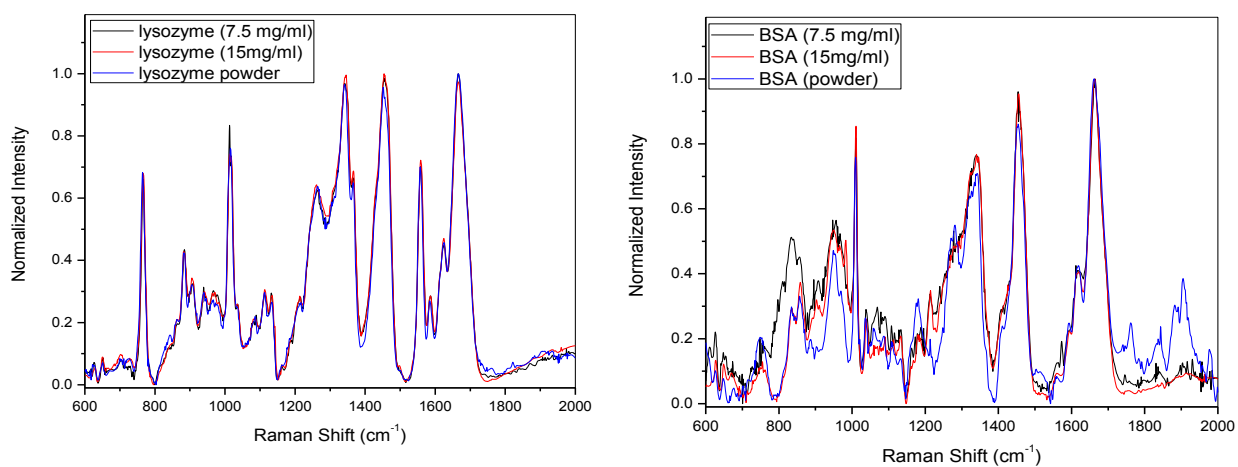


**Figure 6.12:** A comparison between Raman spectra obtained from lysozyme and BSA proteins with different concentrations.

Those figures prove that Raman spectroscopy could detect a good signal from the protein samples even in a low concentration solution. The noise problem (which appeared in the BSA case) can be solved by drying multiple layers of the solution on the slide or increasing the scan time. This result is encouraging and suggests the next step is to purify wag31 protein using a non-feature-fixing gel or buffer.

## 6.5 Summary

Non-surface-enhanced Raman spectroscopy using a 514.5 nm wavelength laser was used to measure in vivo the molecular difference of conditional mutants of *Mycobacterium smegmatis* expressing three different alleles: wild-type *wag31<sub>Mtb</sub>*, phosphoablative *wag31T73A<sub>Mtb</sub>*, and phosphomimetic *wag31T73E<sub>Mtb</sub>*. This study demonstrated that the phosphorylation of Wag31, a key cell-division protein, caused significant differences in the quantity of amino acids associated with peptidoglycan precursor proteins and lipid II which are observable in the Raman spectra of these cells.

Raman spectra were also acquired from the isolated P60 cell envelope fraction of the cells expressing *wag31T73A<sub>Mtb</sub>* and *wag31T73E<sub>Mtb</sub>*. A significant number of the molecular vibrational differences observed in the cells were also observed in the cell envelope fraction, indicating that these differences are indeed localized in the cell envelope. Principal component analyses and discriminant function analyses were conducted on these data to demonstrate the ease of spectral classification and the reproducibility of the data.

The Raman spectra acquired from the wag31 proteins themselves were dominated by the signature of the protein-fixing buffer. A Raman spectroscopy study was conducted on two

different easy to produce proteins, lysozyme and BSA, in both powdered and solution forms. The results revealed the ability to obtain good Raman signals from both cases with considerable differences between the different proteins, but almost no differences between the pure powdered forms and the solutions for a given protein. This result indicates that a Raman study of the Wag31 proteins is possible, assuming the protein-fixing buffer can be eliminated.

## CHAPTER 6 REFERENCES

- <sup>1</sup> 2007 *Tuberculosis Facts Sheet*. World Health Organization. (2007).
- <sup>2</sup> A.A. Salyers and D.D. Whitt (eds.). *Bacterial pathogenesis, a molecular approach*, 2<sup>nd</sup> Ed. ASM Press, Washington DC, (2002).
- <sup>3</sup> P. Fernandez, B. Saint-Joanis, N. Barilone, M. Jackson, B. Gicquel, S.T. Cole, and P.M. Alzari. “The Ser/Thr protein kinase PknB is essential for sustaining mycobacterial growth,” *Journal of Bacteriology* **188**:7778-7784 (2006).
- <sup>4</sup> C.M. Sassetti, D.H. Boyd, and E.J. Rubin. “Genes required for mycobacterial growth defined by high density mutagenesis,” *Molecular Microbiology* **48**:77-84 (2003).
- <sup>5</sup> Y. Av-Gay and M. Everett. “The eukaryotic-like Ser/Thr protein kinases of *Mycobacterium tuberculosis*,” *Trends in Microbiology* **8**:238-244 (2000).
- <sup>6</sup> S.T. Cole, R. Brosch, J. Parkhill, T. Garnier, C. Churcher, D. Harris, S.V. Gordon, K. Eiglmeier, S. Gas, C.E. Barry, 3rd, F. Tekaia, K. Badcock, D. Basham, D. Brown, T. Chillingworth, R. Connor, R. Davies, K. Devlin, T. Feltwell, S. Gentles, N. Hamlin, S. Holroyd, T. Hornsby, K. Jagels, B.G. Barrell, and et al. “Deciphering the biology of *Mycobacterium tuberculosis* from the complete genome sequence,” *Nature* **393**:537-544 (1998).
- <sup>7</sup> C.M. Kang, D.W. Abbott, S.T. Park, C.C. Dascher, L.C. Cantley, and R.N. Husson. “The *Mycobacterium tuberculosis* serine/threonine kinases PknA and PknB: substrate identification and regulation of cell shape,” *Genes & Development* **19**:1692-1704 (2005).
- <sup>8</sup> J.H. Cha and G.C. Stewart. “The divIVA minicell locus of *Bacillus subtilis*,” *Journal of Bacteriology* **179**:1671-1683(1997).
- <sup>9</sup> K. Flardh. “Essential role of DivIVA in polar growth and morphogenesis in *Streptomyces coelicolor* A3(2),” *Molecular Microbiology* **49**:1523-1536 (2003).
- <sup>10</sup> C.M. Kang, S. Nyayapathy, J.Y. Lee, J.W. Suh, and R.N. Husson. “Wag31, a homologue of the cell division protein DivIVA, regulates growth, morphology and polar cell wall synthesis in mycobacteria,” *Microbiology* **154**:725-735 (2008).
- <sup>11</sup> C. Jani, H. Eoh, J. lee, K. Hamasha, M.B. Sahana, J.-S. Han, M. Zeng, S. Nyayapathy, J.-Y. Lee, J.-W. Suh, S.H. Lee, S.J. Rehse, D. Crick, and C.-M. Kang. “Regulation of polar peptidoglycan biosynthesis by Wag31 in mycobacteria,” *BMC Microbiology* **10**:327-336 (2010).

- <sup>12</sup> C.A. Pashley and T. Parish. “Efficient switching of mycobacteriophage L5-based integrating plasmids in *Mycobacterium tuberculosis*,” *FEMS Microbiology Letters* **229**:211-215 (2003).
- <sup>13</sup> M.C. Blokpoel, H.N. Murphy, R. O’Toole, S. Wiles, E.S. Runn, G.R. Stewart, D.B. Young, and B.D. Robertson. “Tetracycline-inducible gene regulation in mycobacteria,” *Nucleic Acids Research* **33**:e22 1-7 (2005).
- <sup>14</sup> S. Khasnobis, J. Zhang, S.K. Angala, A.G. Amin, M.R. McNeil, D.C. Crick, and D. Chatterjee. “Characterization of a specific arabinosyltransferase activity involved in mycobacterial arabinan biosynthesis,” *Chemistry and Biology* **13**:787-795 (2006).
- <sup>15</sup> A. Cao, A. K. Pandya, G.K. Serhatkulu, R.E. Weber, H. Dai, J.S. Thakur, V.M. Naik, R. Naik, G.W. Auner, R. Rabah, and D.C. Freeman. “A robust method for automated background subtraction of tissue fluorescence,” *Journal of Raman Spectroscopy* **38**:1199-1205 (2007).
- <sup>16</sup> A.S. Haka, K E. Shafer-Peltier, M. Fitzmaurice, J. Crowe, R.R. Dasari, and M.S. Feld. “Identifying microcalcifications in benign and malignant breast lesions by probing differences in their chemical composition using Raman spectroscopy,” *Cancer Research* **62**:5375-5380 (2002).
- <sup>17</sup> Y. Zheng, P.R. Carey, and B.A. Palfey. “Raman spectrum of fully reduced flavin,” *Journal of Raman Spectroscopy* **35**:521-524 (2004).
- <sup>18</sup> M.L. Laucks, A. Sengupta, K. Junge, E.J. Davis, and B.D. Swanson. “Comparison of psychroactive arctic marine bacteria and common mesophilic bacteria using surface-enhanced Raman spectroscopy,” *Applied Spectroscopy* **59**:1222-1228 (2005).
- <sup>19</sup> A. Sengupta, M.L. Laucks, and E.J. Davis. “Surface-enhanced Raman spectroscopy of bacteria and pollen,” *Applied Spectroscopy* **59**:1016-1023 (2005).
- <sup>20</sup> W.E. Huang, R.I. Griffiths, I.P. Thompson, M.J. Bailey, and A.S. Whiteley. “Raman microscopic analysis of single microbial cells,” *Analytical Chemistry* **76**:4452-4458 (2004).
- <sup>21</sup> M. Harz, P. Rosch, K.-D. Peschke, O. Ronneberger, H. Burkhardt, and J. Popp. “Micro-Raman spectroscopic identification of bacterial cells of the genus *Staphylococcus* and dependence on their cultivation conditions,” *Analyst* **1**:1543-1550 (2005).
- <sup>22</sup> A.C. Singer, W.E. Huang, J. Helm, and I.P. Thompson. “Insight into pollutant bioavailability and toxicity using Raman confocal microscopy,” *Journal of Microbiological Methods* **60**: 417-422 (2005).

- <sup>23</sup> K. Maquelin, L.P. Choo-Smith, T. van Vreeswijk, H.P. Endtz, B. Smith, R. Bennett, H.A. Bruining, and G.J. Puppels. "Raman spectroscopic method for identification of clinically relevant microorganisms growing on solid culture medium," *Analytical Chemistry* **72**:12-19 (2000).
- <sup>24</sup> J.D. Gelder, P. Scheldeman, K. Leus, M. Heyndrickx, P. Vandenabeele, L. Moens, and P.D. Vos. "Raman spectroscopic study of bacterial endospores," *Analytical and Bioanalytical Chemistry* **389**:2143-2151 (2007).
- <sup>25</sup> I. Notingher. "Raman spectroscopy cell-based biosensors," *Sensors* **7**:1343-1358 (2007).
- <sup>26</sup> A.C. Williams and H.G.M. Edwards. "Fourier transform Raman spectroscopy of bacterial cell walls," *Journal of Raman Spectroscopy* **25**:673-677 (1994).
- <sup>27</sup> L.J. Goeller and M.R. Riley. "Discrimination of bacteria and bacteriophages by Raman spectroscopy and surface-enhanced Raman spectroscopy," *Applied Spectroscopy* **61**:679-685 (2007).
- <sup>28</sup> I. Notingher, J. Slevakumaran, and L.L. Hench. "New detection system for toxic agents based on continuous spectroscopic monitoring of living cells," *Biosensors and Bioelectronics* **20**:780-789 (2004).
- <sup>29</sup> W.F. Howard, Jr., W.H. Nelson, and J.F. Sperry. "A resonance Raman method for the rapid detection and identification of bacteria in water," *Applied Spectroscopy* **34**:72-75 (1980).
- <sup>30</sup> R.A. Dalterio, M. Baek, W.H. Nelson, D. Britt, J.F. Sperry, and F.J. Purcell. "The resonance Raman microprobe detection of single bacterial cells from a chromobacterial mixture," *Applied Spectroscopy* **41**:241-244 (1987).
- <sup>31</sup> A. Sengupta, M.L. Lauckes, N. Dildine, E. Drapala, and E.J. Davis. "Bioaerosol characterization by surface-enhanced Raman spectroscopy (SERS)," *Aerosol Science* **36**:651-664 (2005).
- <sup>32</sup> U. Neugebauer, U. Schmid, K. Baumann, U. Holzgrabe, W. Ziebuhr, S. Kozitskaya, W. Kiefer, M. Schmitt, and J. Popp. "Characterization of bacterial growth and the influence of antibiotics by means of UV resonance Raman spectroscopy," *Biopolymers* **82**:306-311 (2006).

## Chapter 7

### Surface-Enhanced Raman Spectroscopy (SERS) Study of Bacteria

#### 7.1 Introduction

As stated in Chapter 2, Raman signals obtained from bacterial samples suffer from weakness and a huge background. Surface-enhanced Raman spectroscopy (SERS) is one of the most common methods used to overcome this issue.<sup>1</sup> In 1974 for the first time, Fleischman *et al.* observed a large enhancement in the Raman spectra of pyridine adsorbed on a roughened silver electrode<sup>2</sup> and in 1977 the cause of such enhancement was explained by Jeanmaire and Van Duyne.<sup>3</sup>

Since then Raman signal enhancement has been observed using suspensions of gold or silver nanoparticles and since 1979 they have been widely used for SERS measurements. The shape and size of the nanoparticles is of great importance and should be specified. Too small particles will not enhance the field due to the lack of electrical conductance and the too large particles will decrease the enhancement efficiency due to their ability to excite multipole transitions (Raman scattering is caused by the dipole transition only).<sup>4</sup>

Despite the fact that SERS should provides the same signal features that RS does with great enhancement, there are always some changes observed in the SERS spectrum compared to the same sample's Raman spectrum. Some peaks will be shifted, some disappear, and others will be formed. This irreproducibility of the spectra is affected by the inhomogeneity of the bacteria and colloidal suspension and the molecules' symmetry where a very slight difference in the symmetry of the molecule will lead to a different vibrational mode.<sup>5</sup>

The goal of this study was to evaluate the signal enhancement achieved by using surface-enhanced Raman spectroscopy by comparing the resultant SERS spectra with the traditional Raman spectra. SERS measurements were obtained from different bacterial strains which studied previously using traditional Raman spectroscopy. Silver colloid nanoparticles were prepared and mixed with different bacteria suspensions and the resultant SERS spectra were compared to the original Raman spectra. To evaluate the efficiency of colloidal nanoparticles and their stability, a SERS test on the molecular dye rhodamine 6G was performed.

## **7.2 Materials and Methods**

### **7.2.1 Microorganisms and Growth Conditions**

Two *E. coli* strains, the pathogenic strain O157:H7 and the non-pathogenic strain *Hfr* K-12 were selected for this study. Their growth conditions were described in Chapter 4. Also the three *M. smegmatis* conditional mutant strains of *wag31* containing tetracycline-inducible  $P_{tet}$ -*wag31*,  $P_{tet}$ -*wag31T73A* or  $P_{tet}$ -*wag31T73E* at the *attB* locus were used for the SERS study. Their growth conditions were discussed in Chapter 6.

### **7.2.2 Silver Colloids Solution Materials and Preparation**

The SERS materials that were used in this study include silver nitrate ( $AgNO_3$ ), trisodium citrate ( $Na_3C_6H_5O_7$ ), sodium borohydride ( $NaBH_4$ ), and Rhodamine 6G. Mili-Q grade water (18.2 M $\Omega$ /cm) was used for all solution preparation.

The silver colloids were prepared using two different methods:

1: The first method was based on the Lee and Meisel method<sup>6</sup> where 90 mg of  $\text{AgNO}_3$  was dissolved in 500 mL of DI water to form 500 mL of a 1 mM  $\text{AgNO}_3$  aqueous solution. The solution was heated with stirring to reach the boiling point, meanwhile 10 mL of 1% trisodium citrate solution was prepared by dissolving 0.1 g of  $\text{Na}_3\text{C}_6\text{H}_5\text{O}_7$  in 10 mL DI water and added to the boiling solution and then the mixture was allowed to boil with stirring for one hour. According to the method of Cyrankiewicz et al.<sup>7</sup> a simple modification was made in the way of adding trisodium citrate solution; the addition was done in four portions (the first portion was 0.2 mL and the other three 0.6 mL each). When the temperature of the  $\text{AgNO}_3$  solution reached 90°C, the first portion was added, the next portion was added at 95°C and then the third and fourth portions were added after a time interval of 15 minutes. After that the mixture was allowed to boil with stirring for 30 minutes instead of one hour. Finally the resultant dark grey color solution was left to cool down with stirring at room temperature.

2: The second method was based on the Creighton method<sup>8</sup> where 2 mM  $\text{NaBH}_4$  was prepared by dissolving 11.3 mg of  $\text{NaBH}_4$  in 150 mL of deionized water and allowed to cool down using ice with stirring for 10 minutes. Meanwhile 1 mM  $\text{AgNO}_3$  was prepared by dissolving 8.49 mg of  $\text{AgNO}_3$  in 50 mL water and adding it in portions to the solution while cooling with stirring. The brownish color solution was used for SERS measurements.

$10^{-2}$  M solution of Rhodamine 6G (R6G) in ethanol was prepared by dissolving 0.479 mg R6G in 10 mL ethanol, then a  $10^{-4}$  M solution of R6G was prepared by adding 10 mL of ethanol to 0.1 mL of the  $10^{-2}$  M R6G solution. Finally, the desired  $10^{-6}$  M solution of R6G was prepared by adding 10 mL of ethanol to 0.1 mL of the  $10^{-4}$  M R6G solution.

### **7.2.3 Raman Data Collection**

The Ag colloids solution was mixed with the R6G solution and the bacterial suspension with different ratios. SERS measurements were acquired from dried spots of the samples using the Raman instrumentation previously described. Each spectrum was obtained from 3 exposures with a scanning time of 10 seconds in the spectral region  $600\text{-}2000\text{ cm}^{-1}$ .

## **7.3 Results and Discussion**

### **7.3.1 R6G results**

To evaluate the enhancement efficiency of the prepared silver colloids and the colloidal stability, a  $1\text{ }\mu\text{M}$  solution of R6G dye was mixed with the silver colloids solution (prepared using the first method) in three different ratios. SERS spectra of these ratios are shown in Figure 7.1. It can be noticed that the best enhancement occurred when the same amount of R6G and the colloids solutions was mixed.

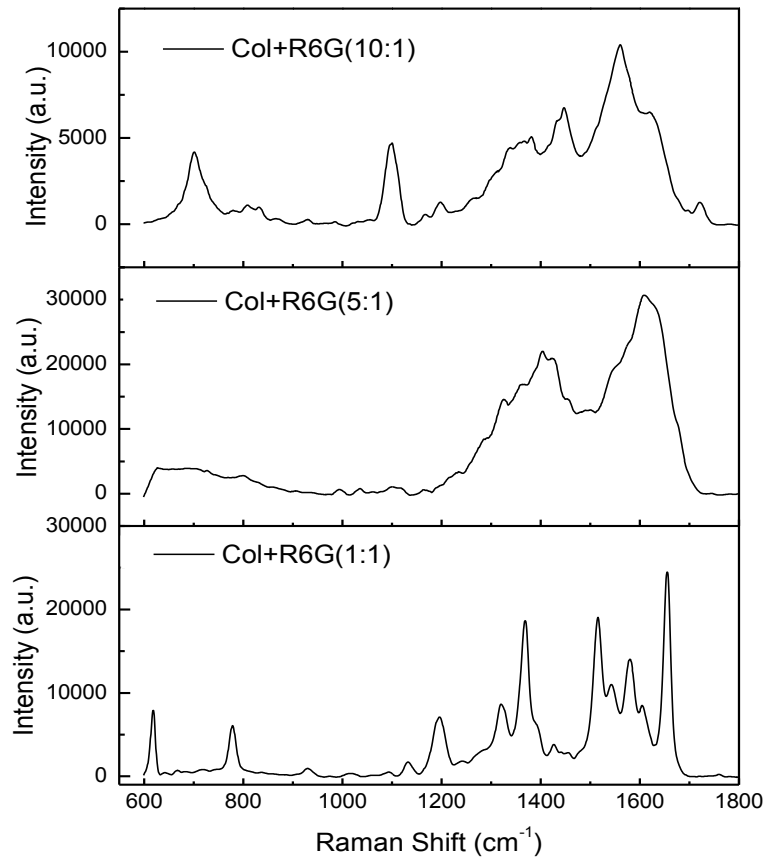


**Figure 7.1:** Raman spectra of R6G dye solution and silver colloids solution mixed with different ratios.

Figure 7.2 compare a spectrum obtained without using the colloids with a SERS spectrum of R6G dye. Also a silver colloids spectrum is plotted for this comparison to insure that the colloids peaks are not included in the SERS spectra of R6G. The raw data plotted in Figure 7.2(A) reveals the many-fold enhancement that occurred to the R6G Raman signal. For a closer look at the R6G features in both cases, Raman and SERS spectra obtained from R6G were processed and normalized as appeared in Figure 7.2(B). The spectra were shifted vertically for clarity. All the peaks were recovered with an  $11-21\text{ cm}^{-1}$  shift to lower wavenumber.

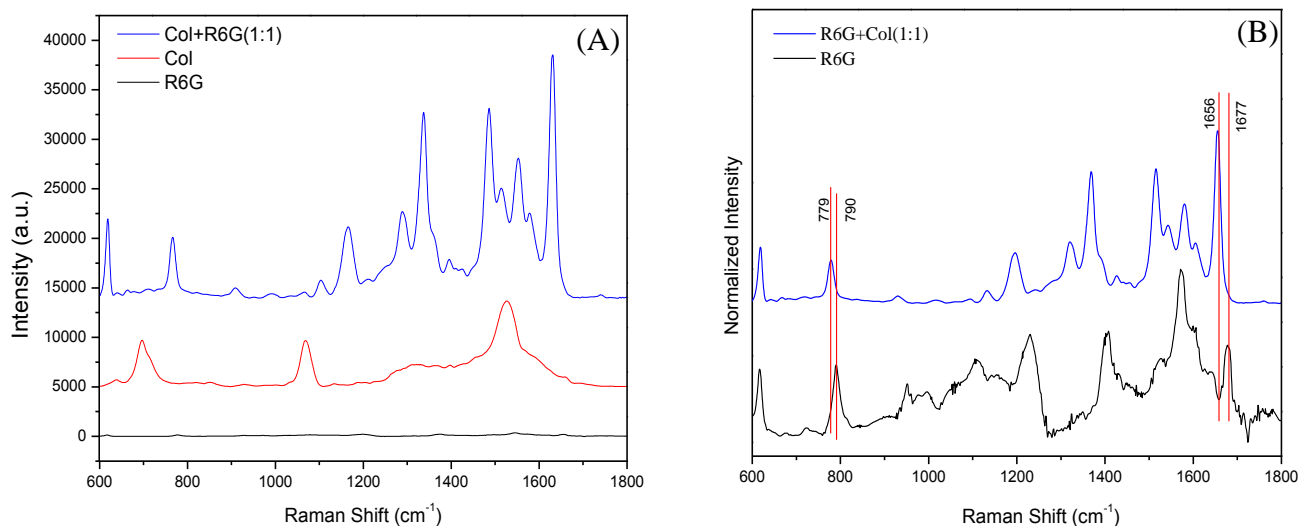


**Figure 7.2:** (A) A comparison between the spectra of R6G, Ag colloids and the mixture of equal amount of R6G and Ag colloids. (B) A comparison between processed Raman spectra and SERS spectra of R6G dye.

### 7.3.2 Bacteria results

Four different amounts of *E. coli* K12 bacterial suspension and silver colloids solution (prepared using the first method) were mixed to form four different ratios: 1:1, 1:5, 1:10 and 1:50 and tested using Raman spectroscopy. Figure 7.3 shows a typical SERS spectrum for each case. The best enhancement observed was for the samples with an *E. coli* to colloids ratio equal to 1:10 and 1:50.

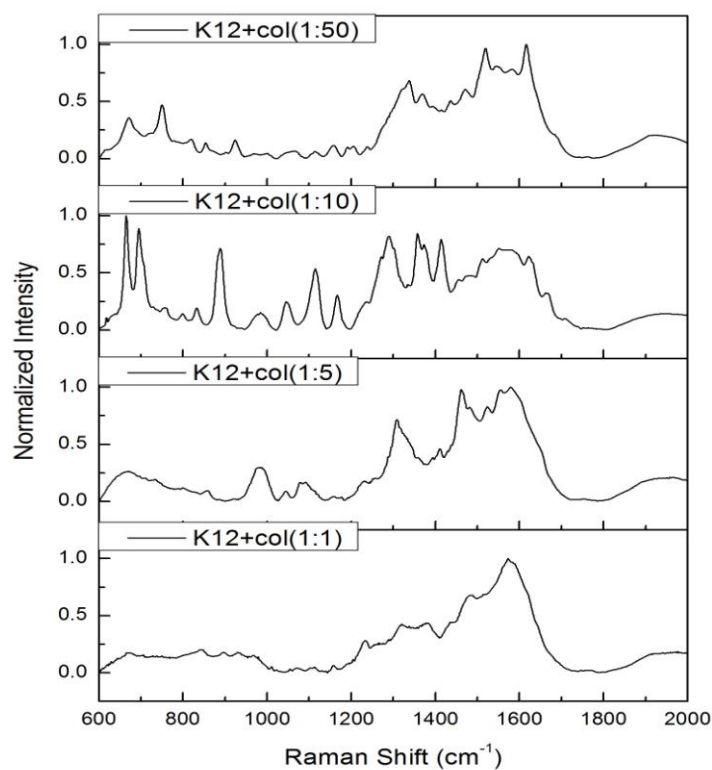


**Figure 7.3:** SERS spectra of *E. coli* K12 and the silver colloids solution mixed with different ratios.

Figure 7.4 compares a typical Raman spectrum of K12 and its SERS spectra with 1:10 and 1:50 ratios. Raw data are on the left and processed data are on the right.

When 10  $\mu\text{L}$  of *E. coli* K12 suspension was mixed with 5 mL of colloids solution, the signal was considerably enhanced but this enhancement was dominated by a huge background in the spectral region from 1000-1700  $\text{cm}^{-1}$ . Moreover, I observed considerable differences between the peaks of the Raman signal and SERS signal which indicated that SERS was not successfully able to reproduce the same signal obtained from the non-enhanced Raman spectroscopy.

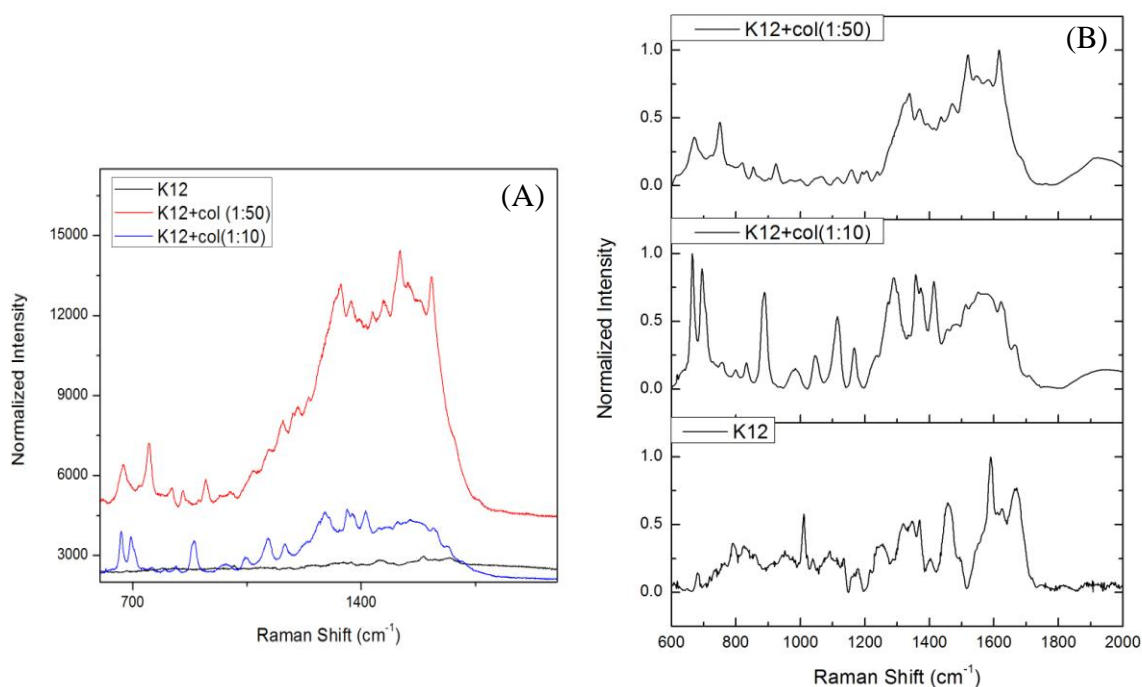


**Figure 7.4:** A comparison between SERS and Raman spectra of *E. coli* K12, (A) raw data shows the signal enhancement, (B) processed data compares the signal features.

SERS spectra were acquired also from the three *M. smegmatis* conditional mutant strains (TA, TE, and WT). A mixture from the same quantity of bacteria and colloids was prepared and tested via Raman spectroscopy. The resultant spectra (shown in Figure 7.5(A)) were dominated

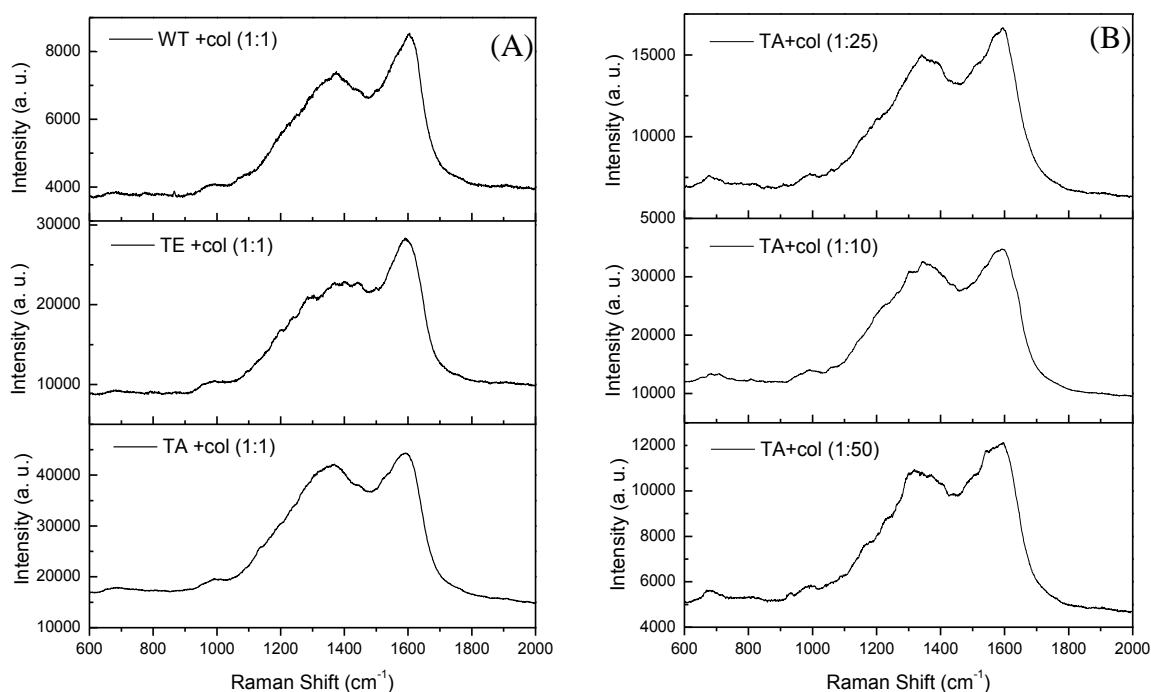


**Figure 7.5:** (A) SERS spectra of TA, TE, and WT *M. smegmatis* and the silver colloids solution mixed with equal amounts. (B) SERS spectra of varying TA-colloids ratios.

by huge humps without recovering any features or Raman peaks that had been observed earlier.

Before drawing any conclusions, the experiment was repeated for different concentrations of bacteria in colloids solution and the Ag colloids solution was prepared eight different times and tested on R6G dye to be sure that it worked very well. All SERS spectra obtained from different ratios of *M. smegmatis* bacteria revealed the same result (Figure 7.5(B))

shows an example), so I conclude that for these strains of bacteria, the silver colloids did not work as it should be.

Ag colloids prepared using the second method were tested first using R6G dye to ensure the stability of the colloids and their ability to enhance the signal. Again the best enhancement occurred when the same amount of the dye and colloids solutions were mixed together. After that SERS spectra of *M. smegmatis* were obtained using this colloids solution. One more time the resultant spectra revealed the negative result that Ag colloids are not good for the enhancement purpose when applied to this kind of bacteria. Figure 7.6 shows an example of SERS spectra acquired from TA bacteria.

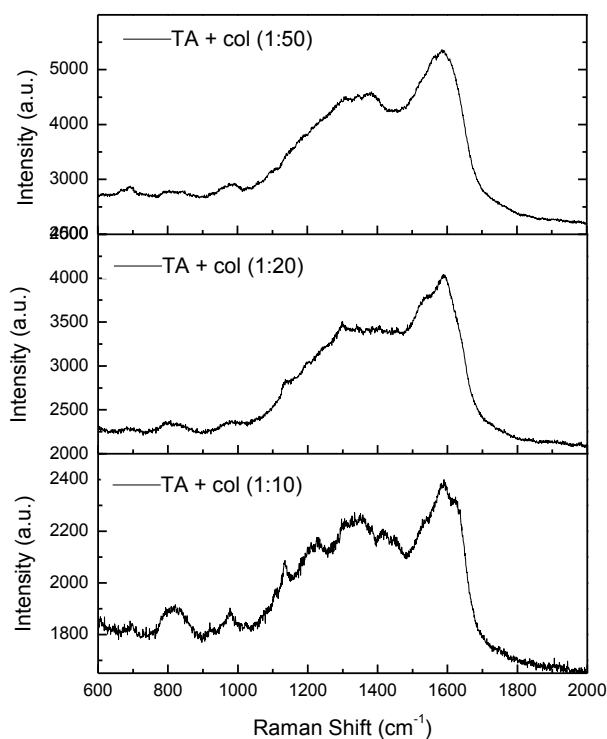


**Figure 7.6:** SERS spectra of TA, where the bacteria and the silver colloids solution mixed with different ratios.

## 7.4 Summary and Conclusions

In this work, silver nanoparticle colloidal suspensions were prepared using two common methods and used to enhance the intensity of Raman signals obtained from bacteria. One  $\mu\text{M}$  rhodamine 6G solution was used to test the stability of the colloids and the efficiency of the enhancement. The results revealed that the colloids were efficient to enhance the intensity of the signal for both R6G and bacteria where the Raman signature of R6G was recovered with a consistent shift, while those for bacteria either disappeared or totally changed. This indicated that the dilution of bacteria in the colloids solution made the detection of bacterial Raman signal very difficult due to the low number of bacteria in the solution. That should be compensated by the great enhancement due to the presence of silver colloids which did not occur in this case. Also it was noticed that the enhancement of SERS varied with the concentration of the colloids.

## CHAPTER 7 REFERENCES

- <sup>1</sup> A. Campion and P. Kambhampati. "Surface-enhanced Raman scattering," *Chemical Society Reviews* **27**:241-250 (1998).
- <sup>2</sup> M. Fleishman, P.J. Hendra, and A.J. McQuillan. "Raman spectra of pyridine adsorbed at a silver electrode," *Chemical Physics Letters* **26**:163-166 (1974).
- <sup>3</sup> D.L. Jeanmaire and R.P. Van Duyne. "Surface Raman Spectroelectrochemistry Part I. Heterocyclic, aromatic, and aliphatic amines adsorbed on the anodized silver electrode," *Journal of Electroanalytical Chemistry* **84**:1-20 (1977).
- <sup>4</sup> R. Aroca, *Surface-enhanced Vibrational Spectroscopy*. UK John Wiley & Sons Ltd (2006).
- <sup>5</sup> M. Moskovits and J.S. Suh. "Surface selection rules for surface-enhanced Raman spectroscopy: calculations and application to the surface-enhanced Raman spectrum of phthalazine on silver," *Journal of Physical Chemistry* **88**:5526-5530 (1984).
- <sup>6</sup> P.C. Lee and D. Meisel. "Adsorption and surface-enhanced Raman of dyes on silver and gold sols," *Journal of Physical chemistry*. **86**:3391-3395 (1982).
- <sup>7</sup> M. Cyrankiewicz, T. Wybranowski, and S. Kruszewski. "Study of SERS efficiency of metallic colloidal systems," *Journal of Physics: Conference Series* **79**:012013 (2007).
- <sup>8</sup> J.A. Creighton, C.G. Blatchford and M.G. Albrecht. "Plasma resonance enhancement of Raman scattering by pyridine adsorbed on silver or gold sol particles of size comparable to the excitation wavelength," *Journal of the Chemical Society: Faraday transactions* **75**:790-798 (1979).

## Chapter8

### Bacterial Characterization Using Electron Microscopy

#### 8.1 Introduction

Electron microscopy is a very well-studied imaging technique that uses a beam of electrons to illuminate a target to create a highly magnified image of the target. This technique can be used for imaging biological samples (including bacteria) but this requires extra procedures to solidify the bacteria target and make it easier to handle.<sup>1,2</sup> Transmission electron microscopy provide a cross sectional image which can be used to detect any difference in the wall thickness of different bacterial samples. On the other hand scanning electron microscopy is used to show the outer surface structure of bacterial cells.

#### 8.2 Transmission Electron Microscopy (TEM)

In this case, the sample will be hit by a high energy electron beam (100-400 keV), the direct beam will go through the sample, while the Bragg reflected beams will be scattered out of the sample. The transmitted electrons will be detected using a fluorescent screen. The electrons will scatter more from the massive regions of the sample and it will appear darker, while the areas with light atoms will allow more transmission of the electrons to come through and it will appear bright. Thus image contrast depends on the atomic composition of the target and this image can be displayed on a monitor using a CDD camera.

TEM was used for imaging the cross section of *M. smegmatis* bacteria to attempt to get a clear image of the cell wall thickness. Many steps were performed to prepare the samples and many steps were required for sectioning the bacteria to get ultrathin slices for TEM imaging. These procedures included chemical fixation and dehydration of the specimens, and then a

polymer resin was used to stabilize them before sectioning them using a microtome. The following is a detailed Protocol for sample preparation.<sup>3</sup>

### **1. Fixation:**

1. Take 50 ml of cells, centrifuge and remove the supernatant.
2. Add Fixative 1 ( 2% paraformaldehyde and 2.5 % glutaraldehyde in 0.2 M Sucrose (pH 7.4)). Pour fixative through the wall of the tube, (do not vortex). After 10 min dissolve the pellet by mixing.
3. Incubate at 4 C overnight.
4. Centrifuge and remove the supernatant.
5. Add 1% solution of OsO<sub>4</sub> in Na-Cacodylate buffer and incubate at 4 C for 2 Hr.
6. Wash with Na-cacodylate 3 times 5 minutes (at this step sample can be stored up to a week at 4 C).

### **2. Dehydration:**

1. 30% Acetone 30 min
2. 50% Acetone 30 min
3. 70% Acetone 30min
4. 95% Acetone 30min
5. 100% Acetone 60 min

### **3. Preparation of resin**

1. Warm the following items to 60°C for not less than 15 min.  
(Epon 812 resin (20 mL), DDSA (9 mL), and MNA (12 mL)). The stock components may be warmed many times over.
2. Pour the required volume of Epon 812 resin into the tube or bottle, add the DDSA and

MNA and pour into the bottle. Mix gently by hand and place on rotator/ mixer for 10 min.

3. Add BDMA or DMP (1.2 mL) and mix as before.

Complete resin can be frozen if necessary.

#### **4. Infiltration:**

1. Mix 50:50 epoxy resin: acetone and bacterial pellet from dehydration step overnight on a rotating mixer.
2. Centrifuge at highest rpm for 15 min and remove the supernatant. (You lose lots of cells at this stage and the supernatant is very sticky).
3. Add fresh epoxy resin for 2–4 h on a rotating mixer with the caps off to allow excess acetone to evaporate.
4. Centrifuge at highest rpm for 15 min remove the supernatant. (You will lose lots of cells at this stage and the supernatant is very sticky).
5. Add fresh epoxy resin for a further 2–4 h on a rotating mixer.

Centrifuge at highest rpm for 15 min remove the supernatant. (You will lose lots of cells at this stage and the supernatant is very sticky).

#### **5. Embedding:**

1. Embed in fresh epoxy resin. (Add DMP or BDMA only at this step)
2. Label BEEM capsule.

Transfer resin in to a beam capsule using a tip or wooden applicator stick and incubate at 60 C for 48 hr.

**6. Sectioning:**

Observe the thick section, and trim EM block further if needed. Then ultrathin sectioning and collection on grids. Sections less than 100 nm thick are good (gold color).

**7. Staining:**

1. Staining grids with uranyl acetate. Uranyl acetate: The uranyl acetate stains must be made fresh before use. Add 0.05 g-0.01 g of uranyl acetate powder to 10 mL distilled water and allow to dissolve. This is a radiochemical and must be handled appropriately
2. On a dental wax sheet place a drop of uranyl acetate stain. Pick up a grid with the section and invert on top of the drop of the stain. Because of surface tension the grid will float on top of the drop.
3. Cover the Petri dish and leave for the 30 min.
4. Pour distilled water in a petri plate. Then pick the grid with a forceps and pass it through distilled water 4-5 times.
5. Carefully dry the edge of grid using a filter paper.
6. Lead stains are very sensitive and will precipitate quickly upon contact with CO<sub>2</sub>. To prevent this from happening either during preparation, storage, or staining. Prepare CO<sub>2</sub> free water: boil double distilled water and store it at once (while still hot) in tightly capped bottles or glass stoppered bottles. When these bottles are opened you should hear a hissing sound, which indicates the bottles were sealed properly. Use this water for preparation of the stain.
7. To prepare lead citrate stain add 0.01g - 0.04g Lead citrate to 10 ml CO<sub>2</sub> free distilled water. Add 0.1 ml 10N NaOH. Cap the bottle and shake well until clear.
8. In a large petri plate keep some NaOH pellet. Place a small petri plate at the centre and

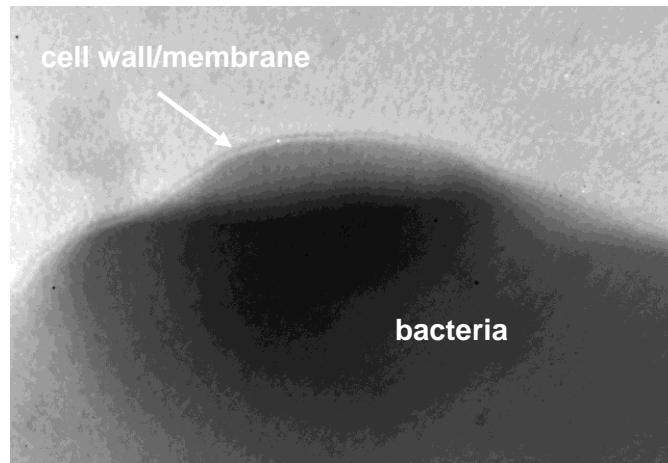


**Figure 8.1:** TEM image of *M. smegmatis*. We are trying to quantify variations in the cell membrane thickness.

pour some lead citrate stain in small petri plate.

9. Using a forcep keep the pre-stained grid inverted on top of the stain. Because of surface tension the grid will float on top.
10. Pour some water on NaOH pellet and cover the lid of he large petri plate.
11. Incubate for 30 min.
12. Wash the grid as in step 4.
13. Air dry the section.

The section is ready to observe under TEM. Figure 8.1 shows a cross sectional image of *M. smegmatis* bacteria.

### 8.3 Scanning Electron Microscopy (SEM)

For SEM imaging, lower energy electrons (1-50 keV) are used to hit the sample and the backscattered electrons are collected. These electrons have a broad energy distribution due to

the energy loss through the collisions with the target atoms. The electrons will scatter more efficiently from heavier atoms and as a result a contrast can be observed from different atoms.

To test if the phosphorylation of Wag31 caused changes in outer cell wall structure, I initiated Scanning Electron Microscopy (SEM) studies of mycobacterial cells containing phosphorylated (Wag31T73E) and non-phosphorylated (Wag31T73A). The sample preparation start with fixation as stated before, then rinsing in distilled water several times to remove buffer. After that the samples were freeze-dried. Finally, the dried cells were covered by an ultra-thin layer of gold to increase conductivity of the specimen so it will emit more secondary electrons and produce a higher contrast image. The results showed a slight difference in the cell surface of these cells as seen in the following figure.

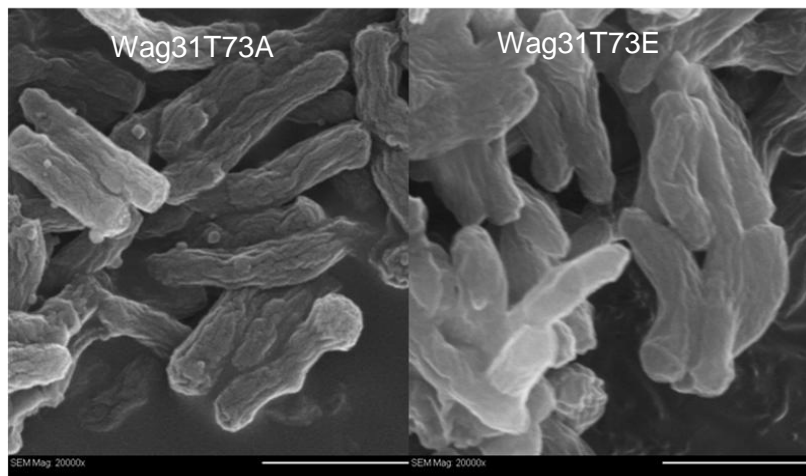


**Figure 8.2:** SEM image of *M. smegmatis* cells containing phosphorylated (Wag31T73E) and non-phosphorylated (Wag31T73A).

## 8.4 Conclusions

SEM and TEM were used to characterize the outer cell surface (SEM) and the inner cross-section (TEM) of bacteria. The preliminary results showed a slight difference between different mutants of *M. smegmatis* bacteria and TEM image showed clearly the cell wall thickness of the cell, these results are promising and open the door for further investigation in order to connect the variations obtained using Raman spectroscopy with a real observed variation using electron microscopy technique.

### CHAPTER 8 REFERENCES

---

<sup>1</sup> E.G. Afrikian, G.St. Julian, and L.A. Bulla, "Scanning electron microscopy of bacterial colonies," *Applied Microbiology* **26**:934–937 (1973).

<sup>2</sup> H.C. Bae, E.H. Costa-Robles, and L.E. Casida, "Microflora of soil as viewed by transmission electron microscopy," *Applied Microbiology* **23**:637-648 (1972).

<sup>3</sup> J. Kuo. *Electron Microscopy Methods and Protocols*, 2nd Edition, Clifton, NJ (2007).

**ABSTRACT****RAMAN SPECTROSCOPY FOR THE MICROBIOLOGICAL  
CHARACTERIZATION AND IDENTIFICATION OF MEDICALLY  
RELEVANT BACTERIA**

by

**KHOZIMA MAHMOUD HAMASHA****August 2011****Advisor:** Dr. Steven J. Rehse**Major:** Physics**Degree:** Doctor of Philosophy

The detection and identification of pathogenic bacteria has become more important than ever due to the increase of potential bioterrorism threats and the high mortality rate of bacterial infections worldwide. Raman spectroscopy has recently gained popularity as an attractive robust approach for the molecular characterization, rapid identification, and accurate classification of a wide range of bacteria.

In this dissertation, Raman spectroscopy utilizing advanced statistical techniques was used to identify and discriminate between different pathogenic and non-pathogenic bacterial strains of *E. coli* and *Staphylococcus aureus* bacterial species by probing the molecular compositions of the cells.

The five-carbon sugar xylitol, which cannot be metabolized by the oral and nasopharyngeal bacteria, had been recognized by clinicians as a preventive agents for dental

caries and many studies have demonstrated that xylitol causes a reduction in otitis media (chronic inner ear infections) and other nasopharyngeal infections. Raman spectroscopy was used to characterize the uptake and metabolic activity of xylitol in pathogenic (*viridans group Streptococcus*) and nonpathogenic (*E. coli*) bacteria by taking their Raman spectra before xylitol exposure and after growing with xylitol and quantifying the significant differences in the molecular vibrational modes due to this exposure. The results of this study showed significant stable spectral changes in the *S. viridians* bacteria induced by xylitol and those changes were not the same as in some *E. coli* strains.

Finally, Raman spectroscopy experiments were conducted to provide important information about the function of a certain protein (*wag 31*) of *Mycobacterium tuberculosis* using a relative non-pathogenic bacterium called *Mycobacterium smegmatis*. Raman spectra of conditional mutants of bacteria expressing three different phosphorylation forms of *wag31* were collected and analyzed. The results show that the phosphorylation of *wag31* causes significant differences in the molecular structure, namely the quantity of amino acids associated with peptidoglycan precursor proteins and lipid II as observed in the Raman spectra of these cells. Raman spectra were also acquired from the isolated cell envelope fraction of the cells expressing different forms of *wag31* and the results showed that a significant number of the molecular vibrational differences observed in the cells were also observed in the cell envelope fraction, indicating that these differences are localized in the cell envelope.

## AUTOBIOGRAPHICAL STATEMENT

### Education

- Wayne State University, Detroit, MI: Doctor of Philosophy (Expected Graduation: August 2011).

Thesis: Raman spectroscopy for the microbiological characterization and identification of medically relevant bacteria

- Wayne State University, Detroit, MI: M.S. Physics (Graduation: December 2010)
- Yarmouk University, Jordan: M.S. Physics (Graduation: June 2001)
- Yarmouk University, Jordan: B.S. Physics (Graduation: June 1998)

### Work Experience

- Graduate Teaching and Research Assistant: Wayne State University, MI, USA, 2006-2011.
- Assistant Lecturer in Physics: Yarmouk University, Jordan, 2003-2006.
- Lecturer in Physics: Yarmouk University/Model School, Jordan, 2001-2003.

### Selected Publications

**1. Khozima Hamasha**, Moodakare Bheema Sahana, Charul Jani, Seeta Nyayapathy, Choong-Min Kang, Steven J. Rehse, “The effect of Wag31 phosphorylation on the cells and the cell fraction of wild-type and conditional mutants of *Mycobacterium smegmatis* studied by visible-wavelength Raman spectroscopy,” *Biochemical and Biophysical Research Communications* **391**: 664-668 (2010).

**2.** Charul Jani, Hyungjin Eoh, Jae Jin Lee, **Khozima Hamasha**, Moodakare Bheema Sahana, Jeong-Sun Han, Seeta Nyayapathy, Jung-Yeon Lee, Joo-Won Suh, Sang Hee Lee, Steve J. Rehse, Dean C Crick, Choong-Min Kang, “Regulation of polar peptidoglycan biosynthesis by Wag31 phosphorylation in *Mycobacteria*” *BMC Microbiology* **10**: 327(2010).

**3.** Sunil Palchaudhuri, Steven J. Rehse, **Khozima Hamasha**, Talha Syed, Eldar Kurtovic, Emir Kurtovic, and James Stenger, “Raman spectroscopy of xylitol uptake and metabolism in Gram-negative and Gram-positive bacteria,” *Applied and Environmental Microbiology* **77**: 131-137 (2011).

**4. Khozima Hamasha**, Qassem Mohaidat, Steven Rehse, and Sunil Palchaudhuri, “Rapid discrimination of four *Escherichia coli* strains using visible-wavelength Raman spectroscopy”, *Journal of Raman Spectroscopy*, in submission (2011).